4-26-2017

Reliability-based Design Optimization with Mixture of Random and Interval Uncertainties

David Yoo
University of Connecticut, david.yoo@uconn.edu

Reliability-based Design Optimization with Mixture of Random and Interval Uncertainties

David Yoo, PhD

University of Connecticut

2017

This study presents novel reliability-based design optimization (RBDO) methods with mixture of random and interval uncertainties. While conventional second-order reliability method (SORM) contains three types of errors, novel SORM proposed in this study avoids the other two types of error by describing the quadratic failure surface with the linear combination of noncentral chi-square variables and using the linear combination of probability of failure estimation. Sensitivity analysis on the developed SORM is then performed for more accurate RBDO. As an alternative to analytic RBDO, sampling-based RBDO is used in case when gradients of performance functions are not available. In this study, interval uncertainty is newly incorporated into existing sampling-based RBDO, since distribution of random uncertainty may not be always identified. Sensitivity-based interval analysis method is developed, which is integrated into optimization framework. It is demonstrated in numerical example that the proposed method efficiently converges to optimum design within a few design cycles. The RBDO approach is further applied to turbomachinery bladed disk, whose dynamic response is very sensitive to presence of uncertainties when interblade coupling is weak. Multi-objective optimization method is developed for optimal piezoelectric circuitry design to simultaneously achieve delocalization of vibration modes and vibration suppression, which is integrated into the host bladed disk structure. Since piezoelectric material cannot withstand the high temperatures, this method is limited to fan blades that is operated at mild temperatures. Alternatively, this study develops the mathematical framework of reliability-oriented optimal design for bladed disk throughout modification of geometry/material properties of blades utilizing intentional mistuning technique, which is applicable to both compressor blades and high pressure turbine blades that are operated at severe temperatures. Both random uncertainty of blades and interval uncertainty of disk connections are

considered. It is demonstrated in case studies that durability and reliability in bladed disk can be achieved using the proposed method.

Reliability-based Design Optimization with Mixture of Random and Interval Uncertainties

David Yoo

B.S., Georgia Institute of Technology, 2008

M.S., Seoul National University, 2012

A Dissertation

Submitted in Partial Fulfillment of the

Requirements for the Degree of

Doctor of Philosophy

at the

University of Connecticut

2017

APPROVAL PAGE

Doctor of Philosophy Dissertation

Reliability-based Design Optimization with Mixture of Random and Interval Uncertainties

Presented by

David Yoo, B.S., M.S.

Major Advisor _____
Dr. Jiong Tang

Associate Advisor _____
Dr. Xu Chen

Associate Advisor _____
Dr. Horea Ilies

Associate Advisor _____
Dr. Ying Li

Associate Advisor _____
Dr. Julian Norato

University of Connecticut
2017

Table of Contents

List of Tables

List of Figures

Chapter 1. Introduction

Most mechanical engineering designs involves a single/multiple times of optimization process in which design objectives such as cost and weight, and other various performances are considered. Design optimization process can be very complex, due to a large number of design variables involved and due to complicated and not explicitly known functional relationships between objective/performances and design variables. In the meantime, practical engineering designs are inevitably subject to uncertainties in geometrical or material properties due to manufacturing tolerance, external loading, and in-service degradation. The responses/performances of mechanical engineering designs such as turbomachinery bladed disk can sometimes be very sensitive to presence of the uncertainties. It is therefore necessary to incorporate stochastic nature of mechanical deigns into their optimization processes to promise product qualities (Haldar and Mahadevan 2000; Tsompanakis *et al*. 2008).

During the past decades, there have been a number of researches that attempt to develop effective optimization methods for mechanical engineering designs in the presence of uncertainties, which is namely reliability-based design optimization (RBDO) (Youn *et al*. 2004; Acar and Solanki 2009; Fang *et al*. 2013). The important step of RBDO is the identification of functional behavior of the main objective and specific performance of interest in terms of design variables, which are namely objective and performance function. In practical engineering design problems, performance functions are often not explicitly known. In such cases, samples are collected throughout numerical simulation such as finite element analysis (FEA) over the domains of design variables, performance functions can be then approximated using various regression techniques such as Gaussian process and Kriging methods. Consequently, failure surface that differentiates failure and non-failure cases, namely failure/constraint surface, can be identified. After determination of distributions of random variables, the main stage of RBDO consists of calculation of probability of failure or reliability of design variables on the performance function, which is namely reliability analysis. In theory, reliability analysis requires complete evaluation of multi-dimensional integral of joint probability

distributions of random design variables over the failure surfaces. Due to the challenges that failure surfaces are often nonlinear and complicated, it is most times not possible to directly evaluate the probability of failure, while retaining both accuracy and efficiency. There have been a number of studies on reliability analysis, which are, in general, categorized into analytic and sampling-based method.

Analytic method is very efficient but less accurate method, which involves approximation of failure surface by Taylor series polynomial. Depending on degree of approximation, first-order and second-order reliability method (FORM and SORM) have been developed. FORM has been widely used due to its convenience and efficiency (Hasofer and Lind 1974). On the other hand, it loses serious amount of accuracy as failure surface becomes more and more nonlinear. SORM has been developed to improve this drawback of FORM. SORM, although it also has the weakness that second-order derivative information is required, significantly improves the accuracy of FORM, when failure surface is nonlinear (Madsen *et al*. 1986). Nevertheless, SORM is still the approximation method that contains three types of errors (Adhikari 2004). The first error comes from the quadratic approximation of failure surface at most probable point (MPP) after the transformation to standard normal space. The second error comes from parabolic approximation of failure surface. The third error comes from calculation of probability of failure. In this research, novel second-order reliability method is proposed to improve accuracy of the conventional SORM (Lee *et al*. 2012; Yoo *et al*. 2014). The proposed SORM entails approximation after the first quadratic approximation that is inherent nature of SORM. This is enabled by further transformation of random design variables into chi-square space where failure surface becomes completely linear function of random variables, which are chi-square variables.

Sampling-based method, although computationally expensive, is very accurate method. There have been studies to develop mathematical formulation of sampling-based RBDO including derivation of sensitivity of reliability with respect to random variables (Lee and Jung 2008; Lee *at el*. 2011). Although reliable optimum design can be effectively obtained based on the derived formulation in the literature, it should be pointed out that these studies are carried out under the assumption that uncertainties are all

random with known distributions. As will be explained in Chapter 4 in more details, generally, there are two types of uncertainties. Aleatory uncertainty is irreducible uncertainty that is inherent variability; on the other hand, epistemic uncertainty is due to the lack of knowledge about a physical system (Hofer *et al*. 2002; Guo and Du 2007). There are three types of epistemic uncertainties which can be listed in the ascending order of uncertainty degree as: random uncertainty, fuzzy uncertainty, and interval uncertainty. Random uncertainty is defined as the uncertainty of which the complete probabilistic distribution is known. Interval uncertainty, on the other hand, is defined as the uncertainty of which only the interval is known while the probabilistic distribution is unknown. In practical engineering design problems, it is often not possible to identify complete distribution of all the uncertainties. Clearly, in reality at least some of the uncertainties are often interval uncertainties.

Therefore, the proposed study develops the sampling-based RBDO in the presence of interval uncertainty (Yoo and Lee 2014). Although not sampling-based, there have been a few previous studies on RBDO with interval uncertainty (Du *et al*. 2005; Mourelatos and Zhou 2005). Most of these studies are carried-out under at least one of these assumptions: (1) bounds of reliability occur at bounds of interval uncertainties, and (2) the bounds of probability of failure always occur at the bounds of performance function. Without making these assumptions, large amount of computations, which is to consider all combinations of interval uncertainties, are required to treat interval uncertainties. When there are a number of interval uncertainties, the calculation becomes virtually impractical without implementation of appropriate algorithm. The proposed study does not make those assumptions. The key idea here is defining behavior of interval uncertainty by Dirac delta function (Browder 1996), similarly to probability density function (PDF) of random variable, sensitivity of reliability with respect to random and interval uncertainties can be thus derived. At the end, sensitivity-based search algorithm can be developed to obtain bounds of reliability.

In this study, RBDO approach is further applied to the turbomachinery bladed disk whose dynamic response is highly sensitive to the presence of uncertainties when the inter-blade coupling is weak. A well-

known problem in bladed disks is that vibration localization could easily occur even with small amount of uncertainty, which is namely mistuning (Yoo *et al*. 2003; Chan and Ewins 2011). When vibration localization occurs, the vibration modes and/or the forced responses under engine-order excitations become drastically different from their counterparts under ideal periodicity (Bladh *et al*. 2002; Castanier and Pierre 2006). That is, the energy is confined to a small number of blades that experience excessive vibration. Some of the previous studies proposed optimization formulations to identify design to minimize the maximum response amplitude amongst the blades (Choi *et al*. 2003; Han *et al*. 2014). While these formulations may certainly benefit the reliability, strictly speaking they cannot yield an optimal design under a pre-specified reliability level. Therefore, one may either reach an overly conservative design that satisfies the reliability requirement but suffers from too much design modification that deteriorates aerodynamic performance, or, reach a design that albeit is optimal under the optimization formulation but still cannot satisfy the reliability requirement. In proposed RBDO formulation, optimal design that satisfies the specific reliability requirement, while minimizing the cost of implementation, can be obtained (Yoo and Tang 2016).

Generally, there are two types of approach to enhance reliability of bladed disks. One type of approach is the technique of namely intentional mistuning (Martel *et al*. 2007; Nikolic *et al*. 2008; Yu *et al*. 2011). In this type of approaches, a pre-specified blade-to-blade design modification is introduced directly into the baseline design, intentionally breaking the ideal periodicity in a deterministic manner. Usually, this intentional mistuning is large enough to overcome the near singularity in the eigensolution sensitivity, but insignificant to cause change in the dynamic characteristics of the bladed disk involved. Several investigations have suggested certain patterns/distributions of intentional mistuning that help reducing the vibration localization. Alternative approach is through integrating passive control devices such as piezoelectric circuitry where piezoelectric transducers are integrated onto individual blades to convert part of the vibration energy into electrical energy (Tang and Wang 1999; Tang and Wang 2003; Yu *et al*. 2006). The converted electrical energy can propagate freely through a well-design circuitry network with strong inter-blade-circuit coupling. Both approaches have their own strengths and weaknesses. The first approach

has drawback that baseline design has to be modified. The second approach has the limitation that some passive control devices cannot sustain high temperature so their applications are limited to cold sections of turbomachinery such as fan blades. Our goal in this research is to use both above mentioned methods to develop new methods to achieve reliability-oriented robust design for bladed disks with random and interval uncertainties.

The paper is organized as follow. Chapter 2 presents the proposed SORM that improves the accuracy of the conventional SORM. Chapter 3 carries out mathematically rigorous sensitivity analysis on the proposed SORM. Chapter 4 introduces the sampling-based design optimization with mixture of random and interval variables. Chapter 5 proposes mathematical framework of reliability-oriented robust design for bladed disks using intentional mistuning. Chapter 6 shows multi-objective optimization of piezoelectric circuitry network for vibration suppression of mistuned bladed disks. Chapter 7 summarizes and concludes this study.

Chapter 2. Novel Second-Order Reliability Method (SORM) Using Non-Central or General Chi-Squared Distributions

2.1 Introduction

The most probable point (MPP)-based method is very popular in the analytical methods and includes first-order reliability method (FORM) (Haldar and Mahadevan 2000; Hasofer and Lind 1974; Tu and Choi 1999; Tu *et al.* 2001), second-order reliability method (SORM) (Breitung 1984; Hohenbichler and Rackwitz 1988; Adhikari 2004; Zhang and Du 2010), and the MPP-based dimension reduction method (DRM) (Rahman and Wei 2006; Lee *et al.* 2008; Xiong *et al.* 2008). The probability density function (PDF) approximation method (Rosenblueth 1975; Du and Huang 2006; Youn *et al.* 2006) is also one of the analytical methods and approximates a PDF of the performance function by assuming a general distribution type for the probability of failure calculation. The simulation or sampling methods such as the Monte Carlo simulation (MCS) (Rubinstein and Kroese 2008), importance sampling method (Denny 2001; Bucklew 2010), and Latin hypercube sampling method (McKay *et al.* 1979; Huntington and Lyrintzis 1998; Helton and Davis 2003; Helton *et al.* 2006; Olsson *et al.* 2003), can be readily used for the probability of failure calculation since these methods do not require any analytical formulation. However, due to extensive computational burden, the simulation or sampling methods need to be combined with surrogate models for the design optimization (Zhao *et al.* 2011; Lee *et al.* 2011; Simpson *et al.* 2001; Queipo *et al.* 2005; Buranathiti *et al.* 2005).

Among these methods, the MPP-based method computes the probability of failure by approximating the performance function $G(\mathbf{X})$ using the first or second-order Taylor series expansion at MPP as in FORM or SORM, respectively, or the summation of univariate functions at MPP as in the MPP-based DRM. The reliability analysis using FORM could be very well erroneous if the performance function is highly nonlinear and/or multi-dimensional (Lee *et al.* 2008). The MPP-based DRM is much more accurate than FORM and users can control its accuracy by changing the number of integration (or quadrature) points (Lee

et al. 2008). However, the computational cost increases rapidly with the number of random variables. SORM is obviously more accurate than FORM since it uses a quadratic function for the reliability calculation approximated at MPP which requires the gradient and Hessian of the performance function at MPP. Once the gradient and Hessian at MPP are available, SORM uses a parabolic approximation of the quadratic function in various ways to calculate the probability of failure of the performance function (Adhikari 2004; Madsen *et al.* 1986). Because of the parabolic approximation, existing SORM methods entail additional errors on top of the quadratic approximation error (Adhikari 2004), which will be explained in detail in Section 2.2.2.

The main objective of the study in this chapter is to propose a novel SORM methodology to compute the probability of failure (or reliability) using non-central or generalized chi-squared distribution. To apply the proposed method, an MPP should be first found after transforming all random variables in the original X-space to the standard normal U-space through Rosenblatt transformation (Rosenblatt 1952). Once a quadratic approximation at MPP in U-space is available, the proposed method does not use further approximation of the quadratic function. Instead, the proposed method converts the quadratic failure function of standard normal variables to the linear combination of non-central chi-square variables using orthogonal transformation. Since every random variable in U-space is the standard normal variable, the probability of failure of a quadratic function in U-space can be obtained using a linear combination of non-central chi-square variables which will be shown in Section 2.3 in detail. The study in this chapter proposes two approaches to compute the probability of failure using the linear combination of non-central chi-square variables: the first approach directly calculates the probability of failure using numerical integration of the joint PDF over the linear failure surface and the second approach uses the cumulative distribution function (CDF) of the linear failure surface for the calculation of the probability of failure. For the first approach, an analytical form of a marginal PDF of a non-central chi-square variable is necessary, which is already available in the literature (Johnson *et al.* 1994; Johnson *et al.* 1994). For the second approach, various representations for CDF of linear combinations of non-central chi-square variables or equivalently

quadratic forms in standard normal vectors have been proposed over the last five decades assuming positive definite quadratic form (Ruben 1962; Siddiqui and Alkarni 2001; Farebrother 1984), approximating the distribution function using numerical methods (Farebrother 1984; Davies 1980; Imhof 1961), using exact series (Harville 1971; Shah 1963; Provost and Rudiuk 1996; Press 1966), or using the upper bound of the distribution function (Siddiqui and Alkarni 2001). In the study in this chapter, exact expression of the distribution functions of linear combinations of non-central chi-square variables which is called a general chi-square distribution (Provost and Rudiuk 1996) will be applied to compute the probability of failure of performance functions after approximating them at MPP in quadratic forms.

2.2 Review of FORM and SORM

2.2.1 First-Order Reliability Method (FORM)

A reliability analysis entails calculation of probability of failure, denoted as P_F, which is defined using a multi-dimensional integral

$$P_F \equiv P[G(\mathbf{X}) > 0] = \int_{G(\mathbf{X})>0} f_{\mathbf{X}}(\mathbf{x}) d\mathbf{x} \tag{2.1}$$

where $P[\bullet]$ is a probability function, $\mathbf{X}=\{X_1, X_2, \cdots, X_N\}^{\mathrm{T}}$ is an N-dimensional random vector where the upper case X_i means that they are random variables and the lower case x_i means that they are the realization of the random variable X_i, $G(\mathbf{X})$ is the performance function such that $G(\mathbf{X}) > 0$ is defined as failure, and $f_{\mathbf{X}}(\mathbf{x})$ is a joint PDF of the random variable $\mathbf{X}$. For the computation of the probability of failure in Equation (2.1), FORM linearizes $G(\mathbf{X})$ at MPP in U-space obtained through Rosenblatt transformation and the linearized function is given by

$$G(\mathbf{X}) = g(\mathbf{U}) \cong g_L(\mathbf{U}) = g(\mathbf{u}^*) + \nabla g^{\mathrm{T}}(\mathbf{U} - \mathbf{u}^*) \tag{2.2}$$

where $\mathbf{u}^*$ is the MPP in U-space which is defined as the point on the limit state function with minimum distance from the origin, and is obtained by solving the following optimization to

$$\begin{aligned} &\text{minimize} \quad \|\mathbf{u}\| \\ &\text{subject to} \quad g(\mathbf{u}) = 0 \end{aligned} \tag{2.3}$$

and ∇g is the gradient vector of the performance function evaluated at the MPP in U-space. Using the definition of the MPP, Equation (2.2) is further simplified as

$$g_L(\mathbf{U}) = \nabla g^{\mathrm{T}}(\mathbf{U} - \mathbf{u}^*) \tag{2.4}$$

since $g(\mathbf{u}^*) = 0$. The reliability index, denoted as β, is then defined as the distance from the origin to $\mathbf{u}^*$ and is given by (Hasofer and Lind 1974)

$$\beta = \|\mathbf{u}^*\| = \left(\mathbf{u}^{*\mathrm{T}}\mathbf{u}^*\right)^{1/2} \tag{2.5}$$

Using the linearized performance function and the reliability index β, FORM approximates the probability of failure in Equation (2.1) as

$$P_F^{\mathrm{FORM}} \cong \Phi(-\beta) \tag{2.6}$$

where $\Phi(\bullet)$ is the standard normal CDF.

2.2.2 Second-Order Reliability Method (SORM)

In SORM, the true limit state function is approximated by its second-order Taylor series expansion at the MPP which is given as

$$\begin{aligned} G(\mathbf{X}) = g(\mathbf{U}) \cong g_Q(\mathbf{U}) &= \nabla g^{\mathrm{T}}(\mathbf{U} - \mathbf{u}^*) + \frac{1}{2}(\mathbf{U} - \mathbf{u}^*)^{\mathrm{T}}\mathbf{H}(\mathbf{U} - \mathbf{u}^*) \\ &= \left(-\nabla g^{\mathrm{T}}\mathbf{u}^* + \frac{1}{2}\mathbf{u}^{*\mathrm{T}}\mathbf{H}\mathbf{u}^*\right) - \left(-\nabla g^{\mathrm{T}} + \mathbf{u}^{*\mathrm{T}}\mathbf{H}\right)\mathbf{U} + \frac{1}{2}\mathbf{U}^{\mathrm{T}}\mathbf{H}\mathbf{U} \end{aligned} \tag{2.7}$$

using the gradient vector and the Hessian matrix (H) evaluated at the MPP. Using the failure definition $G(\mathbf{X}) > 0$, the MPP in U-space is also written as

$$\mathbf{u}^* = \beta\frac{\nabla g}{\|\nabla g\|} = \beta\boldsymbol{\alpha} \tag{2.8}$$

where $\boldsymbol{\alpha}$ is the normalized gradient vector at the MPP. Dividing Equation (2.7) by $\|\nabla g\|$ and using Equation (2.8) yields

$$\frac{g_Q(\mathbf{U})}{\|\nabla g\|}=\left(-\beta+\frac{\beta^2}{2}\boldsymbol{\alpha}^{\mathrm{T}}\frac{\mathbf{H}}{\|\nabla g\|}\boldsymbol{\alpha}\right)-\left(-\boldsymbol{\alpha}^{\mathrm{T}}+\beta\boldsymbol{\alpha}^{\mathrm{T}}\frac{\mathbf{H}}{\|\nabla g\|}\right)\mathbf{U}+\frac{1}{2}\mathbf{U}^{\mathrm{T}}\frac{\mathbf{H}}{\|\nabla g\|}\mathbf{U} \tag{2.9}$$

2.2.2.1 Parabolic Approximation of Quadratic Function

The standard normal U-space can be further transformed to the rotated standard normal V-space for parabolic approximation of the quadratic function in Equation (2.9) using the orthogonal transformation $\mathbf{u}=\mathbf{R}\mathbf{v}$ where $\mathbf{R}$ is an $N\times N$ orthonormal rotation matrix whose N^{th} column is $\boldsymbol{\alpha}$ and can be obtained using the Gram-Schmidt orthogonalization (Adhikari 2004; Rahman and Wei 2006; Lee *et al.* 2008). Thus, the $N\times N$ matrix can be rewritten as $\mathbf{R}=[\mathbf{R}_1|\boldsymbol{\alpha}]$ where $N\times(N\text{-}1)$ matrix $\mathbf{R}_1$ satisfies $\boldsymbol{\alpha}^{\mathrm{T}}\mathbf{R}_1=\mathbf{0}$. After the transformation, the MPP in V-space can be expressed as $\mathbf{v}^*=\{0,\cdots,0,\beta\}^{\mathrm{T}}$. Then, using the orthogonal transformation, Equation (2.9) can be rewritten as

$$\frac{\tilde{g}_Q(\mathbf{V})}{\|\nabla g\|}=\left(-\beta+\frac{\beta^2}{2}\boldsymbol{\alpha}^{\mathrm{T}}\frac{\mathbf{H}}{\|\nabla g\|}\boldsymbol{\alpha}\right)-\left(-V_N+\beta\boldsymbol{\alpha}^{\mathrm{T}}\frac{\mathbf{H}}{\|\nabla g\|}\mathbf{R}\mathbf{V}\right)+\frac{1}{2}\mathbf{V}^{\mathrm{T}}\mathbf{R}^{\mathrm{T}}\frac{\mathbf{H}}{\|\nabla g\|}\mathbf{R}\mathbf{V} \tag{2.10}$$

where $\mathbf{V}=\{V_1,V_2,\cdots,V_N\}^{\mathrm{T}}$. To further simplify Equation (2.10), an $N\times N$ matrix $\mathbf{A}$ is partitioned as

$$\mathbf{A}=\frac{\mathbf{R}^{\mathrm{T}}\mathbf{H}\mathbf{R}}{2\|\nabla g\|}=\begin{bmatrix}\tilde{\mathbf{A}} & \mathbf{A}_{1N}\\ \mathbf{A}_{N1} & A_{NN}\end{bmatrix} \tag{2.11}$$

where $\tilde{\mathbf{A}}$ is an $(N-1)\times(N-1)$ matrix and then using symmetry of $\mathbf{A}$ Equation (2.10) becomes

$$\frac{\tilde{g}_Q(\mathbf{V})}{\|\nabla g\|}=V_N-\beta+\tilde{\mathbf{V}}^{\mathrm{T}}\tilde{\mathbf{A}}\tilde{\mathbf{V}}+\frac{\beta^2}{2}\boldsymbol{\alpha}^{\mathrm{T}}\frac{\mathbf{H}}{\|\nabla g\|}\boldsymbol{\alpha}-\beta\boldsymbol{\alpha}^{\mathrm{T}}\frac{\mathbf{H}}{\|\nabla g\|}\mathbf{R}\mathbf{V}+2V_N\mathbf{A}_{N1}\tilde{\mathbf{V}}+A_{NN}V_N^2 \tag{2.12}$$

where $\tilde{\mathbf{V}}=\{V_1,V_2,\cdots,V_{N-1}\}^{\mathrm{T}}$. Using a parabolic approximation, Madsen *et al.* (1986) further simplified Equation (2.12) to

$$\frac{\tilde{g}_Q(\mathbf{V})}{\|\nabla g\|}\cong V_N-\beta+\tilde{\mathbf{V}}^{\mathrm{T}}\tilde{\mathbf{A}}\tilde{\mathbf{V}} \tag{2.13}$$

by keeping only second-order terms in $\tilde{\mathbf{V}}$ and neglecting any cross terms between $\tilde{\mathbf{V}}$ and V_N. The signs in Equation (2.13) are different from the references (Adhikari 2004; Rahman and Wei 2006; Madsen

et al. 1986) because the failure definition ($G(\mathbf{X}) > 0$) used in this paper is the opposite of one used in the references.

2.2.2.2 Probability of Failure Calculation Using SORM

Using the approximated parabolic surface in Equation (2.13) and the definition of the probability of failure in Equation (2.1), the probability of failure by SORM is given by

$$P_F^{\text{SORM}} \cong P\left[\frac{\tilde{g}_Q(\mathbf{V})}{\|\nabla g\|} > 0\right] \cong P[V_N > \beta - \tilde{\mathbf{V}}^{\mathrm{T}}\tilde{\mathbf{A}}\tilde{\mathbf{V}}] \tag{2.14}$$

Since $V_N \sim N(0,1)$, Equation (2.14) can be rewritten as

$$P_F^{\text{SORM}} \cong P[V_N > \beta - \tilde{\mathbf{V}}^{\mathrm{T}}\tilde{\mathbf{A}}\tilde{\mathbf{V}}] = E\left[\Phi\left(-\beta + \tilde{\mathbf{V}}^{\mathrm{T}}\tilde{\mathbf{A}}\tilde{\mathbf{V}}\right)\right] = E\left[\Phi\left(-\beta + w\right)\right] \tag{2.15}$$

where $E[\bullet]$ is an expectation operator.

Expanding $\ln\left[\Phi\left(-\beta + w\right)\right]$ in a first-order Taylor series about $w = 0$ and keeping up to linear term, we obtain (Adhikari 2004)

$$\Phi(-\beta - w) \cong \exp\left[\ln\{\Phi(-\beta)\} - \frac{\phi(\beta)}{\Phi(-\beta)}w\right] = \Phi(-\beta)\exp\left[-\frac{\phi(\beta)}{\Phi(-\beta)}w\right] \tag{2.16}$$

and Hohenbichler and Rackwitz (1988) showed a non-asymptotic expression of Equation (2.15) using Equation (2.16) as

$$P_F^{\text{SORM}} \cong \Phi(-\beta)\left|\mathbf{I}_{N-1} - 2\frac{\phi(\beta)}{\Phi(-\beta)}\tilde{\mathbf{A}}\right|^{-\frac{1}{2}} \tag{2.17}$$

where $\mathbf{I}_{N-1}$ is an $(N-1) \times (N-1)$ identity matrix and $\phi(\bullet)$ is the standard normal PDF.

Using an asymptotic expression of $\phi(\beta) / \Phi(-\beta)$ in Equation (2.17), which is given as

$$\frac{\phi(\beta)}{\Phi(-\beta)} \cong \beta + \beta^{-1} - 2\beta^{-3} + 10\beta^{-5} - 74\beta^{-7} + \cdots \tag{2.18}$$

and keeping only the first term in Equation (2.18), Breitung (1984) further simplified the probability of failure calculation in Equation (2.17) to

$$P_F^{\text{SORM}} \cong \Phi(-\beta)\left|\mathbf{I}_{N-1} - 2\beta\tilde{\mathbf{A}}\right|^{-\frac{1}{2}} \tag{2.19}$$

which is asymptotically correct when $\beta \to \infty$ (Adhikari 2004).

2.2.2.3 Errors of Conventional SORM

As discussed in Sections 2.2.2.1 & 2.2.2.2, conventional SORM uses a few approximations which result in errors. These approximations and errors can be categorized as (Adhikari 2004):

1. **Type 1**: error due to approximating a general nonlinear limit state function by a quadratic function at MPP in U-space as shown in Equation (2.7).
2. **Type 2**: error due to approximating the quadratic function in U-space by a hyperbolic surface as shown in Equation (2.13)
3. **Type 3**: error due to calculation of the probability of failure after making the previous two approximations as explained in Section 2.2.2.2

Type 1 error is essential to SORM and cannot be improved. Type 2 and 3 errors are introduced in addition to Type 1 error for the calculation of the probability of failure. Besides the three types of errors explained above, there will be error due to the existence of multiple MPPs. However, since cases with multiple MPPs are out of the scope of the paper, this paper will focus only on performance functions with single MPP. Extensive work (Hohenbichler and Rackwitz 1988; Adhikari 2004; Zhang and Du 2010; Hong 1999; Polidori *et al.* 1999) has been performed to improve the accuracy of the reliability analysis by reducing Type 3 error with Type 1 and 2 errors given. In this paper, a novel SORM using non-central or general chi-squared distribution for the reliability analysis is proposed and will be explained in detail in Section 3. *The proposed SORM contains Type 1 error only and thus is always more accurate than existing SORM which contains all three types of errors.* The accuracy of the proposed SORM will be compared with the accuracy of existing SORM in Section 2.4 using numerical examples.

2.3 Non-Central and Generalized Chi-Squared Distributions for SORM

2.3.1 Orthogonal Transformation of Quadratic Function

To propose a new SORM which contains Type 1 error only as explained in Section 2.2.2.3, consider the orthogonal transformation $\mathbf{u} = \mathbf{T}\mathbf{y}$ where $\mathbf{T}$ is the N×N matrix of the eigenvectors of $\mathbf{H}$ and $\mathbf{y} \in \mathbb{R}^N$ is an N-dimensional vector of standard normal random variables, y_i, which are statistically independent to each other since $\mathbf{u}$ is statistically independent. Using the orthogonal transformation, Equation (2.9) can be transformed to (Adhikari 2004)

$$\frac{\hat{g}_Q(\mathbf{Y})}{\|\nabla g\|} = a_0 - \mathbf{a}_1^{\mathrm{T}}\mathbf{Y} + \mathbf{Y}^{\mathrm{T}}\hat{\mathbf{A}}\mathbf{Y} \tag{2.20}$$

where three quantities a_0, $\mathbf{a}_1^{\mathrm{T}}$, and $\hat{\mathbf{A}}$ are given by

$$a_0 = -\beta + \frac{\beta^2}{2}\boldsymbol{\alpha}^{\mathrm{T}}\frac{\mathbf{H}}{\|\nabla g\|}\boldsymbol{\alpha} \in \mathbb{R} \tag{2.21}$$

$$\mathbf{a}_1^{\mathrm{T}} = \left(-\boldsymbol{\alpha}^{\mathrm{T}} + \beta\boldsymbol{\alpha}^{\mathrm{T}}\frac{\mathbf{H}}{\|\nabla g\|}\right)\mathbf{T} \in \mathbb{R}^{1\times N} \tag{2.22}$$

and

$$\hat{\mathbf{A}} = \frac{1}{2\|\nabla g\|}\mathrm{diag}\left[\lambda_1, \lambda_2, \cdots, \lambda_N\right] \in \mathbb{R}^{N\times N} \tag{2.23}$$

where λ_i is the i^{th} eigenvalue of the Hessian matrix $\mathbf{H}$. *Since* $\boldsymbol{u}$ *and* $\boldsymbol{y}$ *are the independent standard normal variables, any orthogonal transformation does not change the probability of failure* (Adhikari 2004). Therefore, the probability of failure in Equation (2.1) can be approximated as

$$P_F \cong P\left[\frac{\hat{g}_Q(\mathbf{Y})}{\|\nabla g\|} > 0\right] = P\left[2\hat{g}_Q(\mathbf{Y}) > 0\right] = P\left[2\|\nabla g\|a_0 + \sum_{k=1}^{N}\left(-2\|\nabla g\|a_{1_k}Y_k + \lambda_k Y_k^2\right) > 0\right] \tag{2.24}$$

and Equation (2.24) can be rewritten as

$$P_F \cong P\left[\sum_{k=1}^{N}\lambda_k\left(Y_k + \delta_k\right)^2 > \sum_{k=1}^{N}\lambda_k\delta_k^2 - 2\|\nabla g\|a_0\right] \tag{2.25}$$

where

$$\delta_k = -\frac{\|\nabla g\| a_{1_k}}{\lambda_k}. \tag{2.26}$$

Since Y_k in Equation (2.25) are standard normal variables, $Z_k = \left(Y_k + \delta_k\right)^2$ are non-central chi-square variables with one degree of freedom and non-centrality parameter δ_k^2 which is denoted as $\chi_1^2(\delta_k^2)$. Then, the probability of failure in Equation (2.25) can be obtained through either numerical integration of PDFs of non-central chi-square variables over the linear failure domain which will be explained in Section 2.3.2 or CDF of a general chi-square variable which will be explained in detail in Section 2.3.3. Compared with the computational cost for the MPP search which requires performance function values and sensitivities obtained from computer simulation, additional computational cost for the proposed probability of failure calculation methods after finding MPP is negligible since they don't require any function evaluations and instead use PDF or CDF of non-central or general chi-square variables which are analytically available.

2.3.2 Non-Central Chi-Squared Distribution

A general non-central chi-square variable with *v* degree of freedom is expressed as

$$\sum_{k=1}^{v}\left(Y_k + \delta_k\right)^2 \tag{2.27}$$

and its CDF is given by (Johnson *et al.* 1994)

$$F\left(x \mid v, \delta\right) = \sum_{j=0}^{\infty}\left(\frac{\left(\frac{1}{2}\delta\right)^j}{j!}e^{-\frac{\delta}{2}}\right)\Pr\left[\chi_{v+2j}^2 \le x\right] = \sum_{j=0}^{\infty}\left(\frac{\left(\frac{1}{2}\delta\right)^j}{j!}e^{-\frac{\delta}{2}}\right)F\left(x \mid v+2j, 0\right) \tag{2.28}$$

where $\delta = \sum_{k=1}^{v}\delta_k^2$ is the non-centrality parameter and $F\left(x \mid v+2j, 0\right)$ is the CDF of a central chi-square variable with *v*+2*j* degree of freedom given by (Johnson *et al.* 1994)

$$F\left(x\,|\,\nu+2j,0\right)=\frac{\Gamma_{x/2}\left(\dfrac{\nu+2j}{2}\right)}{\Gamma\left(\dfrac{\nu+2j}{2}\right)} \tag{2.29}$$

where $\Gamma_x(\alpha)$ denotes the incomplete gamma function defined by

$$\Gamma_x(\alpha)=\int_0^x e^{-t}t^{\alpha-1}dt,\ x>0 \tag{2.30}$$

The PDF of a non-central chi-square variable with *v* degree of freedom is

$$f\left(x\,|\,\nu,\delta\right)=\frac{1}{2}e^{-(x+\delta)/2}\left(\frac{x}{\delta}\right)^{\nu/4-1/2}I_{\nu/2-1}(\sqrt{\delta x}) \tag{2.31}$$

where $I_a(y)$ is a modified Bessel function of the first kind given by

$$I_a(y)=(y/2)^a\sum_{j=0}^{\infty}\frac{(y^2/4)^j}{j!\Gamma(a+j+1)} \tag{2.32}$$

The probability of failure in Equation (2.25) can be further simplified as

$$P_F\cong P\left[Q>a\right]=1-P\left[Q\le a\right] \tag{2.33}$$

where *Q* is a linear combination of non-central chi-square variables Z_k given by

$$Q=\sum_{k=1}^{N}\lambda_k\left(Y_k+\delta_k\right)^2=\sum_{k=1}^{N}\lambda_k Z_k \tag{2.34}$$

and $a=\sum_{k=1}^{N}\lambda_k\delta_k^2-2\|\nabla g\|a_0$ is a constant. The probability of failure in Equation (2.33) can be rewritten as

$$P_F\cong P\left[Q(\mathbf{Z})>a\right]=\int_{Q(\mathbf{Z})>a}f_{\mathbf{Z}}(\mathbf{z})d\mathbf{z} \tag{2.35}$$

where $f_{\mathbf{Z}}(\mathbf{z})$ is the joint PDF of non-central chi-square variables $\mathbf{Z}=\left\{Z_1,Z_2\cdots,Z_N\right\}^{\mathrm{T}}$. Since Y_k are independent, Z_k are independent as well. Thus, the joint PDF of **Z** is the multiplication of its marginal PDFs which are shown in Equation (2.31). Since *Q* is a linear function of Z_k which are non-central chi-

square variables with one degree of freedom and non-centrality parameter δ_k^2, the probability of failure in Equation (2.35) can be evaluated as

$$P_F \cong \int_{Q(\mathbf{Z})>a} f_{\mathbf{Z}}(\mathbf{z})d\mathbf{z} = \int_0^\infty \left(\int_{h(z_1)}^\infty \left(\cdots \int_{h(z_1,\cdots,z_{N-1})}^\infty f_{Z_N}(z_N)dz_N \cdots \right) f_{Z_2}(z_2)dz_2 \right) f_{Z_1}(z_1)dz_1 \tag{2.36}$$

where $h(z_1,\cdots,z_{N-1}) = z_N = \frac{1}{\lambda_N}\left(a - \sum_{k=1}^{N-1} \lambda_k z_k \right)$ and $h(z_1) = \frac{a - \lambda_1 z_1}{\lambda_2}$ are obtained from $Q(\mathbf{Z}) = a$. The multidimensional integral in Equation (2.36) can be numerically calculated using computer software such as MATLAB since $Q(\mathbf{Z})$ is a linear function and thus there is no error in calculation of the probability of failure using Equation (2.36). The integration in Equation (2.36) starts from zero or positive numbers since Z_k are always positive.

If some of the eigenvalues λ_k in Equation (2.34) are not distinct, that is, some of the λ_k's are equal, then some of the non-central chi-square variables will have more than one degree of freedom (Provost and Rudiuk 1996). The non-central chi-square variable with a duplicated eigenvalue can be rewritten as

$$T_j = \sum_{i=1}^{\nu_j} \left(Y_{j_i} + \delta_{j_i} \right)^2 \tag{2.37}$$

where ν_j denotes the multiplicity of eigenvalue λ_j. Thus, T_j in Equation (2.37) is a non-central chi-square variable with ν_j degrees of freedom and non-centrality parameter $\delta_j^2 = \sum_{i=1}^{\nu_j} \delta_{j_i}^2$ and denoted as $\chi_{\nu_j}^2(\delta_j^2)$. Accordingly, without loss of generality, eigenvalues in the linear combination in Equation (2.34) are distinct and Z_k are non-central chi-square variables with ν_k degrees of freedom and non-centrality parameter δ_k^2 in this paper since it does not change the probability of failure calculation in Equation (2.36).

To see how the probability of failure in Equation (2.36) works, let's use a 2-D quadratic example given by

$$G(\mathbf{X}) = X_1^2 - 6X_1 + X_2^2 - 8X_2 + 10 \tag{2.38}$$

where $X_1 \sim N(5,1)$ and $X_2 \sim N(5,1)$, and they are statistically independent. For the probability of failure calculation, Equation (2.38) is transformed to the standard normal U-space which is expressed as

$$g(\mathbf{U}) = U_1^2 + 4U_1 + U_2^2 + 2U_2 - 10 = (U_1 + 2)^2 + (U_2 + 1)^2 - 15 \tag{2.39}$$

Equation (2.39) needs to be transformed to Y-space through $\mathbf{u} = \mathbf{T}\mathbf{y}$. However, since **T**, which is the matrix of the eigenvectors of the Hessian **H**, is the identity matrix in this example, Y-space and U-space are identical. Hence, Equation (2.39) is directly transformed from U-space to χ^2-space where all random variables have chi-squared distribution as

$$\hat{g}_L(\mathbf{Z}) = Z_1 + Z_2 - 15 \tag{2.40}$$

where $Z_1 \sim \chi_1^2(4)$ and $Z_2 \sim \chi_1^2(1)$. Figure 2.1 shows the performance function given in Equation (2.38)~(2.40) in each space. As shown in the figure, the mean value point in X-space, which is (5,5) because $X_1 \sim N(5,1)$ and $X_2 \sim N(5,1)$, becomes (0,0) in U-space since $U_1 \sim N(0,1)$ and $U_2 \sim N(0,1)$ and (5,2) in χ^2-space because a mean value of a non-central chi-square variable is $\nu + \delta$, and $\nu_1 + \delta_1 = 1 + 4 = 5$ since $Z_1 \sim \chi_1^2(4)$ and $\nu_2 + \delta_2 = 1 + 1 = 2$ since $Z_2 \sim \chi_1^2(1)$.

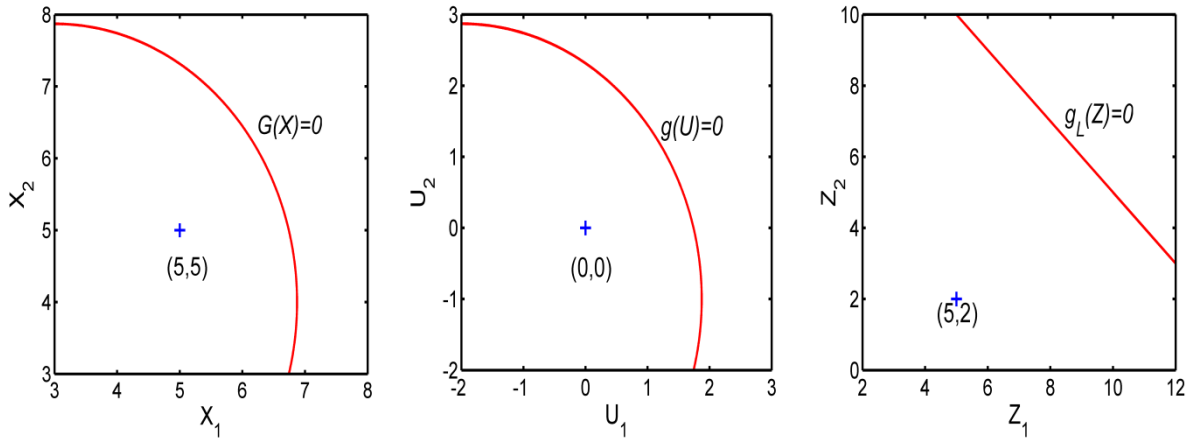

(a) X-space (b) U-space (c) χ^2-space

Figure 2.1 Performance Function in Original and Transformed Space

The probability of failure of the performance function in χ^2-space given in Equation (2.40) can be evaluated using Equation (2.36) as

$$\begin{aligned} P_F &= \int_{\hat{g}_L(\mathbf{Z})>0} f_{\mathbf{Z}}(\mathbf{z})d\mathbf{z} = \int_0^\infty \left(\int_{15-z_1}^\infty f_{Z_2}(z_2)dz_2 \right) f_{Z_1}(z_1)dz_1 \\ &= \int_0^\infty \left(1 - F_{Z_2}(15-z_1)\right) f_{Z_1}(z_1)dz_1 = 1 - \int_0^\infty F_{Z_2}(15-z_1) f_{Z_1}(z_1)dz_1 = 0.0713 \end{aligned} \tag{2.41}$$

Since two eigenvalues of the Hessian **H** of Equation (2.39) are identical to 1, Equation (2.40) can be changed using Equation (2.37) to $\hat{g}_L(\mathbf{Z}) = Z_1 + Z_2 - 15 = Z_3 - 15$ where $Z_3 \sim \chi_2^2(5)$ as explained below Equation (2.37). Hence, the probability of failure can be obtained as $P_F = \int_{15}^\infty f_{Z_3}(z_3)dz_3 = 1 - F_{Z_3}(15) = 0.0713$, which is identical with the result in Equation (2.41). In conclusion, non-central chi-square variables with a duplicated eigenvalue do not change the probability of failure which is theoretically correct.

Since the PDF and CDF of non-central chi-square variables are analytically given as in Equations (2.28) and (2.31), respectively, computational cost for the numerical integration in Equation (2.41) is negligible compared to the MPP search which requires computer simulations. In this example, since a quadratic performance function is used and random variables are normally distributed, there is no approximation used in calculation of the probability of failure and thus there is no error in using the proposed approach.

2.3.3 General Chi-Squared Distribution

As explained in the previous section, the probability of failure in Equation (2.1) can be obtained using a quadratic approximation and non-central chi-square variables. This section will explain that not only the probability of failure but the distribution of *Q* in Equation (2.34) can be obtained using a general chi-squared distribution. Let $\lambda_k > 0$ for $k = 1, \cdots, \rho$, $\lambda_k < 0$ for $k = \rho + 1, \cdots, \rho + \xi$, and $\lambda_k = 0$ for $k = \rho + \xi + 1, \cdots, N$. Then, the linear combination *Q* can be expressed as

$$Q = \sum_{k=1}^{N} \lambda_k Z_k = U - V \tag{2.42}$$

where λ_k are distinct eigenvalues, $Z_k \sim \chi^2_{\nu_k}(\delta_k^2)$, and

$$U = \sum_{k=1}^{\rho} \lambda_k Z_k, \; V = \sum_{k=1+\rho}^{\rho+\xi} \left(-\lambda_k\right) Z_k \tag{2.43}$$

Ruben (1962) obtained the PDF of *U* as (Provost and Rudiuk 1996)

$$f_U(u) = \sum_{i=0}^{\infty} \frac{a_i u^{\alpha+i-1} e^{-u/2\zeta}}{\Gamma(\alpha+i)(2\zeta)^{\alpha+i}}, \; u > 0 \tag{2.44}$$

where

$$\begin{aligned} a_0 &= e^{-\delta/2} \prod_{j=1}^{\rho} \left(\frac{\zeta}{\lambda_j} \right)^{1/2} \\ a_i &= (2i)^{-1} \sum_{r=0}^{i-1} b_{i-r} a_r, \; i \geq 1, \\ b_i &= i\zeta \sum_{j=1}^{\rho} \left(\delta_j^2 / \lambda_j \right) c_j^{i-1} + \sum_{j=1}^{\rho} c_j^i, \; i \geq 1, \end{aligned} \tag{2.45}$$

where $\delta = \sum_{k=1}^{\rho} \delta_k^2$, $\alpha = \rho / 2$, $c_j = 1 - \zeta / \lambda_j$ and ζ is such that

$$\left| c_j \right| = \left| 1 - \zeta / \lambda_j \right| < 1, \quad j = 1, \cdots, \rho \tag{2.46}$$

The parameter ζ is chosen so as to accelerate the convergence of the series in Equation (2.44).

The linear combination *Q* in Equation (2.42) is distributed as the difference of two linear combinations of independent chi-square variables whose PDFs are obtained using Equation (2.44) and is called a general chi-square variable. Since it is not a non-central chi-square variable any more, *Q* does not have a general non-centrality parameter in terms of δ_k^2. Provost and Rudiuk (1996) obtained the exact PDF and CDF of the general chi-square variable using Whittaker's function (Whittaker 1904), which is available in MATLAB or Mathematica. Since they are very complicated, the PDF and CDF of *Q* are not shown in this paper. Once the CDF of *Q* denoted as $F_Q(q)$ is available, the probability of failure in Equation (2.33) can be easily obtained as

$$P_F \cong P\left[Q > a\right] = 1 - P\left[Q \le a\right] = 1 - F_Q(a) \tag{2.47}$$

Let's consider the 2-D example again which is used in Section 2.3.2 to see how this approach is used for the probability of failure calculation. From Equation (2.40), $Q(\mathbf{Z}) = Z_1 + Z_2$ and $Q \sim \chi_2^2(5)$ since $Z_1 \sim \chi_1^2(4)$ and $Z_2 \sim \chi_1^2(1)$ and coefficients of two non-central chi-square variables are identical. Thus, the CDF of *Q* is expressed as $F\left(x \mid 2,5\right)$ using Equation (2.28) and the probability of failure of the performance function in Equation (2.40) is obtained as

$$P_F = P\left[Q > 15\right] = 1 - P\left[Q \le 15\right] = 1 - F(15 \mid 2,5) = 0.0713 \tag{2.48}$$

which is exactly the same as the probability of failure obtained in Equation (2.40). The PDF and CDF of the linear combination *Q* are shown in Figure 2.2.

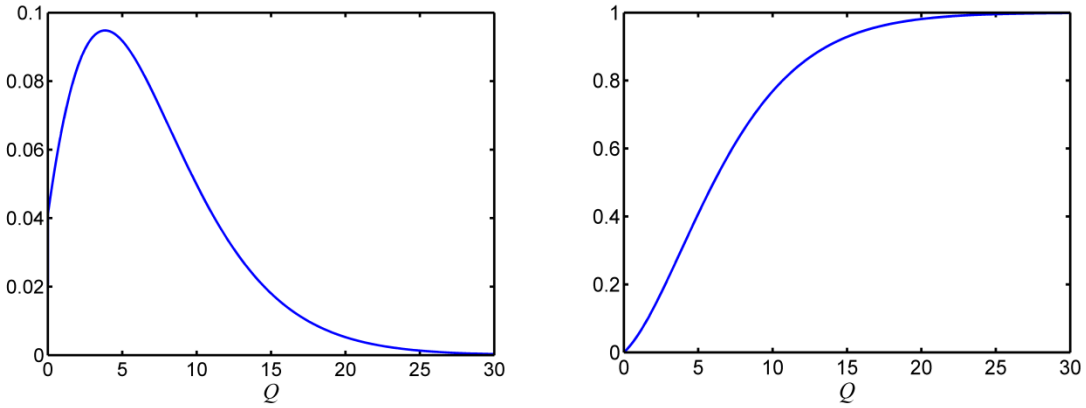

(a) PDF (b) CDF

Figure 2.2 PDF and CDF of Linear Combination *Q* for Equation (2.40)

Figure 2.3 compares conventional and proposed SORM using a flowchart. As shown in the figure,

Figure 3 compares conventional and proposed SORM using a flowchart. As shown in the figure, conventional SORM contains three types of error marked as grey boxes, whereas the proposed SORM contains Type 1 error only. Consequently, *the proposed SORM is always more accurate than existing SORM.*

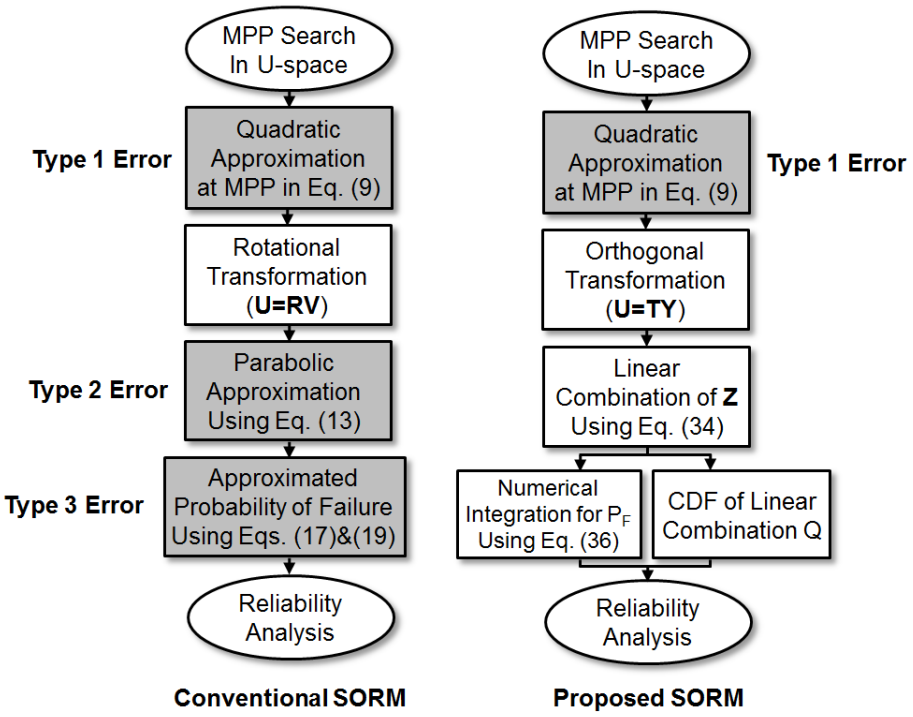

Figure 2.3 Comparison of Conventional and Proposed SORM

2.4 Numerical Examples

This section compares conventional with proposed SORM using numerical examples in terms of accuracy. For the comparison test, two mathematical examples including two dimensional and four-dimensional performance functions and one high dimensional engineering example are used. Since both the conventional and proposed SORM methods contain the same Type 1 error, two mathematical examples in this section do not focus on this error type. This is the reason that two mathematical examples use all quadratic performance functions for the test to focus on how Type 2 and Type 3 error affect the accuracy of reliability analysis. One high dimensional engineering example is used to demonstrate the applicability of the proposed method to real engineering disciplines. Reliability analysis results using conventional and proposed SORM are compared with ones obtained from MCS and FORM in terms of accuracy.

2.4.1 Two-Dimensional Example

To compare the proposed SORM with conventional SORM, consider a 2-D quadratic performance function given by

$$G(\mathbf{X}) = X_1^2 + 2X_1 + X_2^2 + 2X_2 - 0.5X_1X_2 - 13 \tag{2.49}$$

where $X_1 \sim N(0,1)$ and $X_2 \sim N(0,1)$, and they are statistically independent. Since X_1 and X_2 are independent standard normal random variables, X-space and U-space are identical. Thus, Equation (2.49) can be rewritten as

$$g(\mathbf{U}) = U_1^2 + 2U_1 + U_2^2 + 2U_2 - 0.5U_1U_2 - 13 = \frac{1}{2}\mathbf{U}^{\mathrm{T}}\mathbf{H}\mathbf{U} + 2\begin{bmatrix}1 & 1\end{bmatrix}\mathbf{U} - 13 \tag{2.50}$$

To use FORM and SORM for reliability analysis of Equation (2.50), MPP search is first carried out. The search shows that the MPP is (1.8985, 1.8985) and the reliability index is 2.6849. Thus, the reliability analysis using FORM shows that the probability of failure is $\Phi(-2.6849) = 0.3628\%$ as shown in Table 2.1. To apply conventional SORM to the reliability analysis of Equation (2.50), the performance function

in U-space in Equation (2.50) should be transformed to the rotated standard normal V-space using a rotational transformation $\mathbf{u} = \mathbf{R}\mathbf{v}$ where the rotational matrix $\mathbf{R}$ is obtained as

$$\mathbf{R} = \frac{1}{\sqrt{2}}\begin{bmatrix} 1 & 1 \\ -1 & 1 \end{bmatrix} \tag{2.51}$$

using the Gram-Schmidt orthogonalization. Hence, using the rotational transformation, Equation (2.50) is transformed to V-space as

$$\tilde{g}(\mathbf{V}) = \frac{1}{4}\mathbf{V}^{\mathrm{T}}\begin{bmatrix} 5 & 0 \\ 0 & 3 \end{bmatrix}\mathbf{V} + \begin{bmatrix} 0 & 2\sqrt{2} \end{bmatrix}\mathbf{V} - 13 \tag{2.52}$$

and is approximated as a hyperbolic surface given by

$$\frac{\tilde{g}(\mathbf{V})}{\|\nabla g\|} \cong V_2 - 2.6849 + 0.1823V_1^2 \tag{2.53}$$

Using the hyperbolic surface and Equation (2.17), conventional SORM approximates the probability of failure as 1.2024% which overestimates the true probability of failure obtained using MCS as shown in Table 2.1. The MCS result in Table 2.1 is obtained using the original distribution which is the standard normal distribution in this example and using 10 million MCS-samples. Table 2.1 also shows that FORM underestimates the probability of failure. Error in conventional SORM is about 13% and this is mainly because the approximated hyperbolic surface overestimates the failure region as shown in Figure 2.4(a) which is "**Type 2 error**" explained in Section 2.2.2.3.

Table 2.1 Comparison of Probability of Failure Calculation

	FORM	SORM		MCS
		Conventional	Proposed	(10M)
P_F, %	0.3628	1.2024	1.0650	1.0642

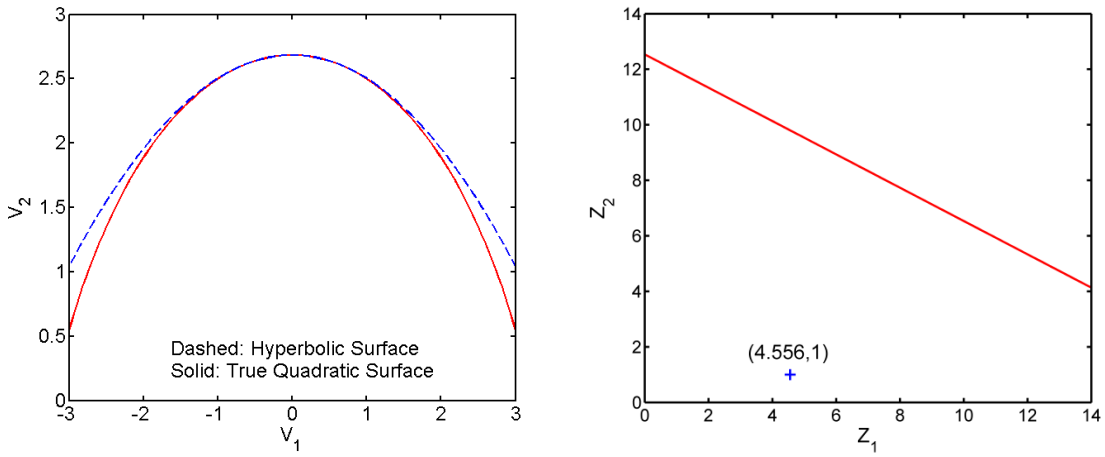

(a) V-space (b) χ^2-space

Figure 2.4 Performance Function in Transformed Space

On the other hand, to apply the proposed SORM to Equation (2.50), Equation (2.50) is transformed using an orthogonal transformation given by

$$\mathbf{u} = \mathbf{T}\mathbf{y} = \frac{1}{\sqrt{2}}\begin{bmatrix} 1 & 1 \\ 1 & -1 \end{bmatrix}\mathbf{y} \tag{2.54}$$

where **T** is the matrix of the eigenvectors of **H** and can be expressed in the transformed space as

$$\begin{aligned} \hat{g}(\mathbf{Y}) &= \frac{1}{2}\left(\lambda_1 Y_1^2 + \lambda_2 Y_2^2\right) + 2\sqrt{2}Y_1 - 13 = \frac{3}{4}Y_1^2 + \frac{5}{4}Y_2^2 + 2\sqrt{2}Y_1 - 13 \\ &= \frac{3}{4}\left(Y_1 + \frac{4}{3}\sqrt{2}\right)^2 + \frac{5}{4}Y_2^2 - \frac{47}{3} \end{aligned} \tag{2.55}$$

where λ_1 and λ_2 are the eigenvalues of **H**. Equation (2.55) is further transformed to χ^2-space as

$$\hat{g}_L(\mathbf{Z}) = \frac{3}{4}Z_1 + \frac{5}{4}Z_2 - \frac{47}{3} \tag{2.56}$$

where $Z_1 \sim \chi_1^2(\frac{32}{9})$ and $Z_2 \sim \chi_1^2(0)$, and it is shown in Figure 2.4(b). Using Equation (2.36), the probability of failure of the performance function in χ^2-space is obtained as

$$P_F = \int_{\hat{g}_L(\mathbf{z})>0} f_{\mathbf{Z}}(\mathbf{z})d\mathbf{z} = \int_0^{\infty}\left(\int_{\frac{188}{15}-0.6z_1}^{\infty} f_{Z_2}(z_2)dz_2\right) f_{Z_1}(z_1)dz_1$$
$$= 1 - \int_0^{\infty} F_{Z_2}\left(\frac{188}{15} - 0.6z_1\right) f_{Z_1}(z_1)dz_1 = 1.0650\% \tag{2.57}$$

Since the original performance function is quadratic in U-space which means that there is no Type 1 error, the probability of failure in Equation (2.57) obtained from the proposed SORM is exact, which can be seen in Table 2.1.

The same probability of failure with the one in Equation (2.57) can be obtained using a general chi-square distribution. Since both eigenvalues of **H** are positive, the PDF of $Q = \frac{3}{4}Z_1 + \frac{5}{4}Z_2$ is obtained using Equation (2.44) and the CDF can be obtained by numerically integrating the PDF. The PDF and CDF of Q are shown in Figure 2.5 and are compared with PDF and CDF obtained using MCS. From the figures, it can be seen that two distribution functions agree very well which should be true theoretically.

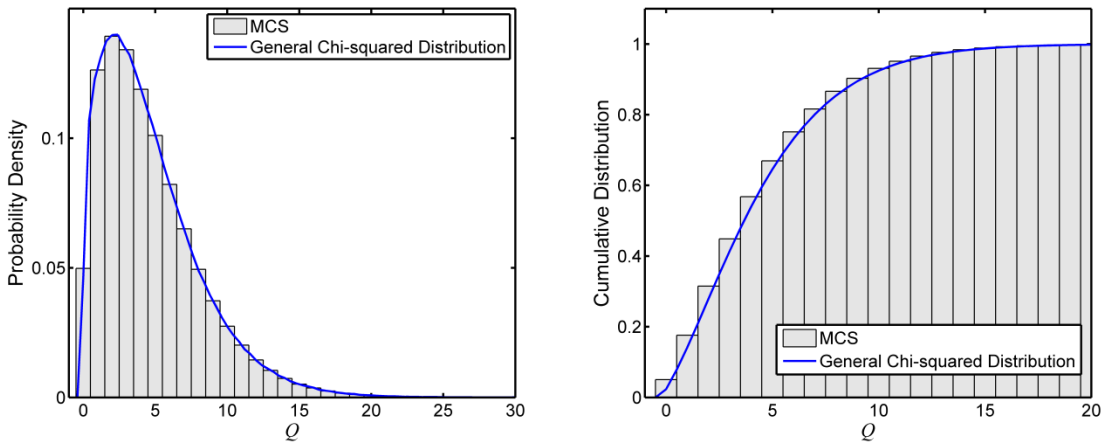

(a) PDF (b) CDF

Figure 2.5 Comparison of Distribution Function of Q

2.4.2 Four-Dimensional Example

To test the proposed SORM for higher dimensional problems, consider a 4-D quadratic performance function given by

$$G(\mathbf{X}) = -X_1^2 - X_2^2 - X_3^2 - X_4^2 + 10X_1 + 12X_2 + 12X_3 + 12X_4 - 43 \tag{2.58}$$

where $X_i \sim N(0,1)$ for $i = 1 \sim 4$ and statistically independent of each other. Equation (2.58) is expressed in U-space as

$$g(\mathbf{U}) = -\left(U_1 - 5\right)^2 - \left(U_2 - 6\right)^2 - \left(U_3 - 6\right)^2 - \left(U_4 - 6\right)^2 + 90 \tag{2.59}$$

and is expressed in χ^2-space as

$$\hat{g}_L(\mathbf{Z}) = -Z_1 - Z_2 - Z_3 - Z_4 + 90 \tag{2.60}$$

where $Z_1 \sim \chi_1^2(25)$, $Z_2 \sim \chi_1^2(36)$, $Z_3 \sim \chi_1^2(36)$, and $Z_4 \sim \chi_1^2(36)$. Or using a characteristic of chi-square variables, Equation (2.60) can be further simplified as

$$\hat{g}_L(\mathbf{Z}) = -Z + 90 \tag{2.61}$$

where $Z \sim \chi_4^2(133)$. Thus, the probability of failure of Equation (2.61) is exactly obtained using the CDF of Z as $F\left(90 \mid 4,133\right) = 1.4293\%$. Whereas, the probability of failure using conventional SORM in Equation (2.19) is 1.5281% which contains 6.85% error compared with the MCS result. Even if the conventional SORM result is more accurate than the FORM result as shown in Table 2.2, the proposed SORM shows much more accurate results than conventional SORM and FORM results without sacrificing efficiency. It should be noted that FORM overestimates the probability of failure in this example unlike the example used in Section 2.4.1. Figure 2.6 compares distribution functions of Equation (2.58) obtained from the proposed method and MCS.

Table 2.2 Comparison of Probability of Failure Calculation

	FORM	SORM		MCS
		Conventional	Proposed	(10M)
P_F, %	2.0477	1.5281	1.4293	1.4301

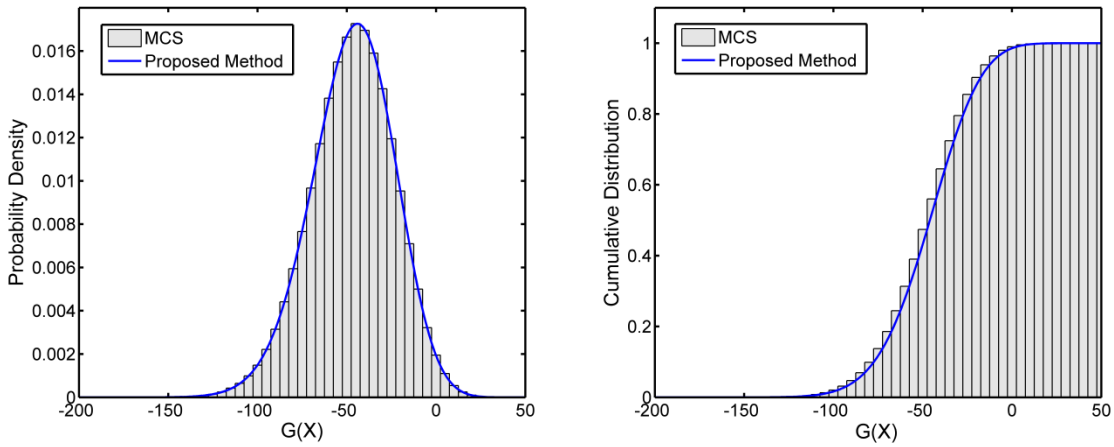

(a) PDF (b) CDF

Figure 2.6 Comparison of Distribution Function of G(**X**) in Equation (2.58)

2.4.3 High-Dimensional Engineering Example − Cantilever Tube

Since previous two numerical examples are low dimensional and mathematical ones, a high dimensional engineering example which was first used in the reference (Guo and Du 2009) and modified for the purpose of the paper is used in this section to verify the accuracy of the proposed second-order reliability method. As shown in Figure 2.7, the cantilever tube is subject to forces F_1, F_2 on xy-plane, x-directional axial force P, and torsion T on yz-plane. The maximum von Mises stress $\sigma_{\max}$ which will occur at the point A in Figure 2.7 is treated as a performance function. Consequently, since the performance function fails if $G(\mathbf{X}) > 0$, the limit state function is defined as

$$G(\mathbf{X}) = \sigma_{\max} - S_y \tag{2.62}$$

where S_y is the yield strength of the tube material.

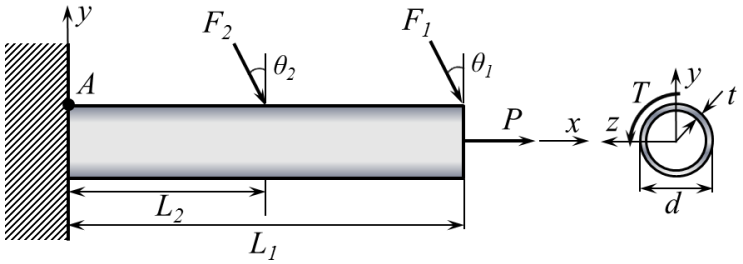

Figure 2.7 Cantilever Tube

From Figure 2.7, the maximum von Mises stress at A is given by

$$\sigma_{\max} = \sqrt{\sigma_x^2 + 3\tau_{xz}^2} \tag{2.63}$$

where the normal stress σ_x is obtained as

$$\sigma_x = \frac{P + F_1 \sin\theta_1 + F_2 \sin\theta_2}{\frac{\pi}{4}\left[d^2 - (d-2t)^2\right]} + \frac{(F_1 L_1 \cos\theta_1 + F_2 L_2 \cos\theta_2)d}{2 \times \frac{\pi}{64}\left[d^4 - (d-2t)^4\right]} \tag{2.64}$$

and the shear stress τ_{xz} is obtained as

$$\tau_{xz} = \frac{Td}{4 \times \frac{\pi}{64}\left[d^4 - (d-2t)^4\right]}, \tag{2.65}$$

respectively. Properties of 9 random variables used in Equations (2.62) ~ (2.65) are listed in Table 2.3. In this example, two angles are assumed to be fixed at $\theta_1 = 5^\circ$ and $\theta_2 = 10^\circ$.

Table 2.3 Properties of Random Variables

Random Variables	Mean	Standard Deviation	Distribution Type
X_1 (t)	4 mm	0.04 mm	Normal
X_2 (d)	40 mm	0.4 mm	Normal
X_3 (L_1)	120 mm	6 mm	Normal
X_4 (L_2)	60 mm	3 mm	Normal
X_5 (F_1)	3.0 kN	0.3 kN	Normal
X_6 (F_2)	3.0 kN	0.3 kN	Normal
X_7 (P)	12.0 kN	1.2 kN	Normal
X_8 (T)	90.0 Nm	9.0 Nm	Normal
X_9 (S_y)	220.0 MPa	22.0 MPa	Normal

Table 2.4 compares probability of failure calculations obtained from FORM, two conventional SORMs and proposed SORM, and MCS. For two conventional SORMs, Equation (2.17) proposed by Hohenbichler and Rackwitz and Equation (2.19) proposed by Breitung are used. As shown in Table 2.4, the probability of failure by FORM is 3.2812, which means the reliability index β is 1.841. Table 2.4 also shows that the performance function in Equation (2.62) is almost linear which means Type 1 error is very small since there is not much difference between probabilities of failure by FORM and SORM, which are all very close to the MCS result obtained using 100 million MCS-samples. The probability of failure using the proposed

methods explained in Sections 2.3.2 & 2.3.3 is also very close to the MCS result and conventional SORM results in this example. Again, this is because the curvature of the performance function at MPP is almost zero and thus Type 1,2, and 3 errors are almost zero in this example.

Table 2.4 Comparison of Probability of Failure Calculation

	FORM	SORM			MCS
		Breitung	Hohenbichler	Proposed	(100M)
, %	3.2812	3.2865	3.2884	3.2898	3.2907

2.5 Conclusions

To improve the accuracy of reliability analysis using SORM, two approaches to use numerical integration of the linear combination of non-central chi-square variables and to use the CDF of the linear combination which is called a general chi-square variable for the probability of failure calculation are proposed. Since it only includes an error due to approximating a general nonlinear limit state function by a quadratic function at MPP in U-space called Type 1 error, the proposed method always shows more accurate reliability analysis than conventional SORM. Furthermore, computational cost of the proposed method for the reliability analysis is negligible compared with the MPP search once a quadratic approximation is available since the PDF of non-central chi-square variables and the CDF of general chi-square variables are analytically available. Numerical examples verify that the proposed method is more accurate than FORM and conventional SORM when compared with MCS results.

Chapter 3. Probabilistic Sensitivity Analysis for Novel Second-Order Reliability Method (SORM) Using Non-Central or Generalized Chi-Squared Distributions

3.1 Introduction

To carry out RBDO utilizing reliability analysis method, sensitivities of probabilistic constraints with respect to design variables, which are the mean of input random variables, are required. Many works have been devoted to derive the sensitivity of the probabilistic constraint (Ditlevsen and Madsen 1996; Lee *et al.* 2009; Lee *et al.* 2011; Lee *et al.* 2011; Hohenbichler and Rackwitz 1986; Rahman and Wei 2008; Madsen *et al.* 1986). Thus, the study in this chapter presents the sensitivity analysis of the novel SORM for more accurate RBDO. Since the novel SORM performs reliability analysis at MPP, sensitivities of probabilistic constraints at MPP with respect to the mean of random variables are derived during the sensitivity analysis. To calculate the sensitivity, it is necessary to evaluate probability density function (PDF) of a linear combination of non-central chi-square variables, which is obtained utilizing the general chi-squared distribution.

3.2 Sensitivity Analysis Using Novel SORM

In Section 2.3, $Q = \sum_{k=1}^{N} \lambda_k \left(Y_k + \delta_k \right)^2$ in Equation (2.25) is a general chi-square variables whose PDF and CDF are given in Section 2.3.2 and Section 2.3.3, respectively. The Probability of failure in Equation (2.25) can be rewritten as

$$P_F \cong P\left[Q > \sum_{k=1}^{N} \lambda_k \delta_k^2 - 2\|\nabla g\| a_0 \right] = 1 - F_Q\left(\sum_{k=1}^{N} \lambda_k \delta_k^2 - 2\|\nabla g\| a_0 \right) \tag{3.1}$$

where $F_Q(\bullet)$ is the CDF of Q. The sensitivity of the probability of failure with respect to a distribution parameter θ can be obtained by taking derivative of Equation (3.1) as

$$\frac{dP_F}{d\theta} = -f_Q(q,\boldsymbol{\delta})\frac{dq}{d\theta} - \sum_{i=1}^{N}\frac{dF_Q(q,\boldsymbol{\delta})}{d\delta_i}\frac{d\delta_i}{d\theta} \tag{3.2}$$

denoting $\sum_{k=1}^{N}\lambda_k\delta_k^2 - 2\|\nabla g\|a_0$ in Equation (3.1) as *q*. In Equation (3.2), $f_Q(\bullet)$ is the PDF of Q, which is obtained using a general chi-squared distribution explained in Section 2.3.3. Here, it should be noted that $F_Q(\bullet)$ in Equation (3.2) is not only a function of *q* but also a function of $\boldsymbol{\delta}$, which is the vector of the non-centrality parameter defined in Equation (2.26).

To calculate Equation (3.2), $\frac{d\lambda_k}{d\theta}$ needs to be obtained based on the definition of *q*, which requires third-order derivative of $g(\mathbf{U})$ or derivative of **H**. Consider a generalized eigenvalue problem of the Hessian matrix **H** such that $\mathbf{HT} = \boldsymbol{\lambda}\mathbf{AT}$ where $\boldsymbol{\lambda}$ and $\mathbf{T}$ are the diagonal matrix of the eigenvalues and the matrix of the eigenvectors of **H**, respectively, and **A** represents the matrix that is symmetric and positive definite. Then, according to the eigenvalue perturbation theory, $\frac{d\lambda_k}{d\theta}$ is obtained using the property of the matrix **A** as (Trefethen 1997)

$$\begin{aligned}\frac{d\lambda_k}{d\theta} &= \sum_{i=1}^{N}\sum_{j=1}^{N}\frac{\partial\lambda_k}{\partial H_{ij}}\frac{\partial H_{ij}}{\partial\theta} = \sum_{i=1}^{N}\sum_{j=1}^{N}\frac{\partial}{\partial H_{ij}}\left(\lambda_{0k} + \mathbf{T}_k^{\mathrm{T}}\left(\delta\mathbf{H} - \lambda_k\delta\mathbf{A}\right)\mathbf{T}_k\right)\frac{\partial H_{ij}}{\partial\theta} \\ &= \sum_{i=1}^{N}\sum_{j=1}^{N}T_{k_i}T_{k_j}\left(2-\delta_{ij}\right)\frac{\partial H_{ij}}{\partial\theta}\end{aligned} \tag{3.3}$$

where H_{ij} is the element of $\mathbf{H}$ at the i^{th} row and the j^{th} column; λ_{0k} is the eigenvalue of $\mathbf{H}$ at the current design; $\mathbf{T}_k$ is the k^{th} eigenvector corresponding to λ_k; T_{k_i} is the i^{th} component of $\mathbf{T}_k$; all of the δ terms are perturbed quantities which is much smaller than the corresponding quantities; and δ_{ij} is the Kronecker delta. Since the third-order derivative of the Hessian matrix $\mathbf{H}$ is not available in SORM, it is assumed in the study in this chapter that $\frac{\partial H_{ij}}{\partial\theta}$ in Equation (3.3) is 0, which leads to $\frac{d\lambda_k}{d\theta} = 0$.

Using the assumption above, the sensitivity of the probability of failure in Equation (3.1) can be approximated as

$$\begin{aligned}\frac{dP_F}{d\theta} \cong -2 f_Q(q,\boldsymbol{\delta})\left(\sum_{k=1}^{N} \lambda_k \delta_k \frac{d\delta_k}{d\theta} - \frac{d\|\nabla g\|}{d\theta} a_0 - \|\nabla g\| \frac{da_0}{d\theta} \right) \\ - \sum_{i=1}^{N} \frac{dF_Q(q,\boldsymbol{\delta})}{d\delta_i} \left(\frac{\|\nabla g\|}{\lambda_i} \frac{da_{1_i}}{d\theta} + \frac{a_{1_i}}{\lambda_i} \frac{d\|\nabla g\|}{d\theta} \right)\end{aligned} \tag{3.4}$$

Equation (3.4) can be then rewritten based on the definition of δ stated in Equation (2.26) as

$$\begin{aligned}\frac{dP_F}{d\theta} \cong -2 f_Q(q,\boldsymbol{\delta})\left(\|\nabla g\| \boldsymbol{\delta}^T \frac{d\mathbf{a_1}}{d\theta} + \frac{d\|\nabla g\|}{d\theta} \boldsymbol{\delta}^T \mathbf{a_1} - \frac{d\|\nabla g\|}{d\theta} a_0 - \|\nabla g\| \frac{da_0}{d\theta} \right) \\ - \sum_{i=1}^{N} \frac{dF_Q(q,\boldsymbol{\delta})}{d\delta_i} \left(\frac{\|\nabla g\|}{\lambda_i} \frac{da_{1_i}}{d\theta} + \frac{a_{1_i}}{\lambda_i} \frac{d\|\nabla g\|}{d\theta} \right)\end{aligned} \tag{3.5}$$

As shown in Equation (3.5), $\frac{d\mathbf{a_1}}{d\theta}$, $\frac{d\|\nabla g\|}{d\theta}$, and $\frac{da_0}{d\theta}$ need to be derived for the sensitivity analysis of the probability of failure. From Equation (2.22) and the assumption made in the previous paragraph, $\frac{d\mathbf{a_1}}{d\theta}$ in Equation (3.5) becomes

$$\begin{aligned}\frac{d\mathbf{a_1}}{d\theta} &\cong \mathbf{T}^T \left(\mathbf{I} - \beta \frac{\mathbf{H}}{\|\nabla g\|} \right) \frac{d\boldsymbol{\alpha}}{d\theta} - \mathbf{T}^T \mathbf{H} \boldsymbol{\alpha} \frac{d}{d\theta} \left(\frac{\beta}{\|\nabla g\|} \right) \\ &= \mathbf{T}^T \left(\mathbf{I} - \beta \frac{\mathbf{H}}{\|\nabla g\|} \right) \frac{d\boldsymbol{\alpha}}{d\theta} - \frac{\mathbf{T}^T \mathbf{H} \boldsymbol{\alpha}}{\|\nabla g\|} \frac{d\beta}{d\theta} + \frac{\beta \mathbf{T}^T \mathbf{H} \boldsymbol{\alpha}}{\|\nabla g\|^2} \frac{d\|\nabla g\|}{d\theta}\end{aligned} \tag{3.6}$$

where $\frac{d\boldsymbol{\alpha}}{d\theta}$ can be derived based on the definition of $\boldsymbol{\alpha}$ stated in Equation (2.8) as

$$\frac{d\boldsymbol{\alpha}}{d\theta} = \frac{d}{d\theta}\left(\frac{\nabla g}{\|\nabla g\|} \right) = \frac{1}{\|\nabla g\|} \frac{d\nabla g}{d\theta} - \frac{\nabla g}{\|\nabla g\|^2} \frac{d\|\nabla g\|}{d\theta} = \frac{1}{\|\nabla g\|} \frac{d\nabla g}{d\theta} - \frac{\boldsymbol{\alpha}}{\|\nabla g\|} \frac{d\|\nabla g\|}{d\theta} \tag{3.7}$$

Utilizing the chain rule, $\frac{d\nabla g}{d\theta}$ in Equation (3.7) can be written as

$$\frac{d\nabla g}{d\theta} = \frac{\partial \nabla g}{\partial \theta} + \mathbf{H} \frac{d\mathbf{u}^*}{d\theta} \tag{3.8}$$

where $\frac{d\mathbf{u}^*}{d\theta}$ can be obtained by taking derivative of $\mathbf{u}^*$ in Equation (2.8) with respect to θ as

$$\frac{d\mathbf{u}^*}{d\theta} = \frac{d\beta}{d\theta}\boldsymbol{\alpha} + \beta\frac{d\boldsymbol{\alpha}}{d\theta} \tag{3.9}$$

$\frac{d\|\nabla g\|}{d\theta}$ in Equation (3.7) can be obtained as (Lee *et al.* 2009)

$$\frac{d\|\nabla g\|}{d\theta} = \boldsymbol{\alpha}^T \frac{d\nabla g}{d\theta} \tag{3.10}$$

Then, using Equations (3.8), (3.9) and (3.10), Equation (3.7) can be rewritten as

$$\frac{d\boldsymbol{\alpha}}{d\theta} = \frac{\mathbf{I} - \boldsymbol{\alpha}\boldsymbol{\alpha}^T}{\|\nabla g\|}\left[\frac{\partial \nabla g}{\partial \theta} + \mathbf{H}\left(\frac{d\beta}{d\theta}\boldsymbol{\alpha} + \beta\frac{d\boldsymbol{\alpha}}{d\theta}\right)\right] \tag{3.11}$$

Thus, it is obtained

$$\frac{d\boldsymbol{\alpha}}{d\theta} = \left[\mathbf{I} - \frac{\beta\left(\mathbf{I} - \boldsymbol{\alpha}\boldsymbol{\alpha}^T\right)\mathbf{H}}{\|\nabla g\|}\right]^{-1}\frac{\left(\mathbf{I} - \boldsymbol{\alpha}\boldsymbol{\alpha}^T\right)}{\|\nabla g\|}\left(\frac{\partial \nabla g}{\partial \theta} + \frac{d\beta}{d\theta}\mathbf{H}\boldsymbol{\alpha}\right) \tag{3.12}$$

The limit-state function in the original X-space is expressed as (Ditlevsen and Madsen 1996)

$$G(\mathbf{x}) = g(\mathbf{u};\theta) \tag{3.13}$$

Due to the fact that distribution parameter θ has no influence on the limit state function expressed in Equation (3.13), derivative of the left hand side of Equation (3.13) with respect to θ is zero, which implies

$$\frac{dg(\mathbf{u};\theta)}{d\theta} = \frac{\partial g}{\partial \theta} + \nabla^T g\frac{d\mathbf{u}}{d\theta} = 0 \tag{3.14}$$

Thus, $\frac{\partial \nabla g}{\partial \theta}$ is derived using Equation (3.14) as

$$\frac{\partial \nabla g}{\partial \theta} = \nabla\frac{\partial g}{\partial \theta} = -\nabla\left(\nabla^T g\frac{d\mathbf{u}}{d\theta}\right) \tag{3.15}$$

By inserting Equation (3.15) into Equation (3.12), we can obtain

$$\frac{d\boldsymbol{\alpha}}{d\theta}=\left[\mathbf{I}-\frac{\beta\left(\mathbf{I}-\boldsymbol{\alpha}\boldsymbol{\alpha}^T\right)\mathbf{H}}{\|\nabla g\|}\right]^{-1}\frac{\left(\mathbf{I}-\boldsymbol{\alpha}\boldsymbol{\alpha}^T\right)}{\|\nabla g\|}\left[-\nabla\left(\nabla^T g\frac{d\mathbf{u}}{d\theta}\right)+\frac{d\beta}{d\theta}\mathbf{H}\boldsymbol{\alpha}\right] \tag{3.16}$$

The reliability index β can be expressed based on Equation (2.8) as

$$\beta=\boldsymbol{\alpha}^T\mathbf{u}^* \tag{3.17}$$

Then, by taking derivative of Equation (3.17) with respect to θ yields

$$\frac{d\beta}{d\theta}=\frac{d\boldsymbol{\alpha}^T}{d\theta}\mathbf{u}^*+\boldsymbol{\alpha}^T\frac{d\mathbf{u}^*}{d\theta}=\boldsymbol{\alpha}^T\frac{d\mathbf{u}^*}{d\theta} \tag{3.18}$$

owing to the fact that $\frac{d\boldsymbol{\alpha}^T}{d\theta}$ and $\boldsymbol{\alpha}$ are mutually orthogonal and $\mathbf{u}^*=\beta\boldsymbol{\alpha}$. The orthogonality can be verified by differentiation of $\boldsymbol{\alpha}^T\boldsymbol{\alpha}=1$ or by

$$\begin{aligned}\frac{d\boldsymbol{\alpha}^T}{d\theta}\mathbf{u}^* &= \frac{d}{d\theta}\left[\nabla g\left(\nabla^T g\nabla g\right)^{-1/2}\right]^T\mathbf{u}^*\\ &= \left\{\frac{1}{\|\nabla g\|}\frac{d}{d\theta}(\nabla g)-\frac{\nabla g}{\|\nabla g\|^3}\left[\nabla^T g\frac{d}{d\theta}(\nabla g)\right]\right\}^T\mathbf{u}^*\\ &= \frac{\beta}{\|\nabla g\|^2}\frac{d}{d\theta}(\nabla g)^T\nabla g-\frac{\beta}{\|\nabla g\|^2}\left[\nabla^T g\frac{d}{d\theta}(\nabla g)\right]\\ &= 0.\end{aligned} \tag{3.19}$$

The limit-state function at MPP in U-space is given by $g\left(\mathbf{u}^*;\theta\right)=0$, and the differentiation of it gives

$$\frac{dg}{d\theta}=\frac{\partial g}{\partial\theta}+\nabla^T g\frac{d\mathbf{u}^*}{d\theta}=0 \tag{3.20}$$

Then, dividing both sides of Equation (3.20) by $\|\nabla g\|$ gives

$$\frac{1}{\|\nabla g\|}\left[\frac{\partial g}{\partial\theta}+\nabla^T g\frac{d\mathbf{u}^*}{d\theta}\right]=\frac{1}{\|\nabla g\|}\frac{\partial g}{\partial\theta}+\frac{\nabla^T g}{\|\nabla g\|}\frac{d\mathbf{u}^*}{d\theta}=\frac{1}{\|\nabla g\|}\frac{\partial g}{\partial\theta}+\boldsymbol{\alpha}^T\frac{d\mathbf{u}^*}{d\theta}=0 \tag{3.21}$$

Using Equations (3.14) and (3.21), Equation (3.18) can be rewritten as

$$\frac{d\beta}{d\theta}=-\frac{1}{\|\nabla g\|}\frac{\partial g}{\partial\theta}=\left[\boldsymbol{\alpha}^T\frac{d\mathbf{u}}{d\theta}\right]_{\mathbf{u}=\mathbf{u}^*} \tag{3.22}$$

Finally, $\frac{da_0}{d\theta}$ in Equation (3.5) can be obtained using Equation (2.21) as

$$\begin{aligned}\frac{da_0}{d\theta} &\cong -\frac{d\beta}{d\theta} + \frac{\beta}{\|\nabla g\|}\frac{d\beta}{d\theta}\boldsymbol{\alpha}^{\mathrm{T}}\mathbf{H}\boldsymbol{\alpha} + \frac{\beta^2}{2}\frac{\frac{d\left(\boldsymbol{\alpha}^{\mathrm{T}}\mathbf{H}\boldsymbol{\alpha}\right)}{d\theta}\|\nabla g\| - \boldsymbol{\alpha}^{\mathrm{T}}\mathbf{H}\boldsymbol{\alpha}\frac{d\|\nabla g\|}{d\theta}}{\|\nabla g\|^2} \\ &= -\frac{d\beta}{d\theta} + \frac{\beta}{\|\nabla g\|}\frac{d\beta}{d\theta}\boldsymbol{\alpha}^{\mathrm{T}}\mathbf{H}\boldsymbol{\alpha} + \frac{\beta^2}{\|\nabla g\|}\boldsymbol{\alpha}^{\mathrm{T}}\mathbf{H}\frac{d\boldsymbol{\alpha}}{d\theta} - \frac{\beta^2\boldsymbol{\alpha}^{\mathrm{T}}\mathbf{H}\boldsymbol{\alpha}}{2\|\nabla g\|^2}\frac{d\|\nabla g\|}{d\theta}\end{aligned} \tag{3.23}$$

Then, using Equations (3.7) and (3.10), Equation (3.23) can be expressed as

$$\frac{da_0}{d\theta} \cong -\frac{d\beta}{d\theta} + \frac{\beta}{\|\nabla g\|}\frac{d\beta}{d\theta}\boldsymbol{\alpha}^{\mathrm{T}}\mathbf{H}\boldsymbol{\alpha} + \frac{\beta^2}{\|\nabla g\|}\left[\boldsymbol{\alpha}^{\mathrm{T}}\mathbf{H} - \frac{\boldsymbol{\alpha}^{\mathrm{T}}\mathbf{H}\boldsymbol{\alpha}}{2}\boldsymbol{\alpha}^{\mathrm{T}}\left(\mathbf{I} - \boldsymbol{\alpha}\boldsymbol{\alpha}^{T}\right)^{-1}\right]\frac{d\boldsymbol{\alpha}}{d\theta} \tag{3.24}$$

The sensitivity of the probability of failure with respect to θ is therefore given by

$$\begin{aligned}\frac{dP_F}{d\theta} &= -2f_Q(q,\boldsymbol{\delta})\left(\|\nabla g\|\boldsymbol{\delta}^T\frac{d\mathbf{a_1}}{d\theta} + \frac{d\|\nabla g\|}{d\theta}\boldsymbol{\delta}^T\mathbf{a_1} - \frac{d\|\nabla g\|}{d\theta}a_0 - \|\nabla g\|\frac{da_0}{d\theta}\right) \\ &\quad -\sum_{i=1}^{N}\frac{dF_Q(q,\boldsymbol{\delta})}{d\delta_i}\left(\frac{\|\nabla g\|}{\lambda_i}\frac{da_{1_i}}{d\theta} + \frac{a_{1_i}}{\lambda_i}\frac{d\|\nabla g\|}{d\theta}\right) \\ &= -2f_Q(q)\left(\|\nabla g\|\boldsymbol{\delta}^T\frac{d\mathbf{a_1}}{d\theta} + \boldsymbol{\alpha}^T\frac{d\nabla g}{d\theta}\left(\boldsymbol{\delta}^T\mathbf{a_1} - a_0\right) - \|\nabla g\|\frac{da_0}{d\theta}\right) \\ &\quad -\sum_{i=1}^{N}\frac{dF_Q(q,\boldsymbol{\delta})}{d\delta_i}\left(\frac{\|\nabla g\|}{\lambda_i}\frac{da_{1_i}}{d\theta} + \frac{a_{1_i}}{\lambda_i}\frac{d\|\nabla g\|}{d\theta}\right)\end{aligned} \tag{3.25}$$

where

$$\frac{d\mathbf{a_1}}{d\theta} = \mathbf{T}^T\left(\mathbf{I} - \beta\frac{\mathbf{H}}{\|\nabla g\|}\right)\frac{d\boldsymbol{\alpha}}{d\theta} - \frac{\mathbf{T}^T\mathbf{H}\boldsymbol{\alpha}}{\|\nabla g\|}\frac{d\beta}{d\theta} + \frac{\beta\mathbf{T}^T\mathbf{H}\boldsymbol{\alpha}\boldsymbol{\alpha}^T}{\|\nabla g\|^2}\frac{d\nabla g}{d\theta} \tag{3.26}$$

$$\frac{d\nabla g}{d\theta} = -\nabla\left(\nabla^T g\frac{d\mathbf{u}}{d\theta}\right) + \mathbf{H}\left(\frac{d\beta}{d\theta}\boldsymbol{\alpha} + \beta\frac{d\boldsymbol{\alpha}}{d\theta}\right) \tag{3.27}$$

and $\frac{d\|\nabla g\|}{d\theta}$, $\frac{d\beta}{d\theta}$, $\frac{d\boldsymbol{\alpha}}{d\theta}$, and $\frac{da_0}{d\theta}$ are obtained from Equations (3.10), (3.22), (3.16) and (3.24), respectively. $\frac{d\mathbf{u}}{d\theta}$ in Equations (3.22) and (3.27) is obtained from the Rosenblatt transformation and its i^{th} component is expressed as

$$\frac{du_i}{d\theta} = \frac{d\Phi^{-1}\left[F_{X_i}\left(x_i;\theta\right)\right]}{d\theta} \tag{3.28}$$

For normally distributed independent random variables and when the distribution parameter is the mean of the j^{th} random variable, $\frac{du_i}{d\theta}$ in Equation (3.28) becomes

$$\frac{du_i}{d\mu_j} = -\delta_{ij}\frac{1}{\sigma_j} \tag{3.29}$$

where δ_{ij} is the Kronecker delta.

To calculate Equation (3.25), $\frac{dF_Q(q,\boldsymbol{\delta})}{d\delta_i}$ is also required, which is obtained using FDM as

$$\frac{dF_Q(q,\boldsymbol{\delta})}{d\delta_i} = \frac{F_Q\left(q,\delta_i^{'}\right) - F_Q\left(q,\delta_i\right)}{\delta_i^{'} - \delta_i} \tag{3.30}$$

where $\delta_i^{'}$ is obtained perturbing δ_i by very small amount. To calculate $\frac{dF_Q(q,\boldsymbol{\delta})}{d\delta_i}$ in Equation (3.30), $F_Q\left(q,\delta_i\right)$ should be obtained first using general chi-squared distribution explained in Section 2.3.3. Then, $F_Q\left(q,\delta_i^{'}\right)$ is calculated after setting the appropriate value for $\delta_i^{'}$. During the calculation of $F_Q\left(q,\delta_i^{'}\right)$, another MPP search, which is an iterative algorithm and thus can significantly affect efficiency of the calculation, is not involved. Thus, the efficiency is not much reduced due to the sensitivity analysis using FDM. Additionally, $\frac{dF_Q(q,\boldsymbol{\delta})}{d\delta_i}$ in Equation (3.30) can be accurately calculated setting very small perturbation size for $\delta_i^{'}$ since $F_Q\left(q,\delta_i\right)$ can be very accurately calculated using the exact CDF proposed in the reference (Provost and Rudiuk 1996). For example, if the accuracy of 10 decimal digits for $\frac{dF_Q(q,\boldsymbol{\delta})}{d\delta_i}$ is required, it can be obtained by setting the perturbation size as the order of 10^{-10}.

All terms used for the sensitivity evaluation summarized in Equation (3.25) are available from the probability of failure evaluation using the novel SORM except $\frac{dF_Q(q,\boldsymbol{\delta})}{d\delta_i}$ which requires FDM. As the dimension of a problem increases, computation time for the evaluation of Equation (3.30) could be increased. However, since the CDF of *Q* can be analytically available as indicated in the reference (Provost and Rudiuk 1996), the computation time for Equation (3.30) is negligible. This means that the sensitivity analysis proposed in the paper does not require additional computationally intensive computer simulations. Hence, it can be concluded that the proposed sensitivity analysis is computationally efficient since it does not require additional function evaluations.

3.3 Numerical Examples

The first three numerical studies are carried out in this section to verify the sensitivity analysis proposed in Section 3.2 for low-, medium-, and high-dimensional performance functions. The last numerical study is carried out to test the sensitivity of a higher-order performance function in terms of how the proposed assumption that the Hessian is constant affects the accuracy of the sensitivity calculation.

3.3.1 Sensitivity Using Novel SORM for Two-dimensional Performance Function

In this numerical example, the sensitivity of the probability of failure with respect to the design point is obtained using the analytic derivation in Section 3.2 for the two-dimensional performance function. The means of the random variables are used as design variables.

Consider the following 2D performance function shown in Figure 3.1 and given in X-space as

$$G(\mathbf{X}) = -X_1^2 - 2X_1 - X_2^2 - 2X_2 + 0.5X_1X_2 + 13, \tag{3.31}$$

where the properties of X_1 and X_2 are listed in Table 3.1.

Table 3.1 Property of Random Variables

Variables	Distribution Type	μ	σ
X_1	Normal	–3	1
X_2	Lognormal	4	1

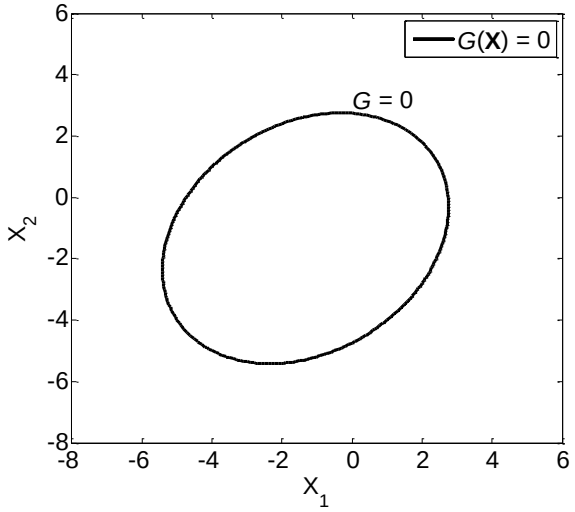

Figure 3.1 Performance Function Given in Equation (3.31)

The performance function in Equation (3.31) can be transformed to U-space using Rosenblatt transformation as

$$G(\mathbf{U}) = \left(\mu_1 + \sigma_1 U_1\right)^2 + 2\left(\mu_1 + \sigma_1 U_1\right) + e^{\left(2\overline{\mu}_2 + 2\overline{\sigma}_2 U_2\right)} + 2e^{\left(\overline{\mu}_2 + \overline{\sigma}_2 U_2\right)} - 0.5\left(\mu_1 + \sigma_1 U_1\right)e^{\left(\overline{\mu}_2 + \overline{\sigma}_2 U_2\right)} - 13 \quad (3.32)$$

where $\overline{\sigma}_2 = \sqrt{\ln\left[1 + \left(\frac{\sigma_2}{\mu_2}\right)^2\right]}$ and $\overline{\mu}_2 = \ln\left(\mu_2\right) - 0.5\overline{\sigma}_2^2$. Equation (3.32) is further transformed to χ^2-space as (Lee *et al.* 2012)

$$\hat{g}_L\left(\mathbf{Z}\right) = \lambda_1 Z_1 + \lambda_2 Z_2 - q \quad (3.33)$$

where λ_1, λ_2, and q are -2.0688, -0.6658, and -31.3333, respectively, and $Z_1 \sim \chi_1^2\left(11.7073\right)$ and $Z_2 \sim \chi_1^2\left(56.8452\right)$. The probability of failure then can be calculated using Equation (3.33) and numerical integration as (Lee *et al.* 2012)

$$P_F = \int_{\hat{g}_L(\mathbf{z})>0} f_{\mathbf{Z}}(\mathbf{z})d\mathbf{z} = \int_0^{\infty}\left(\int_{\frac{q}{\lambda_2}-\frac{\lambda_1 z_1}{\lambda_2}}^{\infty} f_{Z_2}(z_2)dz_2\right) f_{Z_1}(z_1)dz_1$$
$$= \int_0^{\infty} F_{Z_2}\left(\frac{q}{\lambda_2}-\frac{\lambda_1 z_1}{\lambda_2}\right) f_{Z_1}(z_1)dz_1 = 1.15\% \tag{3.34}$$

The sensitivity of the probability of failure in Equation (3.34) with respect to the means of the random variables is then calculated using Equation (3.2), the general chi-squared distribution in Section 2.3.3, and the analytic derivation in Section 3.2. The parameters necessary to calculate $\frac{dP_F}{d\mu_1}$ are obtained based on the derivation in Section 3.2, which are shown in Table 3.2. Using the result, $\frac{dP_F}{d\mu_1}$ is calculated as 0.0152. Likewise, $\frac{dP_F}{d\mu_2}$ is calculated as -0.0383.

Table 3.2 Numerical Values of Parameters

Term/Parameter	Numerical Value
$f_Q(q,\boldsymbol{\delta})$	0.003942
$dq / d\mu_1$	0
δ_i	$(3.4216, -7.5396)$
$dF_Q(q,\boldsymbol{\delta}) / d\delta_i$	$(0.0205, -0.0216)$
$d\delta_i / d\mu_1$	$(-1.8028, -5.9686)$

In terms of accuracy, the calculated sensitivity is then compared with the sensitivity obtained by FDM using MCS, which is shown in Table 3.3. According to Table 3.3, the sensitivity calculated based on the sensitivity analysis in Section 3.2 is almost identical with the sensitivity obtained by FDM using MCS, which is because the performance function in this example is perfectly quadratic.

Table 3.3 Comparison of Sensitivity Calculation

	Proposed Sensitivity	FDM using MCS (10 M)
$dP_F / d\mu_1$	0.0152	0.0152
$dP_F / d\mu_2$	–0.0383	–0.0382

3.3.2 Sensitivity Using Novel SORM for Medium-Dimensional Performance Function

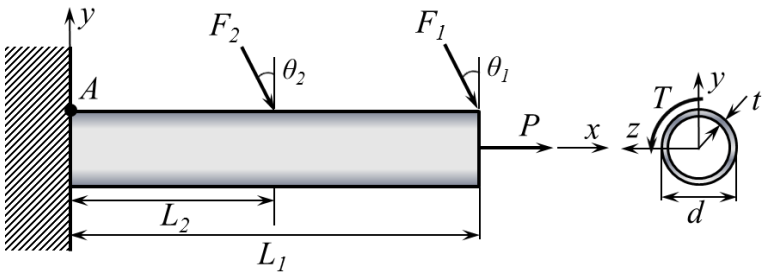

Figure 3.2 Schematic Diagram of Cantilever Tube

In this numerical example, the sensitivity of the probability of failure with respect to the design point is obtained using the analytic derivation in Section 3.2 for the medium-dimensional performance function. Consider the cantilever tube shown in Figure 3.2 subjected to external forces F_1, F_2, and P, and torsion T (Du 2007). The 8D performance function is defined as the difference between the yield strength of $190\,\text{MPa}$ and the maximum stress $\sigma_{\max}$, which is given as

$$G(\mathbf{X}) = \sigma_{\max} - 190\,\text{MPa} \tag{3.35}$$

where $\sigma_{\max}$ is the maximum von Mises stress on the top surface of the tube at the root, which is given by

$$\sigma_{\max} = \sqrt{\sigma_x^2 + 3\tau_{zx}^2} \tag{3.36}$$

where the normal stress σ_x can be obtained as

$$\sigma_x = \frac{P + F_1 \sin\theta_1 + F_2 \sin\theta_2}{\frac{\pi}{4}\left[d^2 - (d-2t)^2\right]} + \frac{(F_1 L_1 \cos\theta_1 + F_2 L_2 \cos\theta_2)\, d}{2 \times \frac{\pi}{64}\left[d^4 - (d-2t)^4\right]} \tag{3.37}$$

and the shear stress τ_{xz} can be obtained as

$$\tau_{xz} = \frac{Td}{4 \times \frac{\pi}{64}\left[d^4 - (d-2t)^4\right]} \tag{3.38}$$

respectively. The properties of the 8 random variables used in Equations (3.35)~(3.38) are given in Table 3.4 and they are all statistically independent to each other. Two angles are assumed to be fixed at $\theta_1 = 5^\circ$ and $\theta_2 = 10^\circ$.

Table 3.4 Properties of Random Variables

Variables	Mean	Standard Deviation	Distribution Type
$X_1(t)$	4 mm	0.04 mm	Normal
$X_2(d)$	40 mm	0.4 mm	Normal
$X_3(L_1)$	120 mm	$\sqrt{3}$ mm	Normal
$X_4(L_2)$	60 mm	$\sqrt{3}/2$ mm	Normal
$X_5(F_1)$	3.0 kN	0.3 kN	Normal
$X_6(F_2)$	3.0 kN	0.3 kN	Normal
$X_7(P)$	12.0 kN	1.2 kN	Normal
$X_8(T)$	90.0 N·m	9.0 N·m	Normal

Using the information in Table 3.4 and the analytic derivation in Section 3.2, the sensitivity is calculated. The obtained sensitivity is then compared with the sensitivity obtained by FDM using MCS. Based on the mostly small percent errors shown in Table 3.5, it can be concluded that the proposed sensitivity analysis accurately calculates sensitivity. For some random variables, relatively large errors compared to the previous example are generated. Considering $\frac{dF_Q(q,\boldsymbol{\delta})}{d\delta_i}$ can be calculated with negligible amount of an error using the FDM in Equation (3.30) with small perturbation size, it is considered that the errors are mostly generated due to the nonlinearity of the performance function.

Table 3.5 Comparison of Sensitivity Calculation

	Proposed Sensitivity	FDM using MCS (10 M)	Error (%)
$dP_F / d\mu_1$	-4.84×10^{2}	-4.64×10^{2}	4.31
$dP_F / d\mu_2$	-1.39×10^{2}	-1.37×10^{2}	1.90
$dP_F / d\mu_3$	1.22×10^{1}	1.21×10^{1}	9.99×10^{-1}
$dP_F / d\mu_4$	1.14×10^{1}	1.14×10^{1}	6.11×10^{-2}
$dP_F / d\mu_5$	4.39×10^{-4}	4.40×10^{-4}	3.43×10^{-1}
$dP_F / d\mu_6$	2.21×10^{-4}	2.21×10^{-4}	4.21×10^{-2}
$dP_F / d\mu_7$	2.98×10^{-5}	2.98×10^{-5}	1.76×10^{-1}
$dP_F / d\mu_8$	3.40×10^{-4}	3.51×10^{-4}	3.06

3.3.3 Sensitivity Using Novel SORM for High-Dimensional Performance Function

In this numerical example, the sensitivities of the probability of failures with respect to the design point are obtained using the analytic derivation in Section 3 for the high-dimensional performance function. The means of the random variables are used as design variables.

Consider the following 20D performance function, which is obtained by flipping the *Dixon & Price function* (Dixon and Price 1989) and setting its constant as $10^{7.66}$, given in X-space as

$$G(\mathbf{X}) = -(X_1 - 1)^2 - \sum_{i=2}^{20} i\left(2X_i^2 - X_{i-1}\right)^2 + 10^{7.66} \tag{3.39}$$

where $X_i \sim N(16,3)$.

Using the analytic derivation in Section 3, the sensitivity is calculated. The obtained sensitivity is then compared with the sensitivity obtained by FDM using MCS. As shown in Table 3.6, the percent errors are generally small, thus it can be concluded that the proposed sensitivity analysis can accurately calculate the sensitivity for the high-dimensional performance function. $dP_F / d\mu_1$ does not appear in Table 3.6 since its value is of the order of 10^{-6}, which is almost 0.

Table 3.6 Comparison of Sensitivity Calculation

	Proposed Sensitivity	FDM using MCS (10 M)	Error (%)
$dP_F / d\mu_2$	-1.21×10^{-3}	-1.24×10^{-3}	3.19
$dP_F / d\mu_3$	-2.52×10^{-3}	-2.57×10^{-3}	2.47
$dP_F / d\mu_4$	-2.95×10^{-3}	-3.02×10^{-3}	2.28
$dP_F / d\mu_5$	-4.05×10^{-3}	-4.19×10^{-3}	3.33
$dP_F / d\mu_6$	-4.50×10^{-3}	-4.60×10^{-3}	2.27
$dP_F / d\mu_7$	-5.43×10^{-3}	-5.35×10^{-3}	1.52
$dP_F / d\mu_8$	-5.81×10^{-3}	-5.98×10^{-3}	2.84
$dP_F / d\mu_9$	-6.57×10^{-3}	-6.98×10^{-3}	5.84
$dP_F / d\mu_{10}$	-7.30×10^{-3}	-7.49×10^{-3}	2.53
$dP_F / d\mu_{11}$	-8.05×10^{-3}	-8.43×10^{-3}	4.46
$dP_F / d\mu_{12}$	-8.56×10^{-3}	-8.57×10^{-3}	0.14
$dP_F / d\mu_{13}$	-8.74×10^{-3}	-8.93×10^{-3}	2.19
$dP_F / d\mu_{14}$	-9.05×10^{-3}	-9.49×10^{-3}	4.67
$dP_F / d\mu_{15}$	-1.01×10^{-3}	-1.02×10^{-2}	0.81
$dP_F / d\mu_{16}$	-1.08×10^{-2}	-1.05×10^{-2}	2.85
$dP_F / d\mu_{17}$	-1.11×10^{-2}	-1.13×10^{-2}	1.80
$dP_F / d\mu_{18}$	-1.15×10^{-2}	-1.13×10^{-2}	2.14
$dP_F / d\mu_{19}$	-1.17×10^{-2}	-1.22×10^{-2}	4.64
$dP_F / d\mu_{20}$	-1.23×10^{-2}	-1.28×10^{-2}	3.87

3.3.4 Sensitivity Using Novel SORM for Higher-Order Performance Function

In this numerical example, the sensitivities of the probability of failures with respect to the three design points are obtained using the analytic derivation in Section 3.2 for the higher-order performance function. The higher-order performance function in X-space is given as

$$G(\mathbf{X}) = 15 + (Y-8)^2 + (Y-8)^3 + YZ \tag{3.40}$$

where $\begin{Bmatrix} Y \\ Z \end{Bmatrix} = \begin{bmatrix} 0.9063 & 0.4226 \\ 0.4226 & -0.9036 \end{bmatrix} \begin{Bmatrix} X_1 \\ X_2 \end{Bmatrix}$. The properties of the random variables at three design points are also shown in Table 3.7.

Table 3.7 Properties of Random Variables at Three Design Points

	X_1			X_2		
	Distribution Type	μ_1	σ_1	Distribution Type	μ_2	σ_2
Design Point 1	Normal	3	0.8	Normal	2	0.8
Design Point 2	Normal	4	0.8	Normal	5	0.8
Design Point 3	Normal	7	0.8	Normal	10	0.8

In Table 3.7, standard deviation for both random variables are intentionally set to be large to cause noticeable amount of error in this example. They are also all statistically independent to each other. As previously stated, the higher-order performance function given in Equation (3.40) is not quadratic, and quadratic approximations performed at three design points in U-space are shown in Figure 3.3.

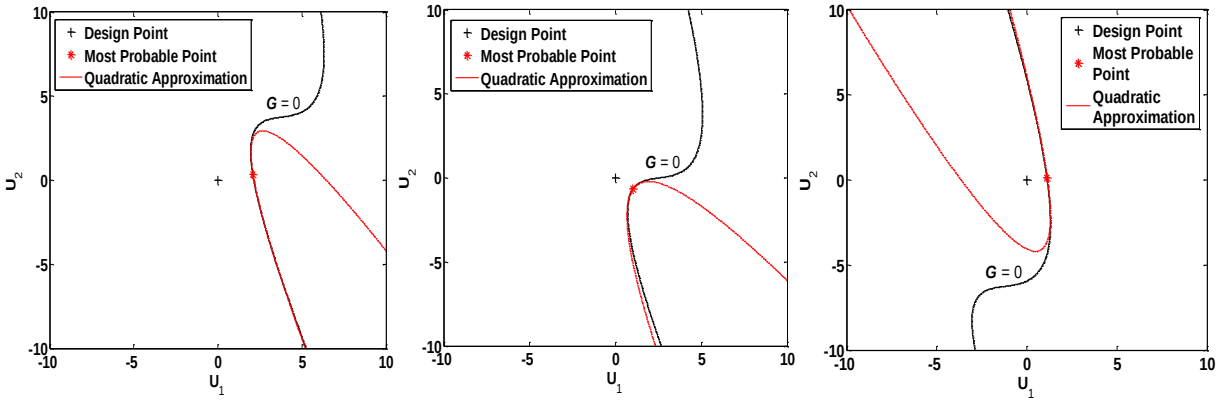

Figure 3.3 Quadratic Approximations in U-space at (a) Design Point 1, (b) Design Point 2, and (c) Design Point 3

Using the information in Table 3.7 and the analytic derivation in Section 3.2, the sensitivity is calculated at each design point, and it is then compared with the sensitivity obtained by FDM using MCS, which is shown in Table 3.7. As shown in Table 3.7, the errors are within range from 1 to 10%. Based on Figure 3.3, it can be seen that larger error in Table 3.8 occurs when small design change causes large change in the shape of the quadratic approximation. For example, if the design in Figure 3.3(a) moves along the y-direction by small amount, the quadratically approximated function will have very different curvature at the MPP. This violates the fundamental assumption in the proposed sensitivity analysis, that is, the Hessian

matrix remains constant when there is small design movement. However, even in the worst-case of the example, the maximum error is still less than 10% which may not affect the efficiency of RBDO.

Table 3.8 Comparison of Sensitivity Calculation at Three Design Points

		Proposed Sensitivity	FDM using MCS (10 M)	Error (%)
Design Point 1	$dP_F / d\mu_1$	5.05×10^{-2}	5.03×10^{-2}	1.40
	$dP_F / d\mu_2$	6.44×10^{-3}	7.11×10^{-3}	9.42
Design Point 2	$dP_F / d\mu_1$	1.32×10^{-1}	1.38×10^{-1}	4.66
	$dP_F / d\mu_2$	-1.06×10^{-1}	-9.96×10^{-2}	6.72
Design Point 3	$dP_F / d\mu_1$	2.65×10^{-1}	2.71×10^{-1}	2.50
	$dP_F / d\mu_2$	3.31×10^{-2}	3.40×10^{-2}	2.74

3.4 CONCLUSIONS

In the study in this chapter, sensitivities of probability of failure with respect to distribution parameters using the novel SORM have been derived through the proposed sensitivity analysis. During the derivation of the sensitivity, since it is inherent in SORM that the third-order derivative of a performance function is not available, it is assumed that sensitivities of eigenvalues with respect to distribution parameters are zero. With the assumption, the sensitivities of the probability of failure with respect to distribution parameters are derived. The calculation of the derived sensitivity includes calculation of the sensitivity of CDF of a linear combination of non-central chi-square variables with respect to each non-centrality parameter by FDM, which, however, does not require any iterative algorithm and repeating calculation of the parameters. Therefore, it is generally very efficient to calculate the sensitivity using the proposed method. The proposed sensitivity analysis is very accurate as well since CDF of a linear combination of non-central chi-square variables before and after perturbation are exactly calculated in the novel SORM. The calculation of the derived sensitivity also requires probability density function (PDF) of a linear combination of non-central chi-square variables, which is obtained by utilizing general chi-squared distribution. In numerical examples, the derived sensitivity is applied to calculate sensitivity in low-, medium-, and high-dimensional examples.

For the low-dimensional example that is perfectly quadratic, and the medium- and high-dimensional examples that are not quadratic, the obtained sensitivities based on the proposed sensitivity analysis are very close to those obtained by FDM using MCS. To further test the assumption that the Hessian matrix does not change due to the small change of the design variables, the last numerical example is carried out with higher-order performance function. The generated errors are not large and they are within acceptable ranges with the largest one below 10%. In conclusion, the proposed sensitivity analysis is efficient and accurate, and the error, which is generated due to the assumption, is within acceptable range even for higher-order performance function.

Chapter 4. Sampling-based Approach for Design Optimization in the Presence of Interval Variables

4.1 Introduction

The uncertainty is generally categorized into aleatory and epistemic uncertainties, where aleatory uncertainty is considered as irreducible whereas epistemic uncertainty is reducible by collecting more data. In case when sufficient amount of data for statistical information is unavailable, possibility-based (or fuzzy set) methods have utilized membership function to model insufficiently collected data (Du *et al.* 2006) and adjusted standard deviation and correlation coefficient involving confidence intervals have been utilized to offset an inaccurate modeling of data (Noh *et al.* 2011). When degree of insufficiency of data is even greater as only lower and upper bounds of data are available, the methods listed above are not applicable anymore, thus the different approach is required.

To deal with data of which only lower and upper bounds are available, a method of multi-point approximation that evaluates the weighting function and local approximations separately has been first developed for interval analysis (Penmetsa and Grandhi 2002). Then, the most probable point (MPP) based first-order reliability method (FORM) has been utilized for design optimization with mixture of random and interval variables (Du *et al.* 2005). As bounds of probability of failure or reliability exist in the presence of interval variables, design optimization for the worst and best cases has been also developed (Du *et al.* 2007), and sensitivity analysis considering bounds of interval variables and probability of failure has been developed accordingly (Duo and Du 2009).

As explained in Chapters 1-3, a design optimum is very efficiently searched by using the MPP-based FORM; however it is generally less accurate for highly nonlinear performance functions and high-dimensional input variables (Halder and Mahadevan 2000; Hasofer and Lind 1974; Tu and Choi 1999; Tu *et al.* 2001). To improve the accuracy on this occasion, the second order reliability method (SORM) can be applied after the MPP search; however, its efficiency is sacrificed due to the fact that computation of the

Hessian matrix is required by the SORM (Breitung 1984; Hohenbichler and Rackwitz 1988; Adhikari 2004; Zhang and Du 2010). The MPP-based dimension reduction method (DRM) can be also used for approximately assessing the reliability of a system, which is used as a probabilistic constraint in RBDO (Rahman and Wei 2006; Lee *et al.* 2008; Xiong *et al.* 2010).

In absence of accurate sensitivities of performance functions, the MPP-based reliability analysis or RBDO, which utilizes sensitivities of performance functions to find the MPP, cannot be directly used, instead the sampling-based reliability analysis or RBDO can be used (Lee *et al.* 2011; Lee *et al.* 2010; Gu *et al.* 2001). Assuming an accurate surrogate model is given (Youn *et al.* 2008; Wei et al. 2008; Chowdhury *et al.* 2009; Hu and Youn 2011), Monte Carlo simulation (MCS) (Rubinstein 1981) can be applied to find a design optimum with affordable computational burden.

The study in this chapter introduces interval analysis and design optimization utilizing the sampling-based method in the presence of only interval variables and in the presence of both random and interval variables. Due to the presence of interval variables, obtaining the worst combination of interval variables for both constraints and probabilistic constraints is involved (Du *et al.* 2005). When both random and interval variables are present, the worst combination of interval variables for probability of failure is directly searched using the probability of failure and its sensitivity since the design point where the worst-case probability of failure occurs does not always coincide with that for the worst-case performance function; it is highly likely as many studies have assumed, however not always. To evaluate sensitivities of probability of failure with respect to interval variables, the Dirac delta function is utilized to define behavior of the interval variables at the worst-case (Khuri 2004; Hoskins 1979; Kanwal 1998; Saichev and Woyczynski 1997).

Assuming an accurate surrogate model is given, one merit of the proposed method exists not only during the worst-case probability of failure search but also during reliability analysis after the worst-case probability of failure search. The worst-case probability of failure search, which will be explained in Section 4.2, utilizes a vector of interval variables instead of individual components of the vector, and it thus

promises efficiency when function evaluation of surrogate model is inexpensive. Also, it resolves the problem that the worst-case probability of failure does not always occur where the worst-case performance occurs. During the reliability analysis after the worst-case probability of failure search, another merit of the proposed method is that it does not make further approximations since it does not require gradients of the performance function and transformation of design variables from X-space to U-space, thus there is no approximation or restriction in calculating the sensitivities of constraints or probabilistic constraints (Lee *et al.* 2010).

4.2 Review of Sampling-Based RBDO

4.2.1 Formulation of RBDO

The mathematical formulation of RBDO is expressed as

$$\begin{aligned} &\text{minimize} && \text{cost}(\mathbf{d}) \\ &\text{subject to} && P\left[G_j\left(\mathbf{X}^{\mathbf{R}}\right) > 0 \right] \le P_{F_j}^{\text{tar}}, \quad j = 1,...,\text{NC} \\ & && \mathbf{d}^{\text{L}} \le \mathbf{d} \le \mathbf{d}^{\text{U}}, \quad \mathbf{d} \in \mathbf{R}^{\text{ndv}}, \text{ and } \mathbf{X} \in \text{R}^{NR} \end{aligned} \tag{4.1}$$

where $\mathbf{d} = \boldsymbol{\mu}(\mathbf{X})$ is the design vector, which is the mean value of the *NR*-dimensional random vector $\mathbf{X}^{\mathbf{R}} = \left\{ X_1^{\text{R}}, X_2^{\text{R}}, ... X_{NR}^{\text{R}} \right\}^{\text{T}}$; $P_{F_j}^{\text{tar}}$ is the target probability of failure for the j^{th} constraint; and NC, ndv, and *NR* are the number of probabilistic constraints, design variables, and random variables, respectively (Lee *et al.* 2010).

To carry out RBDO using Equation (4.1), the probabilistic constraints and their sensitivities are evaluated. Reviews on the reliability and its sensitivity analyses are explained in Sections 4.2.2 and 4.2.3, respectively.

4.2.2 Probability of Failure

The probability of failure with random variables, denoted by P_F, is defined using a multi-dimensional integral

$$P_F(\boldsymbol{\psi}) \equiv P\left[\mathbf{X}^{\mathbf{R}} \in \Omega_F\right] = \int_{\mathrm{R}^{NR}} I_{\Omega_F}\left(\mathbf{x}^{\mathbf{R}}\right) f_{\mathbf{X}^{\mathbf{R}}}\left(\mathbf{x}^{\mathbf{R}};\boldsymbol{\psi}\right) d\mathbf{x}^{\mathbf{R}} = E\left[I_{\Omega_F}\left(\mathbf{X}^{\mathbf{R}}\right)\right] \tag{4.2}$$

where $\boldsymbol{\psi}$ is a matrix of distribution parameters, which includes mean ($\boldsymbol{\mu}$) and/or standard deviation ($\boldsymbol{\sigma}$) of $\mathbf{X}^{\mathbf{R}}$; $P[\bullet]$ represents a probability measure; Ω_F is defined as a failure set; $f_{\mathbf{X}^{\mathbf{R}}}\left(\mathbf{x}^{\mathbf{R}};\boldsymbol{\psi}\right)$ is a joint probability density function (PDF) of $\mathbf{X}^{\mathbf{R}}$; and $E[\bullet]$ represents the expectation operator (Lee *et al.* 2010; McDonald and Mahadevan 2008). $I_{\Omega_F}\left(\mathbf{x}^{\mathbf{R}}\right)$ in Equation (4.2) is called an indicator function and defined as

$$I_{\Omega_F}\left(\mathbf{x}^{\mathbf{R}}\right) \equiv \begin{cases} 1, & \mathbf{x}^{\mathbf{R}} \in \Omega_F \\ 0, & \text{otherwise} \end{cases}. \tag{4.3}$$

4.2.3 Sensitivity of Probability of Failure

With the four regularity conditions satisfied, which are also explained in detail in the reference (Lee *et al.* 2010), taking the partial derivative of Equation (4.2) with respect to μ_i yields

$$\frac{\partial P_F\left(\boldsymbol{\mu}\right)}{\partial \mu_i} = \frac{\partial}{\partial \mu_i} \int_{\mathrm{R}^{NR}} I_{\Omega_F}\left(\mathbf{x}^{\mathbf{R}}\right) f_{\mathbf{X}^{\mathbf{R}}}\left(\mathbf{x}^{\mathbf{R}};\boldsymbol{\mu}\right) d\mathbf{x}^{\mathbf{R}} \tag{4.4}$$

and the differential and integral operators can be interchanged due to the 4th regularity condition in the reference (Lee *et al.* 2010) and the Lebesgue dominated convergence theorem (Rahman 2009; Rubinstein and Shapiro 1993) giving

$$\frac{\partial P_F\left(\boldsymbol{\mu}\right)}{\partial \mu_i} = E\left[I_{\Omega_F}\left(\mathbf{x}^{\mathbf{R}}\right) \frac{\partial \ln f_{\mathbf{X}^{\mathbf{R}}}\left(\mathbf{x}^{\mathbf{R}};\boldsymbol{\mu}\right)}{\partial \mu_i} \right] \tag{4.5}$$

The partial derivative of the log function of the joint PDF in Equation (4.5) with respect to μ_i is known as the first-order score function (Lee *et al.* 2010) for μ_i and is denoted as

$$s^{(1)}_{\mu_i}\left(\mathbf{x}^{\mathbf{R}};\boldsymbol{\mu}\right) \equiv \frac{\partial \ln f_{\mathbf{X}^{\mathbf{R}}}\left(\mathbf{x}^{\mathbf{R}};\boldsymbol{\mu}\right)}{\partial \mu_i} \tag{4.6}$$

To derive the sensitivity of the probability of failure in Equation (4.2), it is required to know the first-order score function in Equation (4.6), which is obtained using the following equation for independent random variables

$$s_{\mu_i}^{(1)}\left(\mathbf{x}^{\mathbf{R}};\boldsymbol{\mu}\right) \equiv \frac{\partial \ln f_{\mathbf{X}^{\mathbf{R}}}\left(\mathbf{x}^{\mathbf{R}};\boldsymbol{\mu}\right)}{\partial \mu_i} = \frac{\partial \ln f_{X_i^{\mathrm{R}}}\left(x_i^{\mathrm{R}};\mu_i\right)}{\partial \mu_i} \tag{4.7}$$

where $f_{X_i^{\mathrm{R}}}\left(x_i^{\mathrm{R}};\mu_i\right)$ is the marginal PDF corresponding to the i^{th} random variable X_i^{R}, and obtained using the following equation for correlated random variables

$$s_{\mu_i}^{(1)}\left(\mathbf{x}^{\mathbf{R}};\boldsymbol{\mu}\right) \equiv \frac{\partial \ln f_{\mathbf{X}^{\mathbf{R}}}\left(\mathbf{x}^{\mathbf{R}};\boldsymbol{\mu}\right)}{\partial \mu_i} = \frac{\partial \ln c\left(u,v;\theta\right)}{\partial \mu_i} + \frac{\partial \ln f_{X_i^{\mathrm{R}}}\left(x_i^{\mathrm{R}};\mu_i\right)}{\partial \mu_i} \tag{4.8}$$

where c is a copula density function, $u = F_{X_i^{\mathrm{R}}}\left(x_i^{\mathrm{R}};\mu_i\right)$ and $v = F_{X_j^{\mathrm{R}}}\left(x_j^{\mathrm{R}};\mu_j\right)$ are marginal CDFs for X_i^{R} and X_j^{R}, respectively, and θ is the correlation coefficient between X_i^{R} and X_j^{R} (Lee *et al.* 2010). The information of marginal PDFs, CDFs, and commonly used copula density functions is listed in detail in the reference (Lee *et al.* 2010).

4.2.4 Calculation of Probabilistic Constraints and Sensitivities

The MCS can be applied to calculate the probabilistic constraints in Equation (4.1) and their sensitivities. Denoting a surrogate model for the j^{th} constraint function with random variables as $\hat{G}_j\left(\mathbf{X}^{\mathbf{R}}\right)$, the probabilistic constraints in Equation (4.1) can be calculated as

$$P_{F_j} \equiv P\left[G_j\left(\mathbf{X}^{\mathbf{R}}\right) > 0\right] \cong \frac{1}{K}\sum_{k=1}^{K} I_{\hat{\Omega}_{F_j}}\left[\mathbf{x}^{\mathbf{R}(k)}\right] \le P_{F_j}^{\text{tar}} \tag{4.9}$$

where K is the MCS sample size, $\mathbf{x}^{\mathbf{R}(k)}$ is the k^{th} realization of $\mathbf{X}^{\mathbf{R}}$, and the failure set $\hat{\Omega}_{F_j}$ for the surrogate model is defined as $\hat{\Omega}_{F_j} \equiv \left[\mathbf{x}^{\mathbf{R}} : \hat{G}_j\left(\mathbf{x}^{\mathbf{R}}\right) > 0\right]$ (Lee *et al.* 2010). Sensitivities of the probabilistic constraints in Equation (4.1) are calculated using the score function as

$$\frac{\partial P_{F_j}}{\partial \mu_i} \cong \frac{1}{K}\sum_{k=1}^{K} I_{\hat{\Omega}_{F_j}}\left[\mathbf{x}^{\mathbf{R}(k)}\right] s_{\mu_i}^{(1)}\left[\mathbf{x}^{\mathbf{R}(k)};\boldsymbol{\mu}\right] \tag{4.10}$$

where $s_{\mu_i}^{(1)}\left[\mathbf{x}^{\mathbf{R}(k)};\boldsymbol{\mu}\right]$ is obtained using Equations (4.7) and (4.8) for independent and correlated random variables, respectively.

4.3 Design Optimization with Interval Variables

4.3.1 Formulation of Design Optimization with Interval Variables

The mathematical formulation of design optimization with interval variables only is expressed as

$$\begin{aligned} &\text{minimize} && \text{cost}(\mathbf{d}) \\ &\text{subject to} && G_j\left(\mathbf{X}_j^{\mathbf{I,worst}}\right) < 0, \quad j = 1,...,\text{NC} \\ & && \mathbf{d}^{\text{L}} \le \mathbf{d} \le \mathbf{d}^{\text{U}}, \ \ \mathbf{d} \in \text{R}^{\text{ndv}}, \ \text{and} \ \ \mathbf{X}^{\mathbf{I}} \in \text{R}^{NI} \end{aligned} \tag{4.11}$$

where $\mathbf{d} = \overline{\mathbf{X}^{\mathbf{I}}}$ is the design vector, which is the mid-point of the *NI*-dimensional interval vector $\mathbf{X}^{\mathbf{I}} = \left\{X_1^{\text{I}}, X_2^{\text{I}}, ..., X_{NI}^{\text{I}}\right\}^{\text{T}}$ where *NI* is the number of interval variables. $\mathbf{X}_j^{\mathbf{I,worst}}$ in Equation (4.11) is the worst-case interval variables for the j^{th} constraint, which is obtained by solving the optimization problem to

$$\begin{aligned} &\text{maximize} && G_j\left(\mathbf{X}^{\mathbf{I}}\right) \\ &\text{subject to} && \left|X_i^{\text{I}} - \overline{X_i^{\text{I}}}\right| \le \frac{\delta_i^{\text{I}}}{2} \ \ \textit{for} \ i = 1,...,NI \end{aligned} \tag{4.12}$$

where δ_i^{I} is the interval length of X_i^{I}. It should be noted that as any statistical information of an interval variable $\mathbf{X}^{\mathbf{I}}$ is not available, $\mathbf{X}^{\mathbf{I,worst}}$ must be considered for the design optimization.

To carry out the design optimization with interval variables using Equation (4.11), the proposed method first evaluates constraints with the worst-case interval variables, namely the worst-case constraints or the worst-case performance, and their sensitivities. Then, it utilizes "fmincon" using sequential quadratic programming (SQP) method from MATLAB Optimization Toolbox to further solve Equation (4.11), and there exist many alternative methods. Each of the worst-case constraint is obtained by the worst-case

performance search that solves Equation (4.12) and will be explained in Section 4.3.2, and sensitivity analysis of each of the worst-case constraint and its calculation are explained in Section 4.3.3. It is assumed that gradients of performance functions are not available; however it can be directly used if available.

4.3.2 Worst-Case Performance Search

The algorithm explained in this section searches the worst-case performance, and the algorithm was originally developed by Liu *et al*. in the reference (Du *et al*. 2006) for the maximal possibility search (MPS) for possibility-based design optimization. An important merit of the proposed algorithm is that it utilizes a vector of interval variables and a vector of sensitivities of a performance function with respect to all interval variables, thus its efficiency is not affected by the dimension of the interval variables. The algorithm for the worst-case performance search is summarized as following, which is also shown in the flowchart in Figure 4.1.

Step 1. Normalize interval variables X_i^{I} using

$$Z_i^{\mathrm{I}} = \frac{X_i^{\mathrm{I}} - \overline{X_i^{\mathrm{I}}}}{\delta_i^{\mathrm{I}}} \text{ or } X_i^{\mathrm{I}} = \overline{X_i^{\mathrm{I}}} + \delta_i^{\mathrm{I}} \cdot Z_i^{\mathrm{I}} \tag{4.13}$$

such that $\left|Z_i^{\mathrm{I}}\right| \le 0.5$.

Step 2. Set the iteration counter $k = 0$ with the convergence parameter $\varepsilon = 10^{-3}$. Set $j = 1$. Let $\mathbf{Z}^{\mathbf{I}(0)} = \mathbf{0}$. Calculate the performance $G\left(\mathbf{Z}^{\mathbf{I}(0)}\right)$ and the sensitivity $\nabla G\left(\mathbf{Z}^{\mathbf{I}(0)}\right)$. It is explained in Section 4.3.3 how to obtain $\nabla G\left(\mathbf{Z}^{\mathbf{I}(0)}\right)$. Let the direction vector be $\mathbf{d}^{(0)} = \nabla G\left(\mathbf{Z}^{\mathbf{I}(0)}\right)$.

Step 3. Search the next point as $\mathbf{Z}^{\mathbf{I}(k+1)} = 0.5 \cdot \mathrm{sgn}\left(\mathbf{d}^{(k)}\right)$ where 0.5 is obtained from *Step 1*. Let $k = k + 1$.

Step 4. Calculate the performance $G\left(\mathbf{Z}^{\mathbf{I}(k)}\right)$ and its sensitivity $\nabla G\left(\mathbf{Z}^{\mathbf{I}(k)}\right)$. Let a conjugate direction vector $\mathbf{d}^{(k)} = \nabla G\left(\mathbf{Z}^{\mathbf{I}(k)}\right) + \beta \mathbf{d}^{(k-1)}$ where $\beta = \left(\left\|\nabla G\left(\mathbf{Z}^{\mathbf{I}(k)}\right)\right\| / \left\|\nabla G\left(\mathbf{Z}^{\mathbf{I}(k-1)}\right)\right\|\right)^2$. If $\operatorname{sgn}\left(\nabla G\left(\mathbf{Z}^{\mathbf{I}(k)}\right)\right) = \operatorname{sgn}\left(\mathbf{Z}^{\mathbf{I}(k)}\right)$, it is the worst-case and go to *Step 11*.

Step 5. If $G\left(\mathbf{Z}^{\mathbf{I}(k)}\right) \geq G\left(\mathbf{Z}^{\mathbf{I}(j)}\right)$, let $j = k$ and go to *Step 3*. Otherwise, go to *Step 6* with $\mathbf{Z}^{\mathbf{I}(j)}$, $G\left(\mathbf{Z}^{\mathbf{I}(j)}\right)$ and $\nabla G\left(\mathbf{Z}^{\mathbf{I}(j)}\right)$.

If behavior of the performance function is not monotonic within an interval domain, in other words, if any component of the worst-case interval vector does not occur at the vertex of its interval domain, interpolation algorithm must be additionally applied to obtain more accurate worst-case performance (Du *et al.* 2006).

Step 6. Let $l = 0$ and a direction vector be $\mathbf{d}^{(l)} = \nabla G\left(\mathbf{Z}^{\mathbf{I}(j)}\right)$.

Step 7. Calculate the new point $\mathbf{Z}^{\mathbf{I}(k+1)}$ on the boundary of the domain from the start point $\mathbf{Z}^{\mathbf{I}(j)}$ along the search direction $\mathbf{d}^{(l)}$. Let $k = k + 1$.

Step 8. Calculate the performance $G\left(\mathbf{Z}^{\mathbf{I}(k)}\right)$ and its sensitivity $\nabla G\left(\mathbf{Z}^{\mathbf{I}(k)}\right)$. If

$$\begin{cases} \operatorname{sgn}\left(\partial G\left(\mathbf{Z}^{\mathbf{I}(k)}\right) / \partial\left(Z_i^{\mathrm{I}}\right)\right) = \operatorname{sgn}\left(Z_i^{\mathrm{I}}\right), & \text{for } \left|Z_i^{\mathrm{I}}\right| = 0.5 \\ \left|\partial G\left(\mathbf{Z}^{\mathbf{I}(k)}\right) / \partial\left(Z_i^{\mathrm{I}}\right)\right| < \varepsilon, & \text{for } \left|Z_i^{\mathrm{I}}\right| < 0.5 \end{cases}$$

then it is the worst-case and go to *Step 11*. Otherwise, go to *Step 9*.

Step 9. Use $G\left(\mathbf{Z}^{\mathbf{I}(j)}\right)$, $G\left(\mathbf{Z}^{\mathbf{I}(k)}\right)$, $\nabla G\left(\mathbf{Z}^{\mathbf{I}(j)}\right)$, and $\nabla G\left(\mathbf{Z}^{\mathbf{I}(k)}\right)$ to construct the third order polynomial $f(t)$ on the straight line between $\mathbf{Z}^{\mathbf{I}(j)}$ and $\mathbf{Z}^{\mathbf{I}(k)}$ where t is the parameter for the line. Calculate the maximum point t^* for this polynomial. Let $\mathbf{Z}^{\mathbf{I}(k+1)}$ be the point on the line corresponding to t^*. Let $k = k + 1$.

Step 10. Calculate the performance $G\left(\mathbf{Z}^{\mathbf{I}(k)}\right)$ and its sensitivity $\nabla G\left(\mathbf{Z}^{\mathbf{I}(k)}\right)$. Check the convergence criteria using the equation in *Step 8*. If converged, it is the worst-case and go to *Step 11*. Otherwise, let the new conjugate direction vector be $\mathbf{d}^{(l+1)} = \nabla G\left(\mathbf{Z}^{\mathbf{I}(k)}\right) + \beta \mathbf{d}^{(l)}$ where β is given by $\beta = \left(\left\|\nabla G\left(\mathbf{Z}^{\mathbf{I}(k)}\right)\right\| / \left\|\nabla G\left(\mathbf{Z}^{\mathbf{I}(k-2)}\right)\right\|\right)^2$. Let $j = k$, $l = l + 1$, and go to *Step 7*.

Step 11. De-normalize $\mathbf{Z}^{\mathrm{I,worst}}$ by Equation (4.13) in *Step 1* to obtain $\mathbf{X}^{\mathrm{I,worst}}$.

The proposed algorithm requires evaluation of sensitivities of a performance function with respect to interval variables. When gradients of the performance function are not available, sensitivities of each performance function with respect to interval variables can be calculated by the sampling-based method, and derivation of the sensitivities of the performance function with respect to interval variables and its calculation are explained in Section 4.3.3.

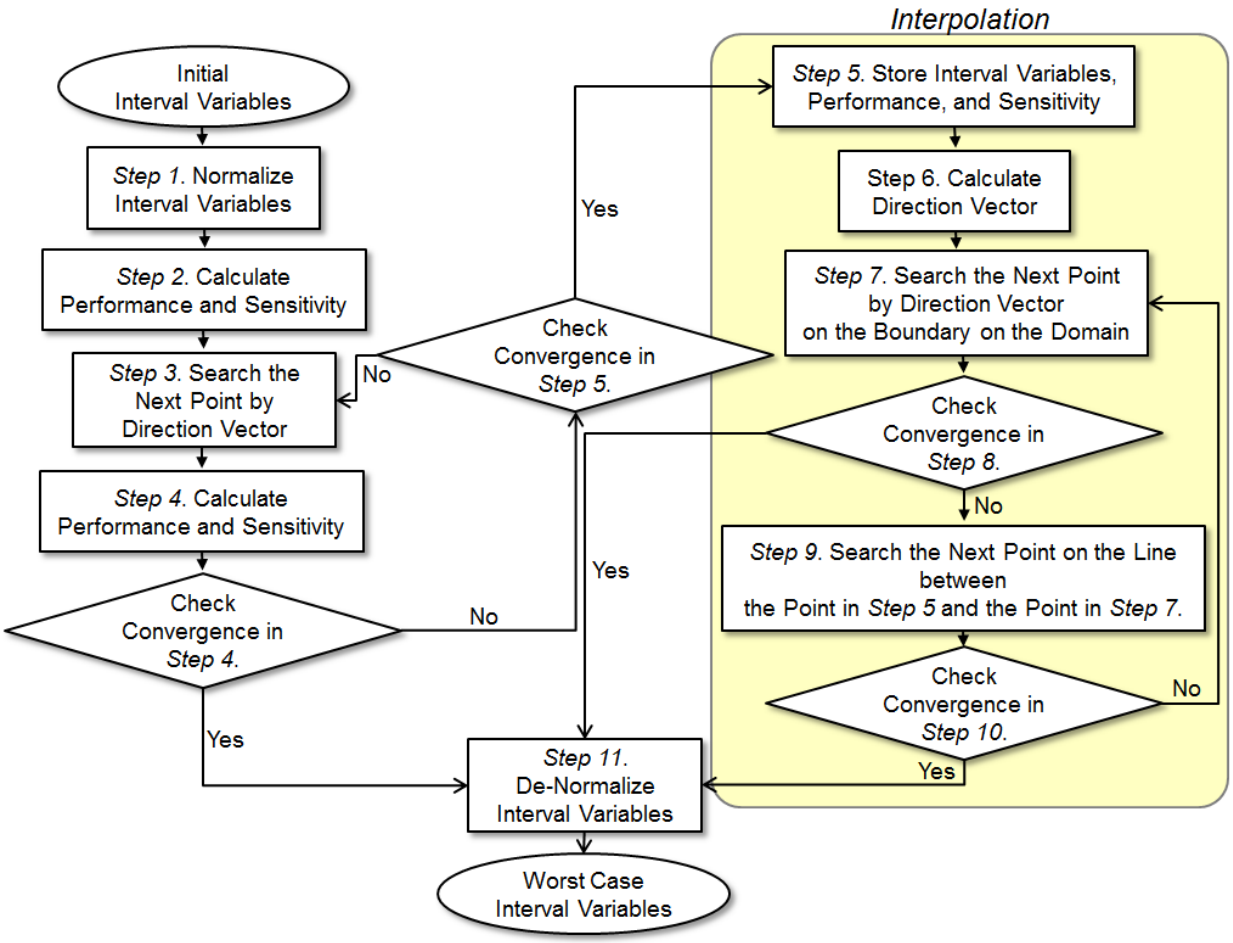

Figure 4.1 Flowchart for Worst-case Performance Search

4.3.3 Sensitivity Analysis on Worst-Case Performance Function

The behavior of any point within the interval of an interval variable x^{I} can be expressed using the Dirac delta function $\delta_{X^{\mathrm{I}}}(\bullet)$ (Browder 1996) as

$$\delta_{X^{\mathrm{I}}}\left(x^{\mathrm{I}}\right)=\begin{cases}+\infty, & x_i^{\mathrm{I}}=0\\ 0, & x_i^{\mathrm{I}}\neq 0\end{cases}, \tag{4.14}$$

and shifting Equation (4.14) by the worst-case of x_i^{I} denoted as $X_i^{\mathrm{I,worst}}$ yields

$$\delta_{X^{\mathrm{I}}}\left(x^{\mathrm{I}}-X^{\mathrm{I,worst}}\right)=\begin{cases}+\infty, & x^{\mathrm{I}}=X^{\mathrm{I,worst}}\\ 0, & x^{\mathrm{I}}\neq X^{\mathrm{I,worst}}\end{cases} \tag{4.15}$$

which is constrained to satisfy the identity

$$\int \delta_{X^{\mathrm{I}}}\left(x^{\mathrm{I}} - X^{\mathrm{I,worst}}\right)dx^{\mathrm{I}} = 1 \tag{4.16}$$

Also, the property of the Dirac delta function (Browder 1996) yields

$$\int G\left(x^{\mathrm{I}}\right)\delta_{X^{\mathrm{I}}}\left(x^{\mathrm{I}} - X^{\mathrm{I,worst}}\right)dx^{\mathrm{I}} = G\left(X^{\mathrm{I,worst}}\right) \tag{4.17}$$

Using Equations (4.14)~(4.17) and assuming $G(\bullet)$ is a continuously differentiable function of any real number, sensitivity of the worst-case performance function with respect to the i^{th} worst-case interval variable in general dimension becomes

$$\frac{\partial G\left(\mathbf{X}_j^{\mathbf{I,worst}}\right)}{\partial X_i^{\mathrm{I,worst}}} = \frac{\partial}{\partial X_i^{\mathrm{I,worst}}}\int_{\mathrm{R}^{NI}} G\left(\mathbf{x}^{\mathbf{I}}\right)\delta_{\mathbf{X}^{\mathbf{I}}}\left(\mathbf{x}^{\mathbf{I}} - \mathbf{X}^{\mathbf{I,worst}}\right)d\mathbf{x}^{\mathbf{I}} = \int_{\mathrm{R}^{NI}} G\left(\mathbf{x}^{\mathbf{I}}\right)\frac{\partial \delta_{\mathbf{X}^{\mathbf{I}}}\left(\mathbf{x}^{\mathbf{I}} - \mathbf{X}^{\mathbf{I,worst}}\right)}{\partial X_i^{\mathrm{I,worst}}}d\mathbf{x}^{\mathbf{I}} \tag{4.18}$$

where $\delta_{\mathbf{X}^{\mathbf{I}}}\left(\mathbf{x}^{\mathbf{I}} - \mathbf{X}^{\mathbf{I,worst}}\right) = \prod_{i=1}^{NI}\delta_{X^{\mathrm{I}}}\left(x_i^{\mathrm{I}} - X_i^{\mathrm{I,worst}}\right)$.

Based on the definition of the Dirac delta function, behavior of a single interval variable x^{I} at its worst-case $X^{\mathrm{I,worst}}$ can be treated as a Gaussian normal distribution with μ of $X^{\mathrm{I,worst}}$ and σ^2 approaching to 0, which implies

$$\delta_{X^{\mathrm{I}}}\left(x^{\mathrm{I}} - X^{\mathrm{I,worst}}\right) = \lim_{\sigma\to 0}\frac{1}{\sqrt{2\pi}\sigma}e^{-0.5\left[\left(x^{\mathrm{I}} - X^{\mathrm{I,worst}}\right)/\sigma\right]^2} = \lim_{\sigma\to 0} f_{X^{\mathrm{I}}}\left(x^{\mathrm{I}}\right). \tag{4.19}$$

Equation (4.19) is verified in this section first. Consider sensitivity of an one-dimensional performance function $G(\bullet)$ with respect to the worst-case of interval variable $X^{\mathrm{I,worst}}$, which by using Equation (4.18) becomes

$$\frac{\partial G\left(X^{\mathrm{I,worst}}\right)}{\partial X^{\mathrm{I,worst}}} = \int G\left(x^{\mathrm{I}}\right)\frac{\partial \delta_{X^{\mathrm{I}}}\left(x^{\mathrm{I}} - X^{\mathrm{I,worst}}\right)}{\partial\left(X^{\mathrm{I,worst}}\right)}dx^{\mathrm{I}} \tag{4.20}$$

$G\left(x^{\mathrm{I}}\right)$ in Equation (4.20) using the Taylor series expansion at $X^{\mathrm{I,worst}}$ can be expressed as

$$G\left(x^{\mathrm{I}}\right) = \sum_{m=0}^{\infty}\frac{G^{(m)}\left(X^{\mathrm{I,worst}}\right)}{m!}\left(x^{\mathrm{I}} - X^{\mathrm{I,worst}}\right)^m = \sum_{m=0}^{\infty} a_m\left(x^{\mathrm{I}} - X^{\mathrm{I,worst}}\right)^m \tag{4.21}$$

where $a_m = G^{(m)}\left(X^{\mathrm{I,worst}}\right)/m!$. Using Equations (4.19) and (4.21) and the score function explained in Section 4.2.3, the right hand side of Equation (4.20) is evaluated as

$$\int G\left(x^{\mathrm{I}}\right)\frac{\partial\delta_{X^{\mathrm{I}}}\left(x^{\mathrm{I}}-X^{\mathrm{I,worst}}\right)}{\partial X^{\mathrm{I,worst}}}dx^{\mathrm{I}} = \int\sum_{m=0}^{\infty}a_m\left(x^{\mathrm{I}}-X^{\mathrm{I,worst}}\right)^m\lim_{\sigma\to 0}\frac{\left(x^{\mathrm{I}}-X^{\mathrm{I,worst}}\right)}{\sigma^2}f_{X^{\mathrm{I}}}\left(x^{\mathrm{I}}\right)dx^{\mathrm{I}} \quad (4.22)$$

Using the expectation operator, the Equation (4.22) is further simplified as

$$\begin{aligned}\int G\left(x^{\mathrm{I}}\right)\frac{\partial\delta_{X^{\mathrm{I}}}\left(x^{\mathrm{I}}-X^{\mathrm{I,worst}}\right)}{\partial X^{\mathrm{I,worst}}}dx^{\mathrm{I}} &= E\left[\sum_{m=0}^{\infty}\lim_{\sigma\to 0}\frac{1}{\sigma^2}\left(a_m\left(x^{\mathrm{I}}-X^{\mathrm{I,worst}}\right)^{m+1}\right)\right]\\ &= E\left[\lim_{\sigma\to 0}\frac{1}{\sigma^2}a_1\left(x^{\mathrm{I}}-X^{\mathrm{I,worst}}\right)^2\right]\\ &= a_1\end{aligned} \quad (4.23)$$

where $E\left[\left(x^{\mathrm{I}}-X^{\mathrm{I,worst}}\right)^p\right]=0$ if p is odd and $E\left[\left(x^{\mathrm{I}}-X^{\mathrm{I,worst}}\right)^p\right]=\sigma^p\left(p-1\right)!!$ if p is even according to the property of central moments of a normal distribution. Using Equation (4.21), the left hand side of Equation (4.20) is evaluated as

$$\begin{aligned}\frac{\partial G\left(X^{\mathrm{I,worst}}\right)}{\partial X^{\mathrm{I,worst}}} &= \left.\frac{\partial G\left(X^{\mathrm{I}}\right)}{\partial X^{\mathrm{I}}}\right|_{X^{\mathrm{I}}=X^{\mathrm{I,worst}}} = \left.\frac{\partial\sum_{m=0}^{\infty}a_m\left(X^{\mathrm{I}}-X^{\mathrm{I,worst}}\right)^m}{\partial X^{\mathrm{I}}}\right|_{X^{\mathrm{I}}=X^{\mathrm{I,worst}}}\\ &= \sum_{m=1}^{\infty}a_m m\left(X^{\mathrm{I}}-X^{\mathrm{I,worst}}\right)^{m-1}\Big|_{X^{\mathrm{I}}=X^{\mathrm{I,worst}}} = a_1.\end{aligned} \quad (4.24)$$

The identical results in Equations (4.23) and (4.24) demonstrate the validity of treating behavior of x^{I} at $X^{\mathrm{I,worst}}$ as a Gaussian normal distribution with μ of $X^{\mathrm{I,worst}}$ and σ^2 approaching to 0.

Finally, using Equation (4.19), Equation (4.18) is further developed as

$$\frac{\partial G\left(\mathbf{X}^{\mathbf{I,worst}}\right)}{\partial X_i^{\mathrm{I,worst}}} = \int_{\mathrm{R}^{NI}} G\left(\mathbf{x}^{\mathbf{I}}\right)\frac{\partial\delta_{\mathbf{X}^{\mathbf{I}}}\left(\mathbf{x}^{\mathbf{I}}-\mathbf{X}^{\mathbf{I,worst}}\right)}{\partial X_i^{\mathrm{I,worst}}}d\mathbf{x}^{\mathbf{I}} = E\left[G\left(\mathbf{x}^{\mathbf{I}}\right)\lim_{\sigma\to 0}\frac{x_i^{\mathrm{I}}-X_i^{\mathrm{I,worst}}}{\sigma^2}\right] \quad (4.25)$$

and sensitivity of the worst-case constraint with respect to design point $\overline{X_i^{\mathrm{I}}}$ in Equation (4.11) becomes

$$\frac{\partial G\left(\mathbf{X}^{\mathbf{I,worst}}\right)}{\partial \overline{X_i^{\mathrm{I}}}} = \sum_{l=1}^{NI} \frac{\partial G\left(\mathbf{X}^{\mathbf{I,worst}}\right)}{\partial X_l^{\mathrm{I,worst}}} \frac{\partial X_l^{\mathrm{I,worst}}}{\partial \overline{X_i^{\mathrm{I}}}} = \sum_{l=1}^{NI} E\left[G\left(\mathbf{x}^{\mathbf{I}}\right) \lim_{\sigma \to 0} \frac{x_l^{\mathrm{I}} - X_l^{\mathrm{I,worst}}}{\sigma^2} \right] \frac{\partial X_l^{\mathrm{I,worst}}}{\partial \overline{X_i^{\mathrm{I}}}} \tag{4.26}$$

where

$$\begin{cases} \partial X_l^{\mathrm{I,worst}} / \partial \overline{X_i^{\mathrm{I}}} = 1, & if \left| X_l^{\mathrm{I,worst}} - \overline{X_i^{\mathrm{I}}} \right| = \delta_l^{\mathrm{I}} / 2 \\ \partial X_l^{\mathrm{I,worst}} / \partial \overline{X_i^{\mathrm{I}}} = 0, & if \left| X_l^{\mathrm{I,worst}} - \overline{X_i^{\mathrm{I}}} \right| < \delta_l^{\mathrm{I}} / 2 \end{cases} \tag{4.27}$$

Additionally, it is noted that the Dirac delta function can be also applicable to define behavior of deterministic variables when sensitivities of performance functions with respect to deterministic variables are not available. Thus, in the presence of deterministic variables, the proposed sampling-based method can be applied to evaluate sensitivities of performance functions even when gradients of the performance functions are not obtainable.

The proposed method assumes surrogate models or actual functions are given, and a surrogate model for the constraint function with interval variables is denoted as $\hat{G}\left(\mathbf{X}^{\mathbf{I}}\right)$. Then, the MCS can be applied to calculate sensitivity of a performance function with respect to the i^{th} worst-case interval variable during the worst-case performance search in Section 4.3.2 using Equation (4.25) as

$$\frac{\partial G\left(\mathbf{X}^{\mathbf{I,worst}}\right)}{\partial X_l^{\mathrm{I,worst}}} \cong \frac{\partial \hat{G}\left(\mathbf{X}^{\mathbf{I,worst}}\right)}{\partial X_l^{\mathrm{I,worst}}} \cong \frac{1}{K} \sum_{k=1}^{K} \hat{G}\left(\mathbf{x}^{\mathbf{I,worst}(k)}\right) \frac{x_l^{\mathrm{I}(k)} - X_l^{\mathrm{I,worst}}}{\sigma^2_{X_l^{\mathrm{I,worst}}}} \tag{4.28}$$

where $\sigma_{X_l^{\mathrm{I,worst}}}$ is $\sigma_{X^{\mathrm{I}}}$ for $X_l^{\mathrm{I,worst}}$ coming from σ in Equation (4.26), and sensitivities of the worst-case constraints in Equation (4.11) can be calculated using Equations (4.26) and (4.27) as

$$\frac{\partial G_j\left(\mathbf{X}_{\boldsymbol{j}}^{\mathbf{I,worst}}\right)}{\partial \overline{X_i^{\mathrm{I}}}} \cong \frac{\partial \hat{G}_j\left(\mathbf{X}_{\boldsymbol{j}}^{\mathbf{I,worst}}\right)}{\partial \overline{X_i^{\mathrm{I}}}} \cong \frac{1}{K} \sum_{l=1}^{NI} \sum_{k=1}^{K} \hat{G}_j\left(\mathbf{x}_{\boldsymbol{j}}^{\mathbf{I,worst}(k)}\right) \frac{x_{j,l}^{\mathrm{I}(k)} - X_{j,l}^{\mathrm{I,worst}}}{\sigma^2_{X_{j,l}^{\mathrm{I,worst}}}} \frac{\partial X_{j,l}^{\mathrm{I,worst}}}{\partial \overline{X_{j,i}^{\mathrm{I}}}} \tag{4.29}$$

The desired value of $\sigma_{X^{\mathrm{I}}}$ used in Equations (4.28) and (4.29) for the sampling-based method is determined through the following simulation analysis. During the simulation analysis, ratio of $\sigma_{X^{\mathrm{I}}}$ to $\overline{X^{\mathrm{I}}}$

or $\frac{\sigma_{X^I}}{\overline{X^I}}$ instead of just σ_{X^I} is considered since σ_{X^I} depends on $\overline{X^I}$, and sensitivity of a performance function $G_1\left(X^I\right)=2X^I$ with respect to X^I is calculated by the MCS while $\frac{\sigma_{X^I}}{\overline{X^I}}$ changes from 0.1 to 0.001 in descending order. The result is then compared to the true sensitivity, which is analytically obtained as 2. From the result shown in Figure 4.2, it is demonstrated that $0.008 \le \frac{\sigma_{X^I}}{\overline{X^I}} \le 0.02$ for the desired value of σ_{X^I}. From the negligible amount of error less than 0.3% in Figure 4.2, validity of calculating sensitivities of a performance function with respect to interval variables using the sampling-based method with a very small standard deviation can be also shown.

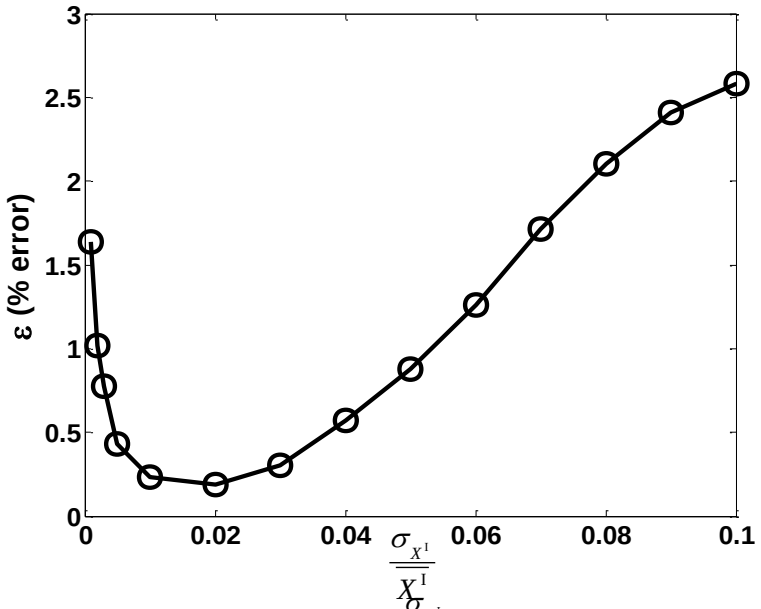

Figure 4.2 Error of Sensitivity as $\frac{\sigma_{X^I}}{\overline{X^I}}$ changes from 0.001 to 0.1

4.4 Design Optimization with Random and Interval Variables

4.4.1 Formulation of Design Optimization with Mixture of Random and Interval Variables

The mathematical formulation of design optimization with mixture of random and interval variables is expressed as

$$\begin{aligned} &\text{minimize} && \text{cost}(\mathbf{d}) \\ &\text{subject to} && P_{F_j}^{\text{worst}} \equiv P\left[G_j\left(\mathbf{X}^{\mathbf{R}}, \mathbf{X}_{\boldsymbol{j}}^{\mathbf{I,worst}}\right) > 0 \right] \le P_{F_j}^{\text{tar}}, \quad j = 1,..., \text{NC} \\ &&& \mathbf{d}^{\text{L}} \le \mathbf{d} \le \mathbf{d}^{\text{U}}, \ \ \mathbf{d} \in \text{R}^{\text{ndv}}, \ \ \mathbf{X}^{\mathbf{R}} \in \text{R}^{NR}, \text{ and } \ \mathbf{X}^{\mathbf{I}} \in \text{R}^{NI} \end{aligned} \tag{4.30}$$

where $\mathbf{d} = \left\{ \mu_1,..., \mu_{NR}, \overline{X^{\text{I}}_{NR+1}},..., \overline{X^{\text{I}}_{NR+NI}} \right\}$ is the design vector; $\mathbf{X}_{\boldsymbol{j}}^{\mathbf{I,worst}}$ in Equation (4.30) is the worst-case interval variables for the j^{th} probabilistic constraint, which is obtained by solving the optimization problem to

$$\begin{aligned} &\text{maximize} && P\left[G_j\left(\mathbf{X}^{\mathbf{I}}\right) > 0 \right] \\ &\text{subject to} && \left| X_i^{\text{I}} - \overline{X_i^{\text{I}}} \right| \le \frac{\delta_i^{\text{I}}}{2} \ \ \textit{for } i = 1,..., NI. \end{aligned} \tag{4.31}$$

To carry out the design optimization with interval variables using Equation (4.30), the proposed method evaluates probabilistic constraints with the worst-case interval variables, namely the worst-case probabilistic constraints or the worst-case probability of failure, and their sensitivities. Each of the worst-case probabilistic constraint is obtained by the worst-case probability of failure search that solves Equation (4.31) and will be explained in Section 4.4.2, and sensitivity analysis of each of the worst-case probabilistic constraint and its calculation are explained in Section 4.4.3. It should be noted that the worst-case probability of failure does not always occur at the point where the worst-case performance occurs, which is demonstrated with an example in Section 4.4.2. Thus, by applying an algorithm for the worst-case performance search in Section 4.3.2 by directly utilizing probability of failure and its sensitivity in replacement of performance value and its sensitivity, the problem pointed out in the previous sentence can be resolved.

4.4.2 Worst-Case Probability of Failure

The worst-case probability of failure with random and interval variables, denoted by P_F^{worst}, is defined using Equation (4.30) and a multi-dimensional integral as

$$P_F^{\text{worst}} \equiv \int_{\mathrm{R}^{NR+NI}} I_{\Omega_F}\left(\mathrm{x}^{\mathrm{R}}, \mathbf{x}^{\mathbf{I}}\right) f_{\mathbf{X}}\left(\mathrm{x}^{\mathrm{R}}\right) \delta_{\mathbf{X}^{\mathbf{I}}}\left(\mathbf{x}^{\mathbf{I}} - \mathbf{X}^{\mathbf{I,worst}}\right) d\mathbf{x}^{\mathbf{R}} d\mathbf{x}^{\mathbf{I}} = E\left[I_{\Omega_F}\left(\mathbf{X}^{\mathbf{R}}, \mathbf{X}^{\mathbf{I,worst}}\right)\right] \quad (4.32)$$

The worst-case probability of failure in Equation (4.32) is obtained using the algorithm for the worst-case performance search explained in Section 4.3.2 by utilizing probability of failure and its sensitivity in replacement of the performance function and its sensitivity. Derivation of the sensitivity of the probability of failure with respect to the worst-case interval variables and its calculation are explained in Section 4.4.3. Usually, the worst-case probability of failure occurs at the worst-case performance, so conventionally the worst-case probability of failure is calculated by evaluating the probability of failure at the worst-case performance (Du *et al.* 2005; Du 2007; Guo and Du 2009). However, this is not always the case and the following example demonstrates it.

Consider a 2D highly nonlinear polynomial function,

$$G_2(\mathbf{X}) = 0.7361 + (\mathrm{W}-6)^2 + (\mathrm{W}-6)^3 - 0.6 \times (\mathrm{W}-6)^4 + \mathrm{Z} \quad (4.33)$$

where $\begin{Bmatrix} \mathrm{W} \\ \mathrm{Z} \end{Bmatrix} = \begin{bmatrix} 0.8660 & 0.5000 \\ 0.5000 & -0.8660 \end{bmatrix} \begin{Bmatrix} X_1^{\mathrm{I}} \\ X_2^{\mathrm{R}} \end{Bmatrix}$. As shown in Table 4.1, X_1^{I} and X_2^{R} are interval and random variables, respectively. The mid-point and interval length of X_1^{I} are 6.5 and 3, respectively. The mean and standard deviation of X_2^{R} are 2.5 and 1, respectively. Then, X_1^{I} is divided into 100 sub-intervals, for each of which, the performance functions and probability of failures are evaluated. For the evaluation of the probability of failure, 5×10^7 MCS sample are used for each sub-interval.

Table 4.1 Property of Input Variables

Variables	Types	Distribution	Parameters	
X_1^{I}	Interval	N/A	$\overline{X_1^{\mathrm{I}}} = 6.5$	$\delta_1^{\mathrm{I}} = 3$
X_2^{R}	Random	Normal	$\mu_2 = 2.5$	$\sigma_2 = 1$

As shown in Figure 4.3, the worst-case probability of failure does not occur where the worst-case performance occurs. The worst-case probability of failure occurs at $X_1^{\mathrm{I}} = \overline{X_1^{\mathrm{I}}} + \delta_1^{\mathrm{I}} / 2 = 8$ where performance and probability of failure are −4.1437 and 0.2418, respectively, while the worst-case performance occurs at $X_1^{\mathrm{I}} = \overline{X_1^{\mathrm{I}}} - \dfrac{\delta_1^{\mathrm{I}}}{2} = 5$, where the performance and probability of failure are −1.1547 and 0.1222, respectively. Thus, the study in this chapter suggests using the algorithm for the worst-case probability failure search directly instead of obtaining the worst-case probability of failure by calculating the probability of failure where the worst-case performance occurs.

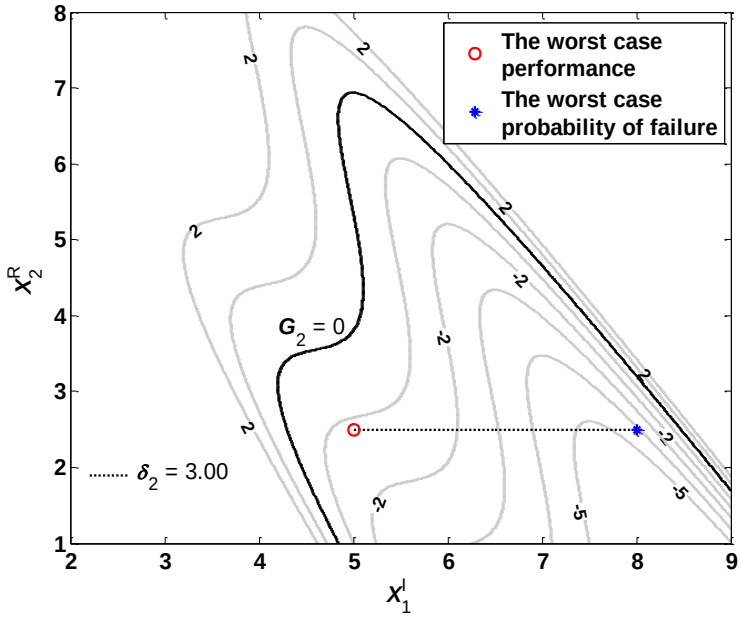

Figure 4.3 Worst-case Performance and Worst-case Probability of Failure

The MCS can be applied to calculate probability of failure during the worst-case probability of failure search. Denoting the surrogate model for constraint functions with random and interval variables as $\hat{G}\left(\mathbf{X}^{\mathbf{R}}, \mathbf{X}^{\mathbf{I}}\right)$, the probability of failure during the worst-case probability of failure search can be calculated using Equation (4.32) as

$$P_F^{\text{worst}} \equiv P\left[G\left(\mathbf{X}^{\mathbf{R}}, \mathbf{X}^{\mathbf{I,worst}}\right) > 0\right] \cong \frac{1}{K}\sum_{k=1}^{K} I_{\hat{\Omega}_F}\left[\mathbf{x}^{\mathbf{R}(k)}, \mathbf{X}^{\mathbf{I,worst}}\right] \le P_F^{\text{tar}} \tag{4.34}$$

where the failure set $\hat{\Omega}_F$ for the surrogate model is defined as $\hat{\Omega}_F \equiv \left[\mathbf{x} : \hat{G}\left(\mathbf{x}^{\mathbf{R}}, \mathbf{X}^{\mathbf{I,worst}}\right) > 0\right]$.

4.4.3 Sensitivity Analysis on Worst-Case Probability of Failure

Taking partial derivative of Equation (4.32) with respect to the i^{th} worst-case interval variable yields

$$\frac{\partial P_F^{\text{worst}}}{\partial X_i^{\text{I,worst}}} = \sum_{i=1}^{NI} E\left[I_{\Omega_F}\left(\mathbf{x}^{\mathbf{R}}, \mathbf{X}^{\mathbf{I,worst}}\right) \frac{x_i^{\text{I}} - X_i^{\text{I}}}{\sigma^2_{X_i^{\text{I,worst}}}} \right] \tag{4.35}$$

Then, taking partial derivative of Equation (4.32) with respect to the mid-point of the i^{th} interval variable using Equation (4.35) yields

$$\frac{\partial P_F^{\text{worst}}}{\partial \overline{X_i^{\text{I}}}} = \sum_{l=1}^{NI} \frac{\partial P_F^{\text{worst}}}{\partial X_l^{\text{I,worst}}} \frac{\partial X_l^{\text{I,worst}}}{\partial \overline{X_i^{\text{I}}}} = \sum_{l=1}^{NI} E\left[I_{\Omega_F}\left(\mathbf{x}^{\mathbf{R}}, \mathbf{X}^{\mathbf{I,worst}}\right) \frac{x_l^{\text{I}} - X_l^{\text{I}}}{\sigma^2_{X_l^{\text{I,worst}}}} \right] \frac{\partial X_l^{\text{I,worst}}}{\partial \overline{X_i^{\text{I}}}}, \tag{4.36}$$

where $\dfrac{\partial X_l^{\text{I,worst}}}{\partial \overline{X_i^{\text{I}}}}$ is obtained from Equation (4.27). Taking partial derivative of Equation (4.32) with respect to the mean of the i^{th} random variable yields

$$\frac{\partial P_F^{\text{worst}}}{\partial \mu_i} = \int_{\mathrm{R}^{NR+NI}} I_{\Omega_F}\left(\mathrm{x}^{\mathrm{R}}, \mathbf{x}^{\mathbf{I}}\right) \frac{\partial \ln f_{\mathrm{X}}\left(\mathrm{x}^{\mathrm{R}}; \boldsymbol{\mu}\right)}{\partial \mu_i} f_{\mathrm{X}}\left(\mathrm{x}^{\mathrm{R}}; \boldsymbol{\mu}\right) \delta_{\mathbf{X}^{\mathbf{I}}}\left(\mathbf{x}^{\mathbf{I}} - \mathbf{X}^{\mathbf{I,worst}}\right) d\mathbf{x}^{\mathbf{R}} d\mathbf{x}^{\mathbf{I}}. \tag{4.37}$$

Using Equation (4.17), Equation (4.37) is further simplified as

$$\begin{aligned} \frac{\partial P_F^{\text{worst}}}{\partial \mu_i} &= \int_{\mathrm{R}^{NR+NI}} I_{\Omega_F}\left(\mathbf{x}^{\mathbf{R}}, \mathbf{X}^{\mathbf{I,worst}}\right) \frac{\partial \ln f_{\mathrm{X}}\left(\mathbf{x}^{\mathbf{R}}; \boldsymbol{\mu}\right)}{\partial \mu_i} f_{\mathrm{X}}\left(\mathbf{x}^{\mathbf{R}}; \boldsymbol{\mu}\right) d\mathbf{x}^{\mathbf{R}} \\ &= E\left[I_{\Omega_F}\left(\mathbf{x}^{\mathbf{R}}, \mathbf{X}^{\mathbf{I,worst}}\right) \frac{\partial \ln f_{\mathrm{X}}\left(\mathbf{x}^{\mathbf{R}}; \boldsymbol{\mu}\right)}{\partial \mu_i} \right]. \end{aligned} \tag{4.38}$$

The MCS can be applied to calculate sensitivity of the probability of failure with respect to the i^{th} worst-case interval variable during the worst-case probability of failure search in Section 4.4.2 based on Equation (4.35) as

$$\frac{\partial P_F^{\text{worst}}}{\partial X_i^{\text{I,worst}}} = \frac{1}{K} \sum_{i=1}^{K} I_{\hat{\Omega}_F}\left[\mathbf{x}^{\mathbf{R}(k)}, \mathbf{X}^{\mathbf{I,worst}}\right] \frac{x_i^{\text{I}(k)} - X_i^{\text{I,worst}}}{\sigma^2_{X_i^{\text{I,worst}}}} \tag{4.39}$$

Sensitivities of the worst-case probabilistic constraints in Equation (4.30) with respect to the i^{th} interval variable at the mid-point as

$$\frac{\partial P_{F_j}^{\text{worst}}}{\partial \overline{X_i^{\text{I}}}} \cong \frac{1}{K}\sum_{l=1}^{NI}\sum_{k=1}^{K} I_{\hat{\Omega}_{F_j}}\left[\mathbf{x}^{\mathbf{R}(k)}, \mathbf{X}_{\boldsymbol{j}}^{\mathbf{I,worst}}\right]\frac{x_{j,l}^{\text{I}(k)} - X_{j,l}^{\text{I,worst}}}{\sigma^2_{X_{j,l}^{\text{I,worst}}}}\frac{\partial X_{j,l}^{\text{I,worst}}}{\partial \overline{X_{j,i}^{\text{I}}}} \tag{4.40}$$

based on Equation (4.36). Sensitivities of the worst-case probabilistic constraints in Equation (4.30) with respect to the i^{th} random variable at the mean point are calculated as

$$\frac{\partial P_{F_j}^{\text{worst}}}{\partial \mu_i} \cong \frac{1}{K}\sum_{k=1}^{K} I_{\hat{\Omega}_{F_j}}\left[\mathbf{x}^{\mathbf{R}(k)}, \mathbf{X}_{\boldsymbol{j}}^{\mathbf{I,worst}}\right] s_{\mu_i}^{(1)}\left[\mathbf{x}^{\mathbf{R}(k)}; \boldsymbol{\mu}\right] \tag{4.41}$$

based on Equation (4.38).

4.5 Numerical Examples

Numerical studies are carried out in this section to verify the algorithm that searches the worst-case probability of failure in Section 4 for both low-dimensional and high-dimensional cases. Also, design optimization with mixture of interval and random variables that utilizes the worst-case probability of failure search is carried out.

4.5.1 Worst-Case Probability of Failure Search for Two-Dimensional Example

In this numerical example, the algorithm that searches the worst-case probability of failure is applied to a two-dimensional case, and one of input variables is an interval and the other is a random. Consider a nonlinear performance function given as

$$G_1(\mathbf{X}) = -0.3X_1^{\text{I}}\left(X_2^{\text{R}}\right)^2 + X_1^{\text{I}} - 0.8X_2^{\text{R}} - 2.8 \tag{4.42}$$

As shown in Table 4.2, X_1^{I} is an interval variable with its mid-point at −0.5 and its interval length of 1, and X_2^{R} is a normally distributed random variable with its mean at 2.2 and its standard deviation of 1.

Table 4.2 Property of Input Variables

Variables	Types	Distribution	Parameters	
X_1^{I}	Interval	N/A	$\overline{X_1^{\mathrm{I}}} = -0.5$	$\delta_1^{\mathrm{I}} = 1$
X_2^{R}	Random	Normal	$\mu_2 = 2.2$	$\sigma_2 = 1$

With the given property of these input variables and the performance function in Equation (4.42), the worst-case probability of failure is obtained using the worst-case probability of failure search explained in Section 4.2. The results are shown both in Table 4.3 and Figure 4.4. The worst-case interval variables at the 4th iteration in Table 4.3 is obtained by an interpolation of two worst-case interval variables candidates at the 2nd and the 3rd iteration during *Step 9* of the worst-case probability of failure search. The obtained result is compared with the result obtained by dividing the interval domain into 100 sub-intervals and performing the MCS with 5×10^7 samples for all sub-intervals, which is shown in Table 4.4.

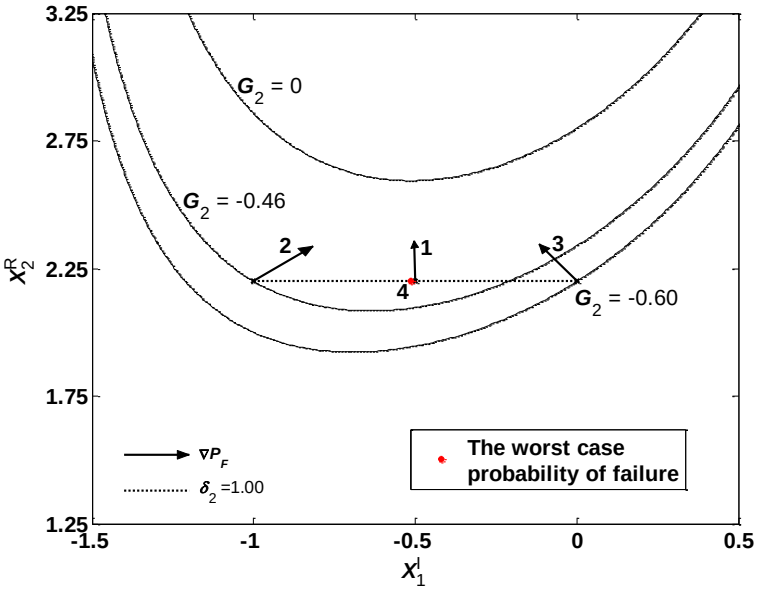

Figure 4.4 Search History of Worst-case Probability of Failure

Table 4.3 Search History of Worst-case Probability of Failure

Iteration	X_1^{I}	P_{F_1}	$\partial P_{F_1} / \partial X_1^{\mathrm{I}}$
1	-0.5	0.3457	-0.00789
2	-1	0.2541	0.42073
3	0	0.2737	-0.26648
4	-0.5146	0.3460	0.00082

In terms of efficiency, the proposed algorithm requires (4iterations) × (1MCS/iteration) = 4MCSs, and performing the MCS for all 100 sub-divided intervals requires (100sub-intervals) × (1MCS/sub-interval) = 100MCSs. Thus, the proposed algorithm is 25 times more efficient than the crude MCS while maintaining accuracy in this example.

Table 4.4 Comparison of Results Obtained by 2 Different Methods

Methods	X_1^{I}	$P_{F_1}^{\mathrm{worst}}$	Number of MCS
Proposed algorithm	-0.5136	0.3460	4
Performing MCS for all 100 sub-intervals	-0.5152	0.3465	100

4.5.2 Worst-Case Probability of Failure Search for High-Dimensional Engineering Example

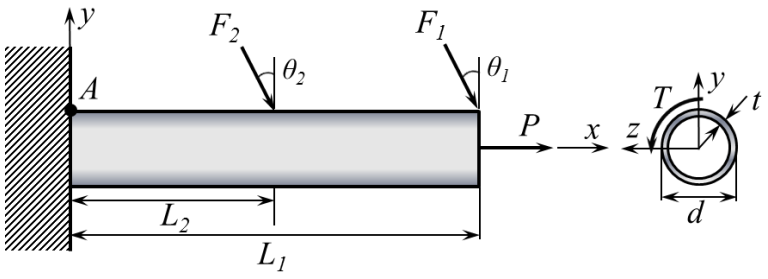

Figure 4.5 Schematic Diagram of Cantilever Tube

In this numerical example, the algorithm that searches the worst-case probability of failure is applied to a high-dimensional case where 2 of input variables are interval and 9 of them are random variables. Consider the cantilever tube shown in Fig. 5 subjected to external forces F_1, F_2, and P, and torsion T (Du

2007). The performance function is defined as the difference between the yield strength S_y and the maximum stress, namely,

$$G_2 = g(\mathbf{X}) = \sigma_{\max} - S_y \tag{4.43}$$

where $\sigma_{\max}$ is the maximum von Mises stress on the top surface of the tube at the origin, which is given by

$$\sigma_{\max} = \sqrt{\sigma_x^2 + 3\tau_{zx}^2} \tag{4.44}$$

where the normal stress σ_x is obtained as

$$\sigma_x = \frac{P + F_1 \sin\theta_1 + F_2 \sin\theta_2}{\frac{\pi}{4}\left[d^2 - (d-2t)^2\right]} + \frac{(F_1 L_1 \cos\theta_1 + F_2 L_2 \cos\theta_2)d}{2 \times \frac{\pi}{64}\left[d^4 - (d-2t)^4\right]} \tag{4.45}$$

and the shear stress τ_{xz} is obtained as

$$\tau_{xz} = \frac{Td}{4 \times \frac{\pi}{64}\left[d^4 - (d-2t)^4\right]}, \tag{4.46}$$

respectively. The property of random and interval variables are given in Tables 4.5 and 4.6, respectively. As shown in Tables 4.5 and 4.6, nine random variables X_1^{R} ~ X_9^{R} having various distributions and two interval variables X_{10}^{I} and X_{11}^{I} having the identical interval length at different mid-points are used as input variables.

Table 4.5 Property of Random Variables

Variables	Parameter 1	Parameter 2	Distribution
$X_1^{\mathrm{R}}(t)$	5 mm (mean)	0.1 mm (std*)	Normal
$X_2^{\mathrm{R}}(d)$	42 mm (mean)	42 mm (mean)	Normal
$X_3^{\mathrm{R}}(L_1)$	119.75 mm (lb**)	120.25 mm (ub***)	Uniform
$X_4^{\mathrm{R}}(L_2)$	59.75 mm (lb)	60.25 mm (ub)	Uniform
$X_5^{\mathrm{R}}(F_1)$	3.0 kN (mean)	0.3 kN (std)	Normal
$X_6^{\mathrm{R}}(F_2)$	3.0 kN (mean)	0.3 kN (std)	Normal
$X_7^{\mathrm{R}}(P)$	12.0 kN (mean)	1.2 kN (std)	Gumbel
$X_8^{\mathrm{R}}(T)$	90.0 Nm (mean)	9.0 Nm (std)	Normal
$X_9^{\mathrm{R}}(S_y)$	133.7 Mpa (mean)	22.0 Mpa (std)	Normal

***:** std-standard deviation
****:** lb – lower bound of a uniform distribution
*****:** ub – upper bound of a uniform distribution

Table 4.6 Property of Interval Variables

Variables	Parameters
$X_{10}^{\mathrm{I}}(\theta_1)$	$\overline{X}_{10}^{\mathrm{I}} = 5°,\ \delta_{10}^{\mathrm{I}} = 10°$
$X_{11}^{\mathrm{I}}(\theta_2)$	$\overline{X}_{11}^{\mathrm{I}} = 10°,\ \delta_{11}^{\mathrm{I}} = 10°$

With the property of input variables and the performance function in Equation (4.43), the worst-case probability of failure is obtained using the worst-case probability of failure search. The MCS with 5×10^7 samples is tried for every iteration, and the tolerance of 10^{-4} instead of 10^{-3} is set for this example since the sensitivity of probability of failure with respect to both interval variables is less than 10^{-2} throughout the interval domain. By using the proposed algorithm, the worst-case probability of failure is obtained in 8 iterations including the one with the interpolation and the discard one. In Table 4.7, since the probability of failure at the 4th iteration is smaller than that at the 3rd iteration, it is discarded during the *Step 5* of the worst-case probability of failure search in Section 4.2. Search history is shown in both Table 4.7 and Figure 4.6. The worst-case probability of failure is obtained as 0.50849 and the worst-case interval variables are obtained as [3.993, 7.887]. The obtained result is then compared with the result obtained by dividing both

interval domains into 100 sub-intervals and performing MCS with samples for all combinations of sub-intervals.

The result of the comparison is shown in Table 8. In terms of efficiency, the proposed algorithm requires (8iterations) × (1MCS/iteration) = 8MCSs, and performing MCS for all combinations of 100 sub-intervals requires (100×100combinations) × (1MCS/combination) = 10000MCSs. Thus, the proposed algorithm is

Table 4.7 Search History of Worst-case Probability of Failure

Iteration	$X_{10}^{\mathrm{I}}(\theta_1)$	$X_{11}^{\mathrm{I}}(\theta_2)$	P_{F_2}	$\partial P_{F_2} / \partial X_{10}^{\mathrm{I}}$	$\partial P_{F_2} / \partial X_{11}^{\mathrm{I}}$
1	5.000	10.00	0.50788	-3.940E-04	4.0768E-04
2	0.000	5.000	0.50476	1.505E-03	5.479E-04
3	0.000	5.000	0.50478	1.486E-03	5.205E-04
4*	10.00	15.00	0.49676	-2.301E-03	-1.345E-03
3[b]	10.00	8.502	0.50160	-2.249E-03	-1.190E-04
4	4.189	6.467	0.50828	-5.640E-05	2.800E-04
4[b]	3.015	15.00	0.50343	3.712E-04	1.362E-03
5	**3.993**	**7.887**	**0.50849**	**-2.790E-05**	**2.1116E-07**

*: Discarded during *Step 5* of Worst-case Probability of Failure Search
[b]Utilized for Interpolation

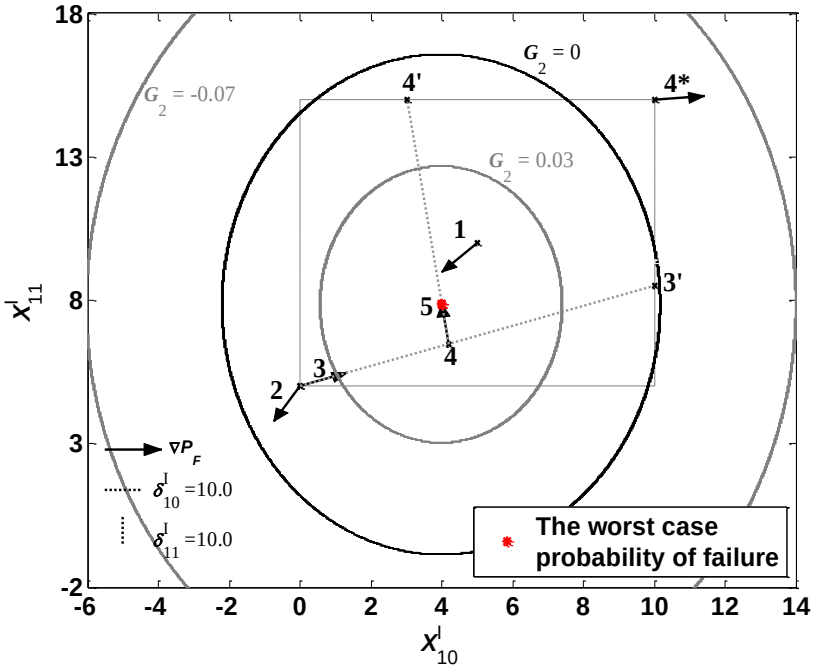

Figure 4.6 Search History of Worst-case Probability of Failure

1250 times more efficient while maintaining accuracy in this example. As suggested by the current and the previous examples, the more interval variables there are, the less efficient performing the crude MCS exponentially becomes. In general dimension, performing the MCS for all combinations of 100 sub-intervals of every interval variable requires (100^{NI} combinations) × (1MCS/combination) = $(10)^{2NI}$ MCSs. On the other hand, the proposed algorithm requires similar number of MCSs regardless of dimension of interval variables since it utilizes a vector of interval variables and its sensitivity vector instead of their individual components.

The efficiency of the crude MCS introduced in this paper can be itself improved using the advanced DOE technique. However, it is not further considered in the study in this chapter, since it is introduced solely for the comparison with the proposed method

.

Table 4.8 Comparison of Results Obtained by 2 Different Methods

Methods	Worst-case Interval Variable	Probability of Failure	Number of MCSs
Proposed Algorithm	[3.993 7.887]	0.50849	8
Performing MCS for all combinations of 100 sub-intervals	[3.939 7.879]	0.5085	10000

4.5.3 Design Optimization with Mixture of Random and Interval Variables

This numerical example shows the design optimization with mixture of random and interval variables, utilizing the worst-case probability of failure search. Consider a 2D mathematical design optimization problem, which is formulated to

$$\begin{aligned} &\text{minimize} \quad C(\mathbf{d}) = d_1 + d_2 \\ &\text{subject to} \quad P_{F_j}^{\text{worst}} = P\left[G_j\left(\mathbf{X}^{\mathbf{R}}(\mathbf{d}), \mathbf{X}_j^{\mathbf{I,worst}}\right) > 0 \right] \le P_{F_j}^{\text{tar}} = 2.275\%, \quad j = 1 \sim 3 \\ &\qquad \mathbf{d}^{\text{L}} \le \mathbf{d} \le \mathbf{d}^{\text{U}}, \quad \mathbf{d} \in \text{R}^2, \quad \mathbf{X}^{\mathbf{R}} \in \text{R}, \quad \text{and} \quad \mathbf{X}^{\mathbf{I}} \in \text{R} \end{aligned} \tag{4.47}$$

where three constraints are given by

$$G_1(\mathbf{X}) = 1 - \frac{\left(X_1^{\mathrm{I}}\right)^2 X_2^{\mathrm{R}}}{20}$$
$$G_2(\mathbf{X}) = 1 - \frac{\left(X_1^{\mathrm{I}} + X_2^{\mathrm{R}} - 5\right)^2}{30} - \frac{\left(X_1^{\mathrm{I}} - X_2^{\mathrm{R}} - 12\right)^2}{120} \tag{4.48}$$
$$G_3(\mathbf{X}) = 1 - \frac{80}{\left(X_1^{\mathrm{I}}\right)^2 + 8X_2^{\mathrm{R}} + 5}$$

The properties of two input variables, one interval and one random variable, are shown in Table 4.9. As shown in Equation (4.47), the target probability of failure $\left(P_{F_j}^{\mathrm{tar}}\right)$ is set to 2.275% for all constraints.

Table 4.9 Property of Input Variables

Input Variables	Variable Types	$\mathbf{d}^{\mathbf{L}}$	$\mathbf{d}^{\mathbf{O}}$	$\mathbf{d}^{\mathbf{U}}$	Parameters
X_1^{I}	Interval	0	5	10	$\delta_1^{\mathrm{I}} = 1.2$
X_2^{R}	Random	0	5	10	$\sigma_2 = 0.4$

Figure 4.7 shows the optimum design of the sampling-based design optimization with interval and random variables. As can be seen in Figure 4.7, the deterministic design optimum ($\mathrm{d}^{\mathrm{dopt}}$) was first searched to enhance efficiency of the design optimization procedure. In Figure 4.7, the dotted box illustrated around the design optimum ($\mathrm{d}^{\mathrm{opt}}$) shows the joint range of X_1^{I} and X_2^{R}. With $P_{F_j}^{\mathrm{tar}}$ of 2.275%, allowed total range of distribution of X_2^{R} becomes $4 \times \sigma_2 = 1.6$, and with $\delta_1^{\mathrm{I}} = 1.2$ of X_1^{I}, size of the dotted box becomes 1.2×1.6. With the dotted box around $\mathrm{d}^{\mathrm{opt}}$ it is easily identified that $\mathrm{d}^{\mathrm{opt}}$ is the desired optimum as vertices of the box are right on two active constraints, $G_1(\mathbf{X}) = 0$ and $G_2(\mathbf{X}) = 0$. $P_{F_1}^{\mathrm{worst}}$ and $P_{F_2}^{\mathrm{worst}}$ occur on the left and the right bounds of X_1^{I}, respectively where $P_{F_1}^{\mathrm{worst}}$ and $P_{F_2}^{\mathrm{worst}}$ are 0.0231 and 0.0228, respectively, which are very close to $P_{F_j}^{\mathrm{tar}}$. Design search history, number of iterations taken to obtain the worst-case probability of failure for each constraint, and total number of iterations at each design search iteration, which is the summation of numbers of worst-case probability of failure searches, are shown in Table 4.10. One MCS for each iteration is used to obtain $P_{F_j}^{\mathrm{worst}}$ and $\nabla P_{F_j}^{\mathrm{worst}}$ while applying the worst-

case probability of failure search explained in Section 4.2. At the 2nd iteration during the design search, $P_{F_2}^{\text{worst}}$ does not behave monotonic within the domain of the interval variable, thus the interpolation algorithm is applied to find more accurate worst-case probability of failure, which is why 5 iterations are taken to obtain $P_{F_2}^{\text{worst}}$. Overall iterations taken to obtain $P_{F_j}^{\text{worst}}$ is around 2 for each design search since P_{F_2} behaves monotonic most times within the domain of the interval variable. Thus, it is concluded that the computational burden to obtain $P_{F_j}^{\text{worst}}$ in this example is affordable.

Table 4.10 Design Search History and Number of Iterations for Worst-case Probability of Failure

Iteration	Design Point (d_1, d_2)	# Iterations for $P_{F_1}^{\text{worst}}$	# Iterations for $P_{F_2}^{\text{worst}}$	# Iterations for $P_{F_3}^{\text{worst}}$	# Total Iterations
1	(3.1139, 2.0639)	2	2	2	6
2	(4.3814, 3.6368)	2	5	2	9
3	(3.8142, 2.9765)	2	2	2	6
4	(2.8478, 3.0296)	2	2	2	6
5	(3.1377, 3.0137)	2	2	2	6
6	(3.3407, 3.0025)	2	2	2	6
7	(3.3741, 3.1111)	2	2	2	6
8	(3.3838, 3.1274)	2	2	2	6

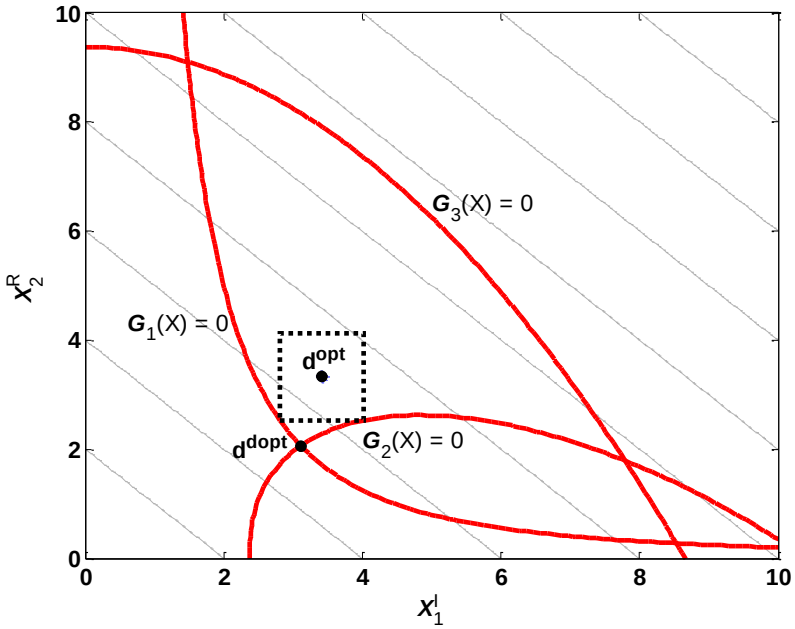

Figure 4.7 Optimum Design of Sampling-Based Design Optimization with Random and Interval Variables

4.6 Conclusions

Sampling-based design optimizations with only interval variables and with both interval and random variables are developed. It is assumed that the surrogate models or actual functions are given and does not aim to improve the efficiency of obtaining surrogate model. For the design optimization with interval variables only, each of the worst-case constraint is evaluated by the developed worst-case performance search where interval and sensitivity vector are utilized, thus efficiency is promised regardless of the dimension of the interval variables, when function evaluation of surrogate model is inexpensive. It is assumed that gradients of performance functions are not available. Therefore, sensitivities of a performance function with respect to interval variables are derived by defining behavior of the interval variables at the worst-case by the Dirac delta function to calculate it by the sampling-based method. Through the simulation analysis, desired value of standard deviation for the interval variables at the worst-case is determined, and the error of the result turns out to be negligible at the desired value. Using the obtained value, the sensitivities of each of the worst-case constraints both at the worst-case and design points are calculated by

the MCS. For the design optimization with random and interval variables, the worst-case probabilistic constraints are evaluated by the worst-case probability of failure search. Since probability of failure does not always occur where the worst-case performance occurs as demonstrated in the study in this chapter, the worst-case probability of failure is obtained by directly using the probability of failure and its sensitivity. Similarly to design optimization with interval variables only, the sensitivities of the probability of failure both at the worst-case and design points are derived, which are then calculated by the MCS. Numerical examples show the worst-case probability of failure is obtained for both low and high-dimensional inputs regardless of the dimension of the interval variables within a few design cycles. On the other hand, the proposed method is still limited to the cases where function evaluations of the surrogate models are not heavy. The design optimum with random and interval variables can be successfully obtain within a few design cycles utilizing the proposed worst-case probability of failure search.

Chapter 5. Reliability-Oriented Optimal Design of Intentional Mistuning for Bladed Disk with Random and Interval Uncertainties

5.1 Introduction

Bladed disks are widely used in turbomachinery. While they are designed to be spatially periodic, bladed disks in practical systems are inevitably subject to uncertainties in geometrical and material properties due to manufacturing tolerance and in-service degradation which generally break the ideal periodicity. Usually, the uncertainties are small, which are referred to as mistuning. A well-known problem in bladed disks is that vibration localization could occur even with small mistuning (Yoo *et al*. 2003; Chan and Ewins 2011). When vibration localization occurs, the vibration modes and/or the forced responses under engine-order excitations become drastically different from their counterparts under ideal periodicity, which may cause catastrophic consequence (Bladh *et al*. 2003; Castanier and Pierre 2006). A significant amount of research has been carried out to elucidate the vibration localization phenomenon and to quantify its negative effects (Choi *et al*. 2003; Petrov and Ewins 2003; Kenyon *et al*. 2005; Beirow *et al*. 2014; Beirow *et al*. 2015). Mathematically, vibration localization is caused by the near singularity in the eigensolution sensitivity of bladed disks with relatively weak inter-blade coupling (e.g., the coupling due to the disk) (Shapiro and Willcox 2003).

Since the uncertain mistuning in bladed disks in general causes detrimental effects, a number of recent studies have attempted to tackle this issue. One type of approaches is through integrating passive control devices such as piezoelectric circuitry where piezoelectric transducers are integrated onto individual blades to convert part of the vibration energy into electrical energy (Tang and Wang 2003). The converted electrical energy can propagate freely through a well-design circuitry network with strong inter-blade-circuit coupling (Yu *et al*. 2006; Kauffman *et al*. 2012). A severe limitation of such type of approaches is that piezoelectric transducers cannot sustain high temperature which however is commonly experienced in turbomachinery. Alternatively, the technique of *intentional mistuning* has been investigated. In this type

of approaches, a pre-specified blade-to-blade design modification is introduced directly into the baseline design, intentionally breaking the ideal periodicity in a deterministic manner (Castanier and Pierre 2002; Martel *et al*. 2007). Several investigations have suggested certain patterns/distributions of intentional mistuning that help reducing the vibration localization (Choi *et al*. 2003; Nikolic *et al*. 2008).

The ultimate purpose of analyzing bladed disks with uncertain mistuning and then performing design optimization is to improve their reliability (Castanier and Pierre 2006). To measure the reliability of a bladed disk in operation, failure and non-failure scenarios need to be examined first. Failure can be chosen to be defined as the maximum response amplitude amongst the blades within the interested excitation frequency range (typically around a resonant frequency) exceeding a threshold value. That threshold value is called the maximum allowed amplitude. Since the uncertainties cause response amplification (e.g., vibration localization), in this context, it is natural to introduce the concept of *reliability analysis* which involves the analysis of the *probability of failure*. Performing reliability analysis, meanwhile, requires taking a closer look at the unwanted but inevitably existing uncertain mistuning. Generally, there are three types of epistemic uncertainties which can be listed in the ascending order of uncertainty degree as: random uncertainty, fuzzy uncertainty, and interval uncertainty (Du *et al*. 2005; Youn *et al*. 2007). Random uncertainty is defined as the uncertainty of which the complete probabilistic distribution is known. Interval uncertainty, on the other hand, is defined as the uncertainty of which only the interval (i.e., the lower and upper bounds) is known while the probabilistic distribution is unknown.

It is worth mentioning that most of the studies concerning reducing vibration localization in bladed disks have so far focused on the underlying physics, e.g., how the vibratory energy would be more evenly distributed from wave/mode analysis standpoint. In terms of quantitative analysis, some optimization formulations were proposed to identify specific intentional mistuning design to minimize the maximum response amplitude amongst the blades, aiming at improving the reliability of the bladed disk (Choi *et al*. 2003; Han *et al*. 2014). While these formulations may certainly benefit the aforementioned reliability, strictly speaking they cannot yield an optimal design under a pre-specified reliability level. That is, in

these studies, the objective is to find, for example, how to mix two different types of identical blades, i.e., how to find the intentional mistuning pattern with given design modification level, to minimize the maximum blade response amplitude. Therefore, one may either reach an overly conservative design that satisfies the reliability requirement but suffers from too much design modification that deteriorates aerodynamic performance, or, reach a design that albeit is optimal under the optimization formulation but still cannot satisfy the reliability requirement. It should also be pointed out that these optimization studies are usually carried out under the assumption that the uncertain mistuning is random with known distribution. This, however, may not always be the actual case since the disk that couples the blades contains uncertainty as well. For example, it is well known that for inserted blades the blade-disk connectivity is subjected to complex contact mechanics which may not be described as random variation (Petrov and Ewins 2006). Also, for new-generation of integrally bladed rotors that are machined from a solid piece of material, the assumption of blade mistuning being random becomes more questionable and the distribution becomes very hard to extract experimentally. Clearly, in reality at least some of the uncertainties involved in bladed disk analysis should be treated as interval ones.

The goal here is to formulate a new mathematical framework of reliability-oriented robust design for bladed disks using intentional mistuning. Design modification is introduced as a pre-specified pattern of blade nominal stiffness, i.e., intentional mistuning. In this new framework, different from all previous studies, the design optimization is cast into the minimization of the level (magnitude) of the design modification in which a pre-specified reliability level is given as a constraint. As one pre-specifies the reliability level, the robust performance can be ensured. In the case that the design modification level identified exceeds the allowable level, a different pattern of design modification can be then explored. This type of robust analysis/design naturally fits the scenario in which some of the uncertainties are interval, since the optimal design is reached in the context of reliability. Without loss of generality, here it is assumed that the blade mistuning is random while the disk connection is subjected to interval uncertainty. The main technical challenge of this research is the computational cost involved: analyzing interval

uncertainty effect itself is computationally intensive, and further applying such analysis to find the optimal design in the parametric space is also costly. Indeed, due to the presence of interval uncertainty, the maximum response will have bounds, which however are distributed due to the presence of random uncertainty. Finding the bounds of the maximum response is not straightforward because the maximum response behaves non-monotonically with respect to inter-blade coupling, owing to the complicated nonlinear relation between them.

To tackle the above-mentioned issues, in the research in this chapter a suite of algorithms that can efficiently evaluate the response bounds due to interval uncertainty that are also subjected to random uncertainty are developed, and the optimal design is then identified. The behavior of reliability of the bladed disk with respect to its maximum response amplitude is monotonic, i.e., the greater the maximum response amplitude is, the larger the probability of failure becomes. Therefore here a sequential treatment of interval and random uncertainties is proposed. The response bounds due to interval uncertainty, which are global minimum and maximum for the maximum response amplitude amongst all blades within interested frequency range, are firstly searched under given intervals of uncertain parameters. Owing to the fact that there will be more than one possible scenario for global minimum/maximum caused by the near singularity of bladed disk responses, an algorithm is developed based on the Metropolis-Hastings technique, and it will efficiently narrow the search down into one possible scenario and then further converge closely to true global minimum/maximum (Brooks *et al*. 2011). The random uncertainty is then analyzed by using Monte Carlo simulation and subsequently the reliability of the bladed disk is obtained. In order to optimize the intentional mistuning efficiently, a gradient- or sensitivity-based approach is formulated, and it requires the computation of sensitivities of both the objective function and the constraint with respect to design variables.

5.2 Vibration of a Bladed Disk with Uncertainties

5.2.1 System Equation of Motion without Uncertainty

The purpose of this research in this chapter is to establish a mathematical framework for reliability-oriented design optimization of bladed-disks. It is not uncommon to adopt surrogate dynamic models during design optimizations owing to the high computational cost involved (Choi *et al*. 2003; Hao *et al*. 2012). Here, without loss of generality, a surrogate model of bladed disk is adopted, and it is shown in Figure 5.1 (Choi *et al*. 2003; Beirow *et al*. 2014). Each blade features one DOF (degree-of-freedom), and the disk coupling is represented by coupling stiffness. The blade mass m_b, stiffness k_b and damping c_b and the disk coupling stiffness k_c can be acquired from order-reduced modeling from a full-scale finite element model or from experiment. It starts from the modeling of ideal bladed disk without mistuning. Let y_j denote the displacement of the *j*-th blade ($j = 1, 2, \cdots, N_b$; N_b is the total number of blades). For the *j*-th blade, the dynamic equation is given as

$$m_b \ddot{y}_j + c_b \dot{y}_j - k_c y_{j-1} + \left(k_b + 2k_c\right) y_j - k_c y_{j+1} = F_j(t) \tag{5.1}$$

where $F_j(t)$ is the force applied to the *j*-th blade due to aerodynamic load. Collecting the displacements and forces into vectors $\mathbf{y} = (y_1, y_2, ..., y_{N_b})^T$ and $\mathbf{F}(t) = (F_1, F_2, ..., F_{N_b})^T$, the matrix form equation of motion is available as

$$\mathbf{M}\ddot{\mathbf{y}} + \mathbf{C}\dot{\mathbf{y}} + \mathbf{K}\mathbf{y} = \mathbf{F}(t) \tag{5.2}$$

where $\mathbf{M}$, $\mathbf{C}$, and $\mathbf{K}$ are the mass, damping, and stiffness matrices, respectively. As bladed disk vibration is considered, the forcing function takes the form of engine-order excitation (Choi *et al*. 2003), i.e.,

$$\mathbf{F} = F \cdot e^{j\omega t}\left\{1, e^{j\phi_2}, ..., e^{j\phi_{N_b}}\right\} = e^{j\omega t} \cdot \mathbf{F}_0, \qquad \phi_i = 2\pi d\left(i-1\right)/N_b \tag{5.3a, b}$$

where d is the engine order ($d = 0,1,\cdots,N_b - 1$), F is the force magnitude constant, $\mathbf{F}_0$ represents the force distribution throughout the bladed disk, and ω is the excitation frequency. Under an engine order excitation, all the blades experience the same force magnitude but with a certain phase difference. In general, a bladed disk is lightly damped, and in this research proportional damping is assumed.

The following eigenvalue problem is solved,

$$\left[\mathbf{K} - \omega_{n,i}^2 \mathbf{M}\right]\boldsymbol{\varphi}_i = \mathbf{0} \tag{5.4}$$

where $\omega_{n,i}^2$ and $\boldsymbol{\varphi}_i$ are the i-th natural frequency and the corresponding mode shape. Let the mass-normalized modal matrix of the system be denoted by $\boldsymbol{\Phi}$. The modal transform is then introduced as

$$\mathbf{y} = \boldsymbol{\Phi}\boldsymbol{\eta} \tag{5.5}$$

where $\boldsymbol{\eta}$ is the vector of modal responses. Substituting Equation (5.5) into Equation (5.1) and left-multiplying Equation (5.1) by $\boldsymbol{\Phi}^T$, owing to the orthogonal condition the de-coupled equations is obtained in the modal space as

$$\ddot{\eta}_i + \mathrm{diag}\left[2\zeta_i\omega_{n,i}\right]\dot{\eta}_i + \mathrm{diag}\left[\omega_{n,i}^2\right]\eta_i = e^{j\omega t}\boldsymbol{\varphi}_i^T\mathbf{F}_0 \qquad (i = 1,2,\cdots,N_b) \tag{5.6}$$

where ζ_i is damping ratio for the i^{th} mode. Let the modal response be represented as $\eta_i = h_i e^{j\omega t}$. The modal response amplitude can be solved as

$$h_i = \frac{\varphi_i^T F_0}{-\omega_f^2 + 2\zeta_i\omega_{n,i}\omega_f j + \omega_{n,i}^2} \qquad (i = 1,2,\cdots,N_b) \tag{5.7}$$

The response of the bladed disk can then be obtained as

$$\mathbf{y} = \left|\mathbf{Y}\right|e^{j\omega t} = \left|\boldsymbol{\Phi}\mathbf{h}\right|e^{j\omega t}. \tag{5.8}$$

where $\mathbf{h} = (h_1, h_2, ..., h_{N_b})^T$.

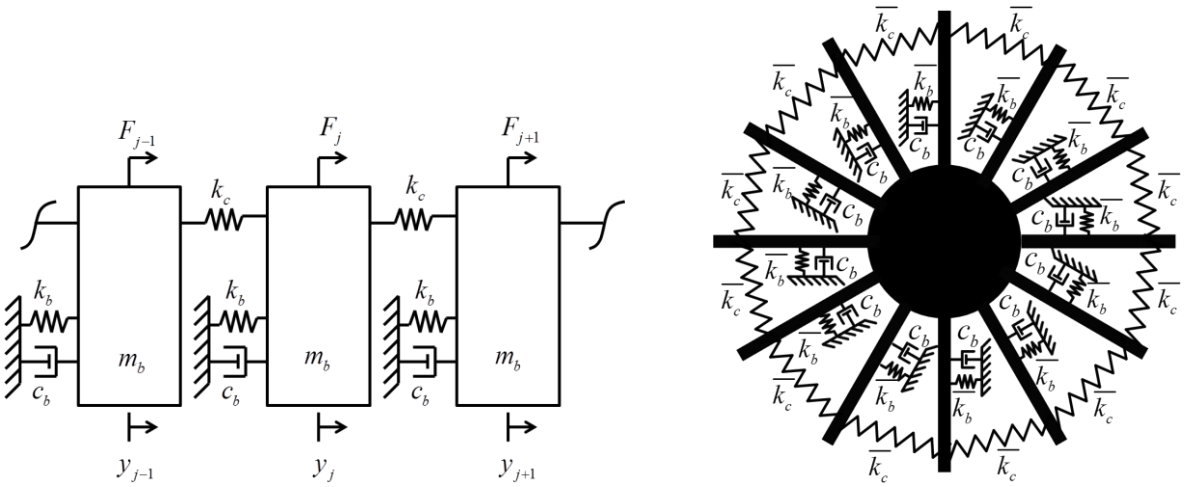

(a) (b)

Figure 5.1 Surrogate bladed disk model (Choi *et al*. 2003; Beirow *et al*. 2014). (a) Local detail; (b) Bladed disk overview.

5.2.2 Mathematical Expressions of Uncertain Mistuning

Recall Equation (5.1). The stiffness matrix of the bladed disk can be written as

$$\mathbf{K} = \mathbf{K}_b + \mathbf{K}_c \tag{5.9}$$

where

$$\mathbf{K}_b = \mathrm{diag}\left[k_b\right]_{N_b \times N_b} \tag{5.10}$$

and

$$\mathbf{K}_c = \begin{bmatrix} 2k_c & -k_c & & 0 & & -k_c \\ -k_c & 2k_c & -k_c & & 0 & \\ & \cdot & \cdot & \cdot & & 0 \\ 0 & & \cdot & \cdot & \cdot & \\ & 0 & & -k_c & 2k_c & -k_c \\ -k_c & & 0 & & -k_c & 2k_c \end{bmatrix}_{N_b \times N_b} . \tag{5.11}$$

Indeed, the stiffness matrix includes the contribution from the blades, $\mathbf{K}_b$, and that from the disk coupling, $\mathbf{K}_c$. In the research in this chapter, without loss of generality, it is assumed that uncertainties of bladed disk are characterized by stiffness variations, and the mass matrix remains unaffected. It is further assumed that there exist two types of uncertainties, i.e., random uncertainty of blades and interval

uncertainty of disk coupling. Blades are usually made through batch process and, in the case of inserted blades, the distribution of blade mistuning can be measured directly. The uncertainty of disk coupling, on the other hand, may depend on local contact conditions etc., and its distribution may not be easily measured. As such, the uncertainty of disk coupling is quantified with a higher uncertain degree, i.e., using interval uncertainty. It is worth noting that the proposed method presented in this research can be extended to cases where blades also have interval uncertainty.

The stiffness matrix of the bladed disk with uncertainties is then written as

$$\mathbf{K}^U = \mathbf{K}_b^R + \mathbf{K}_c^I \tag{5.12}$$

where the superscripts indicate 'uncertain', 'random', and 'interval', respectively. The random stiffness matrix of the blades is

$$\mathbf{K}_b^R = \mathrm{diag}\left[k_{b,1}^R, k_{b,2}^R, ..., k_{b,N}^R \right]_{N_b \times N_b} \tag{5.13}$$

The interval stiffness matrix of the disk coupling is

$$\mathbf{K}_c^I = \begin{bmatrix} 2k_{c,1}^I & -k_{c,2}^I & & 0 & & -k_{c,N_b}^I \\ -k_{c,1}^I & 2k_{c,2}^I & -k_{c,3}^I & & 0 & \\ & \cdot & \cdot & \cdot & & 0 \\ 0 & & \cdot & \cdot & \cdot & \\ & 0 & & -k_{c,(N_b-2)}^I & 2k_{c,(N_b-1)}^I & -k_{c,N_b}^I \\ -k_{c,1}^I & & 0 & & -k_{c,(N_b-1)}^I & 2k_{c,N_b}^I \end{bmatrix}_{N_b \times N_b} \tag{5.14}$$

In the above two expressions, $k_{b,j}^R$ ($j = 1, 2 \cdots, N_b$) is the random stiffness of the *j*-th blade which follows a pre-specified distribution, and $k_{c,j}^I$ ($j = 1, 2 \cdots, N_b$) is the interval stiffness of the *j*-th coupling spring with lower and upper bounds. The uncertainty in each element is independent to each other.

5.3. Reliability Analysis of a Bladed Disk with Interval and Random Uncertainties

For the analysis of the reliability, the performance function is firstly considered, and it can be defined as the difference between the maximum response among all blades in the excitation frequency range of interest (i.e., around a resonant frequency) and the maximum allowed response, which can be written as

$$g = |X|_{\max} - |\mathrm{X}|_{\mathrm{allow}} \tag{5.15}$$

Note the response of the bladed disk calculated using Equation (5.8) is denoted as $\mathbf{y}$ which also depends on the excitation frequency. Here $|X|_{\max}$ denotes the maximum blade response over the interested frequency range, and $|\mathrm{X}|_{\mathrm{allow}}$ denotes the maximum allowed response amplitude. Italic font is used in $|X|_{\max}$ to indicate that the maximum blade response is uncertain in nature. Following this definition, the system is considered safe if $g < 0$ and is considered as failure if $g > 0$. With random uncertainty being involved, this evaluation of reliability becomes probabilistic, and reliability needs to be determined by analyzing the probability of failure. The uncertainty analysis in this chapter involves the mixture of interval and random uncertainties. As a result, the performance function is not only distributed but also bounded. To ensure reliability, the upper bound of performance function, i.e., the worst-case performance function value, should be solved (Du *et al*. 2005). The concepts of reliability and probability of failure with mixture of random and interval uncertainties are illustrated in Figure 5.2, where g_{lower} and g_{upper} represent the lower and upper bounds of performance function, respectively.

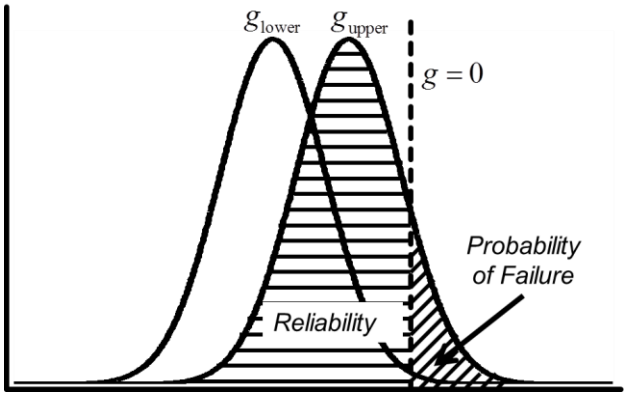

Figure 5.2 Concepts of reliability and probability of failure with mixture of random and interval uncertainties.

The computational cost for reliability analysis with mixture of interval and random uncertainty increases dramatically as compared with that with random uncertainty only. The nominal worst-case must be first identified under the interval uncertainty of disk connection, followed by the standard reliability analysis under blade random uncertainty. Thus, it requires a "double-loop" computational process. Based on the definitions of the performance function and failure (Figure 5.2), it can be observed that in general the greater the performance function value is, the less reliable the design becomes. Reliability can therefore be measured via a sequential approach, i.e., one dealing with the interval uncertainty which searches for the upper or the maximum performance function, and the other dealing with the random uncertainty which calculates distribution of the maximum performance function (Du *et al*. 2005).

5.3.1. Interval Analysis under Disk Connection Uncertainty

It starts from analyzing response under interval disk connection uncertainty only. Since the upper bound of performance function occurs at the maximum response, the worst-case combination of interval uncertainties that maximizes the vibration response needs to be found. Traditionally, this has been achieved by considering all possible combinations of interval uncertainties (Mourelatos *et al*. 2005; Yoo and Lee 2014). The steps of executing this method involve dividing all interval uncertainties into a discrete number of sub-intervals and calculating vibration responses for all possible combinations of these sub-intervals. The worst-case combination can then be determined by finding the actual maximum

responses. While intuitive, for this particular problem of bladed disk analysis, the computational cost would be impractical. For instance, let there be 12 numbers of blade in the assembly, and let each interval disk connection between the adjacent blades be divided into 10 sub-intervals. There would be a total of 10^{12} response calculations.

Here it is proposed to resort to an efficient, sampling-based technique, known as the Metropolis-Hastings (M-H) algorithm (Cai *et al*. 2008), to solve the above-mentioned challenge. The M-H algorithm is a Markov chain Monte Carlo method, and its primary application is to identify multi-dimensional output distribution by generating input random samples (Roberts and Rosenthal 2001). In the research in this chapter the M-H algorithm is modified such that the stopping criterion is deterministic instead of probabilistic, since the distribution information is unknown inside the uncertainty interval. The proposed method with appropriate choice of convergence parameters will efficiently narrow the search down into one possible scenario and then further converge to true global minimum/maximum. Other sampling-based methods such as Latin Hypercube sampling or Genetic Algorithm will be relatively inefficient choices for this problem, since they essentially will search through all possible scenarios (Helton and Davis 2003; Sivanandam and Deepa 2007).

The flowchart of the proposed method that searches for the worst-case interval coupling stiffness combination, denoted by $\boldsymbol{k}_c^{\text{worst}}$, with N_{ws} number of iterations, is shown in Figure 5.3. The procedure can be summarized as:

Step 1. Decide the number of samples N_{ws}. (Based on case studies in this research, the recommended value of N_{ws} is between 500 and 1000. However it can be further adjusted if convergence is not achieved.) Set the iteration counter $j = 0$. Initialize $\boldsymbol{k}_c^{(0)}$ by drawing $\boldsymbol{k}_c^{(0)}$ from *uniform distribution* between $\boldsymbol{k}_c^L$ and $\boldsymbol{k}_c^U$ where the superscripts L and U indicate, respectively, the lower and upper bounds.

Step 2. Propose a value for $\boldsymbol{k}_c^{(j)}$, which is denoted by $\boldsymbol{k}_c^*$, by drawing $\boldsymbol{k}_c^*$ from $N\left(\boldsymbol{k}_c^{(j)}, \boldsymbol{\sigma}_{\boldsymbol{k}_c^{(j)}}\right)$ where

$$\sigma_{\boldsymbol{k}_c^{(j)}} = \left(\boldsymbol{k}_c^U - \boldsymbol{k}_c^L\right)(\rho)^j \gamma \tag{5.16}$$

where ρ and γ are adjustable parameters to expedite the convergence (Roberts and Rosenthal 2001). Repeat *Step 2*, until $\boldsymbol{k}_c^L \le \boldsymbol{k}_c^* \le \boldsymbol{k}_c^U$. Please note that value of ρ is usually close to 1.

Step 3. Check the stopping criterion that is given as

$$\min\left[\left|x\right|_{\max}^* / \left|x\right|_{\max}^{(j)}, 1\right] \ge 1 \tag{5.17}$$

where $\left|x\right|_{\max}^*$ and $\left|x\right|_{\max}^{(j)}$ are the maximum blade responses solved over the interested frequency range under coupling stiffness combinations $\boldsymbol{k}_c^*$ and $\boldsymbol{k}_c^{(j)}$, respectively. If the stopping criterion in Equation (5.17) is satisfied, $\boldsymbol{k}_c^{(j)} = \boldsymbol{k}_c^*$. The next iteration counter is set as $j = j + 1$.

Step 4. If $j < N_{ws}$, go to *Step 2*. If $j = N_{ws}$, $\boldsymbol{k}_c^{\text{worst}} = \boldsymbol{k}_c^{(j)}$.

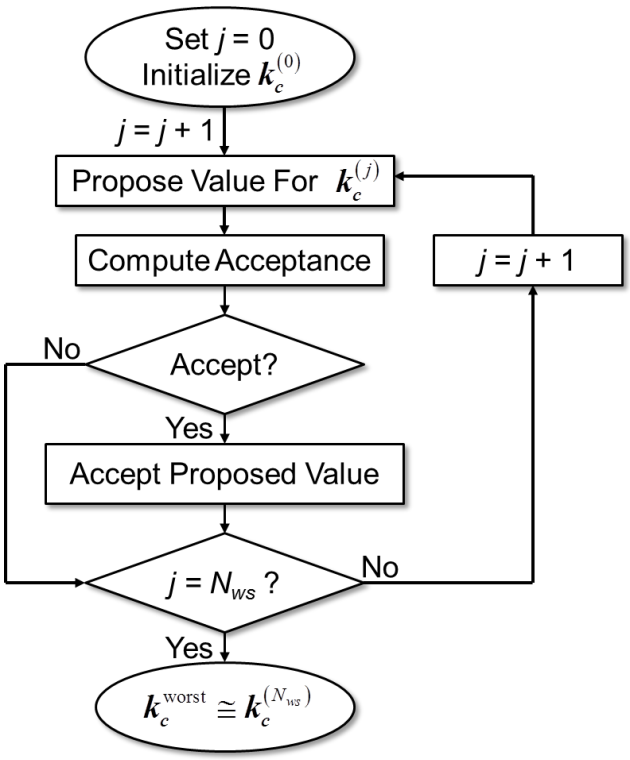

Figure 5.3 Flowchart of proposed M-H based method for worst-case interval coupling stiffness search.

To demonstrate the accuracy as well as the efficiency of the proposed M-H based method for the potential usage in bladed disk analysis, relatively simple examples are carried out first on two weakly-coupled bladed disks with 4 (even) and 5 (odd) blades, respectively. All other parameters are the same as those used in Section 5.5 on more complex structures and will be explained in detail later. For these two bladed disks with smaller number of blades and with interval uncertainty only, comprehensive worst-case analysis can be indeed carried out by using the traditional approach, i.e., discretizing each interval coupling into multiple sub-intervals and evaluating the responses under all possible combinations. Figure 5.4 show the responses for all possible combinations, based on which the worst-case response can be determined. Meanwhile, the results obtained by the traditional approach and the proposed M-H based method are compared in Figure 5.5 where responses are normalized with respect to the nominal response that is extracted without considering interval uncertainty. In Figure 5.5, the worst-case responses obtained by the proposed method for bladed disks with 4 and 5 blades are 109.06% and 133.32% of the nominal response, respectively, while those obtained by the traditional method are 108.90% and 132.63%. It can be observed that the M-H based method converges quickly to the worst-case response obtained by the traditional approach within just a few hundred iterations, which clearly demonstrates its efficiency. In terms of accuracy, the worst-case responses obtained by the proposed method are slightly higher than the ones obtained by the traditional approach (0.16% and 0.69%). This is due to the fact that the proposed method can search for the worst-case combination *continuously* within the intervals, while the traditional approach considers only the discrete combinations of sub-intervals. Since the proposed method can find slightly higher responses, it may be concluded that it gives better result in the context of searching for the worst-case responses. The worst-case combinations of interval couplings obtained by the proposed method are shown in Figure 5.6.

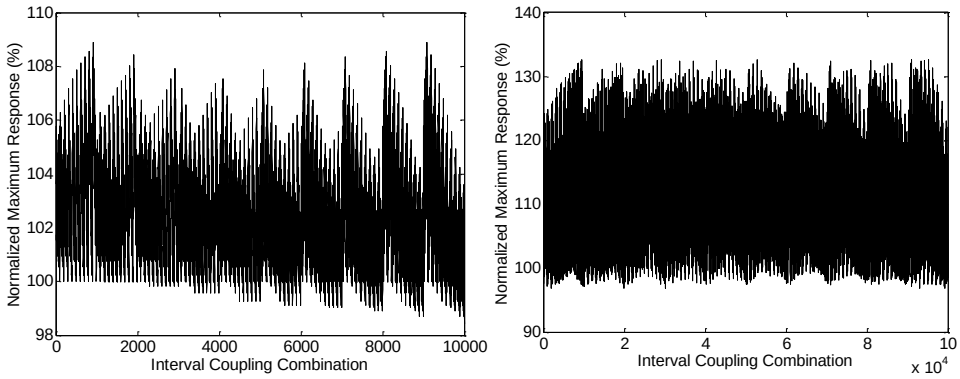

(a) (b)

Figure 5.4 Responses for all possible combinations of interval couplings for bladed disks. (a) 4 blades; (b) 5 blades.

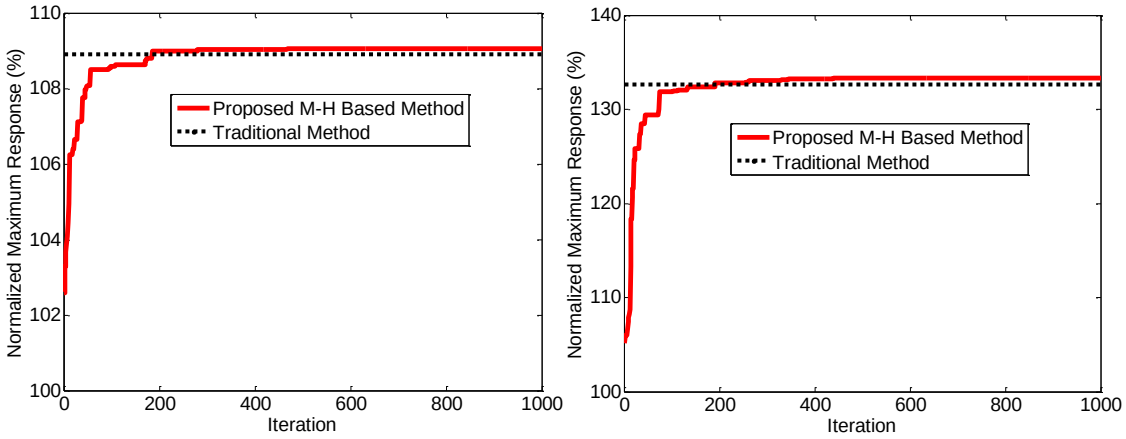

(a) (b)

Figure 5.5 Worst-case amplitude searches by the proposed M-H based method for bladed disks. (a) 4 blades; (b) 5 blades.

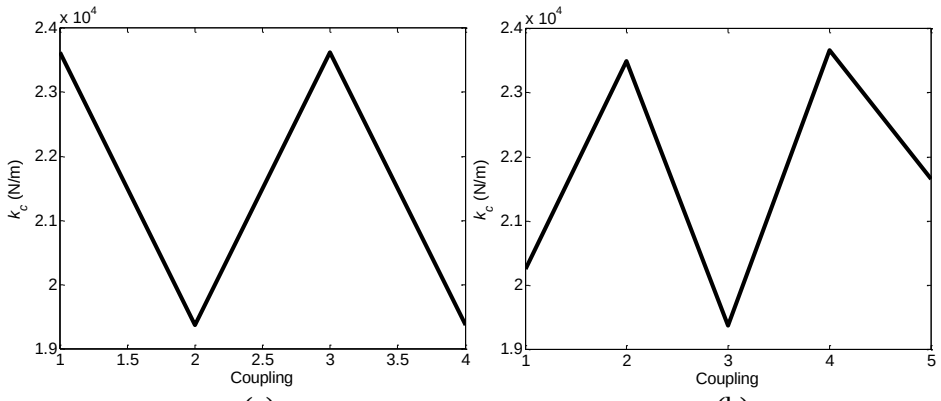

(a) (b)

Figure 5.6 Worst-case combinations of interval couplings obtained by the proposed M-H based method for bladed disks. (a) 4 blades; (b) 5 blades.

5.3.2. Reliability Analysis of a Bladed Disk

As the nominal worst-case performance function can be obtained by the method outlined in Section 5.3.1, the random effect of blades is then analyzed in this section. In this analysis, two effects should be considered, i.e., the amplification and the distribution of vibration response under uncertainties. As indicated by a number of previous studies, the random uncertainty in blades, namely *random mistunings*, causes significant amplification in vibration response (Bladh *et al*. 2003; Castanier and Pierre 2006). One instance of this phenomenon is illustrated in Figure 5.7, where the maximum vibration response of blades under random uncertainty of 1% is 1.356 times of the one without any uncertainty. Meanwhile, the amplified response is also distributed due to the nature of random uncertainty.

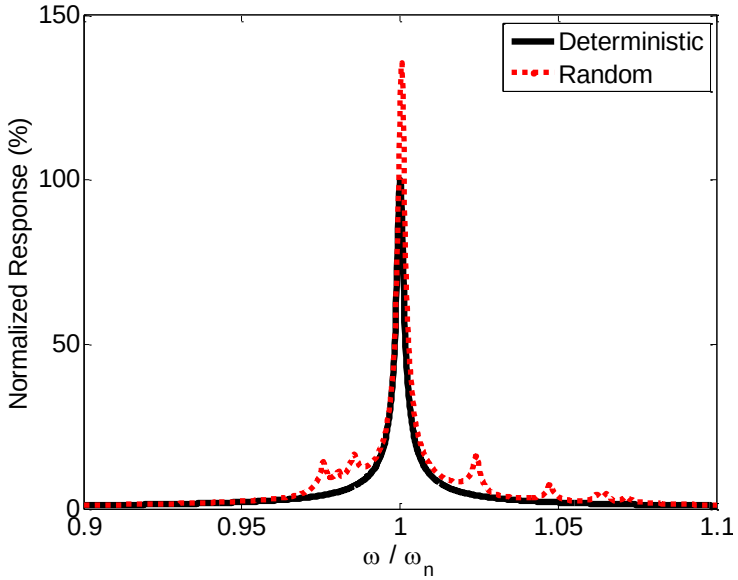

Figure 5.7 Response amplification of bladed disk with 1% of random uncertainty.

Owing to the complexity of the problem, the reliability analysis can only be performed numerically using sampling-based method. While sampling-based method generally requires high computational cost, with the surrogate model of bladed disk presented in Section 5.2, it is indeed practical. To proceed, safe and failure instances need to be defined first. Recall Equation (5.15). One instance of safe case and one of failure case are illustrated in Figure 5.8. Reliability analysis involves the calculation of the probability

of failure. As explained in the beginning of Section 5.3, the probability of failure should be considered under the worst-case condition, which is namely the worst-case probability of failure (Du *et al*. 2005; Yoo and Lee 2014),

$$P_F^{\text{worst}} = P\left[g_{\text{upper}} > 0 \right] = \int I_{\Omega_F}\left(|x|_{\max}^{\text{worst}} \right) f_{|X|_{\max}^{worst}}\left(|x|_{\max}^{\text{worst}} \right) d\,|x|_{\max}^{\text{worst}} = E\left[I_{\Omega_F}\left(|X|_{\max}^{\text{worst}} \right) \right] \tag{5.18}$$

where $|X|_{\max}^{\text{worst}}$ is the worst-case maximum response that is to be evaluated at the worst-case combinations of interval couplings, which is obtained using the M-H algorithm outlined in Section 5.3.1, $|x|_{\max}^{\text{worst}}$ is the realization of $|X|_{\max}^{\text{worst}}$ under Monte Carlo sampling of the random mistuning, Ω_F is the failure set defined as $\Omega_F \equiv \left\{ |x|_{\max}^{\text{worst}} \,|\, |x|_{\max}^{\text{worst}} > |\mathrm{X}|_{\text{allow}} \right\}$, $P[\cdot]$ is a probability measure, $f_{|X|_{\max}^{\text{worst}}}\left(|x|_{\max}^{\text{worst}} \right)$ is the probability density function (PDF) of $|X|_{\max}^{\text{worst}}$, and $E[\cdot]$ represents the expectation operator. $I_{\Omega_F}\left(|x|_{\max}^{\text{worst}} \right)$ in Equation (5.18) is an indicator function (Lee *et al*. 2011),

$$I_{\Omega_F}\left(|x|_{\max}^{\text{worst}} \right) = \begin{cases} 1, & |x|_{\max}^{\text{worst}} \in \Omega_F \\ 0, & \text{otherwise} \end{cases} \tag{5.19}$$

Through Monte Carlo simulation, the worst-case probability of failure can be calculated as

$$P_F^{\text{worst}} = E\left[I_{\Omega_F}\left(|X|_{\max}^{\text{worst}} \right) \right] \cong \frac{1}{K} \sum_{k=1}^{K} I_{\Omega_F}\left[|x|_{\max}^{\text{worst},(k)} \right]. \tag{5.20}$$

In Equation (5.20), *K* indicates the number of samples and 10,000 samples are used in this research. Finally, the reliability, denoted as *R*, can be obtained as

$$R = 1 - P_F^{\text{worst}}. \tag{5.21}$$

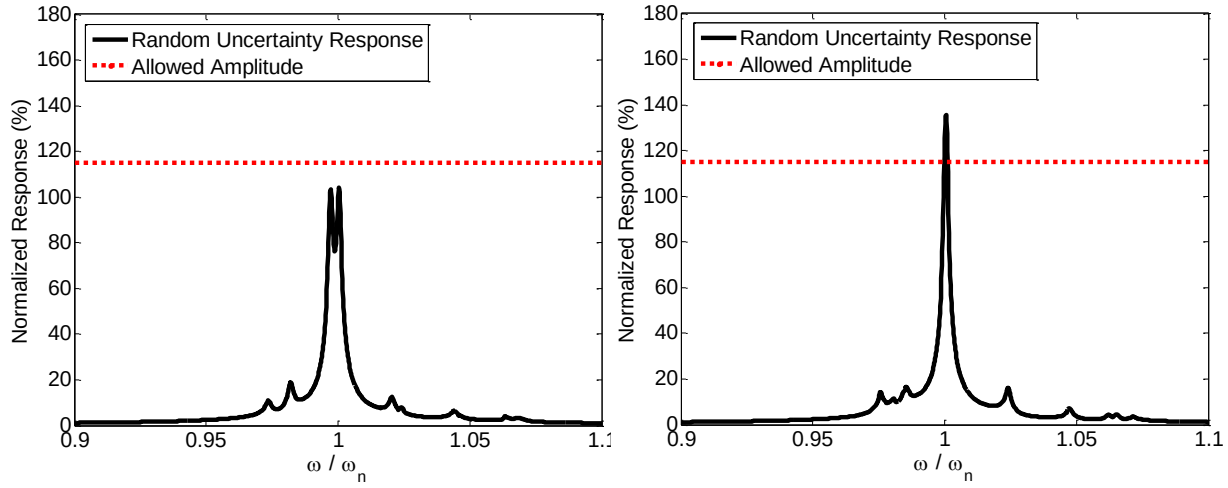

Figure 5.8 Bladed disk response with 1% of random uncertainty; (a) A safe instance; (b) A failure instance.

5.4. Formulation of Design Optimization of a Bladed Disk Using Intentional Mistuning and Sensitivity Analysis

5.4.1. Intentional Mistuning

The fundamental idea of intentional mistuning is to alter the nominal bladed disk with pre-specified design modification to break up the spatial periodicity that is the root cause of high sensitivity of vibratory with respect to uncertainties. Previous studies have suggested introducing particular patterns of blade stiffness modifications for intentional mistuning (Yu *et al*. 2011). Examples of these patterns include those that follow linear, harmonic, and pseudo harmonic trends. In this research, without loss of generality, the spatially harmonic pattern is chosen for illustration. That is, the nominal blade stiffness becomes

$$k_{b_i} = \overline{k_b} + \Delta k_{b_i} = \overline{k_b} + \tau \overline{k_b} \sin\left\{\frac{(i-1)\phi}{N_b}\right\} \tag{5.22}$$

where $\overline{k_b}$ is the original nominal blade stiffness, and τ and ϕ are the intentional mistuning parameters. Indeed, τ defines the percentage modification of the equivalent blade stiffness with respect to the original value, and ϕ defines the specific spatially harmonic pattern. Here we allow ϕ to be non-multiples of

π, because intentional mistuning is small in stiffness modification, and does not have to follow a periodic pattern (Zhou *et al*. 2017). This will allow flexibility in stiffness pattern realization. It is also worth noting that in practice, the stiffness of individual blade can be changed by various means such as geometry modification of the blade. The actual relation of the maximum amplitude versus the intentional mistuning parameters is plotted in Figure 5.9. As shown in the figure, the average of response amplitude can be significantly reduced, depending on values of τ and ϕ.

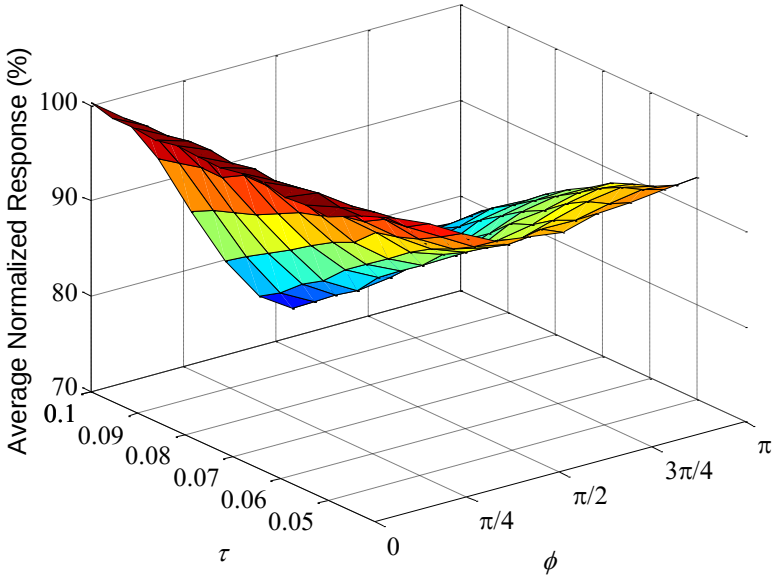

Figure 5.9 Bladed disk response reductions with respect to intentional mistuning parameters.

5.4.2. Formulation of Design Optimization of Bladed Disk with Intentional Mistuning

The goal here is to find the optimal intentional mistuning parameters, τ and ϕ, to minimize the total change of blade normal stiffness while achieving the reliability of bladed disk on vibration response. The design optimization can then be defined as

$$\text{Find } \tau \text{ and } \phi \text{ to minimize } f(\tau,\phi)=\sqrt{\Delta k_{b,1}^2+\Delta k_{b,2}^2+\ldots+\Delta k_{b,N_b}^2} \tag{5.23}$$

$$\text{which is subject to } P_F^{\text{worst}}=P\left[\left|X\right|_{\max}^{\text{worst}}-\left|X\right|_{\text{allow}}\right]\le P_F^{\text{target}},\ \tau^L\le\tau\le\tau^U,\ \phi^L\le\phi\le\phi^U$$

In Equation (5.23), $f(\tau,\phi)$ quantifies the total design modification; P_F^{worst} is the worst-case probability of failure; P_F^{target} is the target or desired probability of failure. Therefore, the design optimization is now cast into a formulation of finding the minimum stiffness change to yield a desired reliability.

5.4.3. Sensitivity Analysis for Design Optimization Computation

The objective function in Equation (5.23) can be re-written in terms of τ and ϕ as

$$\overline{f}(\tau,\phi)=\sqrt{\sum_{i=1}^{N_b}\tau^2\sin^2\left\{\frac{(i-1)\phi}{N_b}\right\}}\,. \tag{5.24}$$

As the objective function and probabilistic constraints in Equation (5.23) are continuous functions of τ and ϕ, gradient-based design optimization can be carried-out. The greatest advantage of using the gradient-based method is efficient rate of convergence can be guaranteed. In order to proceed, calculation of sensitivities of objective function and probabilistic constraints with respect to intentional mistuning parameters that are design variables is needed (Yoo *et al*. 2014). The sensitivity of the objective function in Equation (5.24) with respect to τ and ϕ can be derived, based on that they are independent variables, as

$$\frac{\partial\overline{f}}{\partial\tau}=\sqrt{\sum_{i=1}^{N_b}\sin^2\left\{\frac{(i-1)\phi}{N_b}\right\}}$$

$$\frac{\partial\overline{f}}{\partial\phi}=\frac{\tau\sum_{i=1}^{N_b}\left(\frac{i-1}{N_b}\right)\sin\left\{\frac{2(i-1)\phi}{N_b}\right\}}{2\sqrt{\sum_{i=1}^{N_b}\sin^2\left\{\frac{(i-1)\phi}{N_b}\right\}}} \tag{5.25a, b}$$

The sensitivity of the worst-case probability of failure in Equation (5.23) with respect to τ and ϕ can be calculated using the finite difference method as

$$\frac{\partial P_F^{\text{worst}}}{\partial\tau}\cong\frac{\Delta P_F^{\text{worst}}}{\Delta\tau}=\frac{P_F^{\text{worst}'}-P_F^{\text{worst}}}{\tau'-\tau}$$

$$\frac{\partial P_F^{\text{worst}}}{\partial \phi} \cong \frac{\Delta P_F^{\text{worst}}}{\Delta \phi} = \frac{P_F^{\text{worst}'} - P_F^{\text{worst}}}{\phi' - \phi} \tag{5.26a, b}$$

To expedite the calculation and take advantage of the explicit relations between the structural modal properties (i.e., the natural frequencies of vibration modes) and the vibratory responses, the sensitivity can be actually derived as

$$\frac{\partial P_F^{\text{worst}}}{\partial \tau} = \left(\frac{\partial P_F^{\text{worst}}}{\partial \mathbf{\Lambda}} \frac{\partial \mathbf{\Lambda}}{\partial \mathbf{K}} + \frac{\partial P_F^{\text{worst}}}{\partial \mathbf{\Phi}} \frac{\partial \mathbf{\Phi}}{\partial \mathbf{K}} \right) \frac{\partial \mathbf{K}}{\partial \tau}$$

$$\frac{\partial P_F^{\text{worst}}}{\partial \phi} = \left(\frac{\partial P_F^{\text{worst}}}{\partial \mathbf{\Lambda}} \frac{\partial \mathbf{\Lambda}}{\partial \mathbf{K}} + \frac{\partial P_F^{\text{worst}}}{\partial \mathbf{\Phi}} \frac{\partial \mathbf{\Phi}}{\partial \mathbf{K}} \right) \frac{\partial \mathbf{K}}{\partial \phi} \tag{5.27a, b}$$

where $\mathbf{\Lambda} = \text{diag}\left[\omega_{n,i}^2 \right]$ is the diagonal matrix of the squares of natural frequencies and $\mathbf{\Phi}$ is the modal matrix solved from Equation (5.4). Here $\frac{\partial \mathbf{K}}{\partial \tau}$ and $\frac{\partial \mathbf{K}}{\partial \phi}$ can be easily calculated as

$$\frac{\partial k_{b_{ii}}}{\partial \tau} = \overline{k_b} \sin\left\{ \frac{(i-1)\phi}{N_b} \right\}, \qquad \frac{\partial k_{b_{ii}}}{\partial \phi} = \tau \overline{k_b} \frac{(i-1)}{N_b} \cos\left\{ \frac{(i-1)\phi}{N_b} \right\}, \qquad \frac{\partial k_{b_{jk}}}{\partial \tau} = \frac{\partial k_{b_{jk}}}{\partial \phi} = 0 \tag{5.28a-c}$$

As suggested by Equation (5.26), calculating sensitivity of the worst-case probability of failure with respect to τ and ϕ requires solving eigenvalue problem of the bladed disk system multiple times. In this study, single-degree-of-freedom per blade model is used in the surrogate model, thus solving the eigenvalue problem is not computationally demanding. In future when the approach is extended for more complicated bladed disk model with many DOFs, the computational cost for a single run will be high. Here eigenvalue perturbation is introduced into the analysis to realize efficient analysis based on Equation (5.27). In particular, a perturbation algorithm that is suitable for repeated or closely spaced eigenvalues is adopted (Tang and Wang 2003). The essential idea is to calculate the perturbation of the eigenvalues and eigenvectors by separately calculating the eigenvalue problem of the reduced system that corresponds to each set of repeated eigenvalues.

Additionally, the distribution of the worst-case response amplitude is usually Gaussian, which is based on Central Limit Theorem (Rice 2007). The sensitivity of the worst-case probability of failure with respect to eigenvalues and eigenvectors in Equation (5.27) can thus be further derived for the case when the worst-case response amplitude is normally distributed, which is presented in Appendix.

5.5. Case Studies

In this section, the proposed method is applied to two distinct sets of weakly-coupled bladed disks in the presence of uncertainties. The nominal structure for both bladed disks is identical, which is illustrated in Figure 5.1(b) (Choi *et al*. 2003; Beirow *et al*. 2014), where $\overline{k_b}$ and $\overline{k_c}$ are the nominal blade stiffness and coupling stiffness, respectively. The detailed properties are listed in Table 5.1. The first set of bladed disks contains random uncertainty in its blades only, while the second set of bladed disk contains not only random uncertainty in its blades but also interval uncertainty in its couplings. The nominal structure is certainly weakly-coupled as suggested by low value of nominal coupling ratio $\left(\overline{k_c} / \overline{k_b}\right)$ in Table 5.1.

Table 5.1 Properties of the nominal bladed disk

Number of blades (N_b)	12
Engine order (d)	2
Excitation frequency (ω)	$(5900:1:6900)$ Hz
Damping Ratio $\left(\zeta_i\right)$	0.001
Blade mass (m_b)	0.0114 kg
Nominal blade stiffness ($\overline{k_b}$)	430300 N/m
Maximum response of nominal structure	0.001107 m
Allowed response ($\left\|X\right\|_{\text{allow}}$)	0.001250 m
Random uncertainty (COV)	1 %
Nominal Coupling Ratio ($\overline{k_c} / \overline{k_b}$)	5 %

5.5.1 Reliability Analysis of the Original Bladed Disk without Intentional Mistuning

Without loss of generality, both bladed disks are assumed to be subjected to the 2nd engine order excitation, i.e., $d = 2$ in Equation (5.3b). The maximum response amplitude of the nominal structure

over all excitation frequencies is obtained to be 0.001107 based on Section 5.2, which is less than the allowed amplitude by a wide margin. Thus, it can be decided that performance of the nominal is satisfactory without uncertainties.

Responses become dramatically different when uncertainties are present. For the first bladed disk, the random mistuning of its blades is normally distributed, and the coefficient of variation (COV) is 1% for all of their distributions. The reliability can be calculated using the Monte Carlo simulation based on Equations (5.20) and (5.21), and is found to be 37.7%.

For the second bladed disk, interval analysis is required first due to the presence of interval uncertainty, and the bounds of the interval coupling stiffness between 12 blades are all $\pm 10\%$. During the interval analysis, the worst-case amplitude is obtained based on the method presented in Section 5.3.2. The result of the worst-case amplitude search is shown in Figure 5.10, and the worst-case combination of interval coupling stiffness is shown in Figure 5.11. In Figure 5.10, the proposed M-H based method converges to the worst-case amplitude within three hundred iterations, and the response amplitude at the worst-case is about 50.0% greater than the nominal response. The worst-case reliability is then calculated to be 14.6% using Monte Carlo simulation. In both bladed disks, severe amplifications on their maximum responses are present, due to the presence of uncertainties.

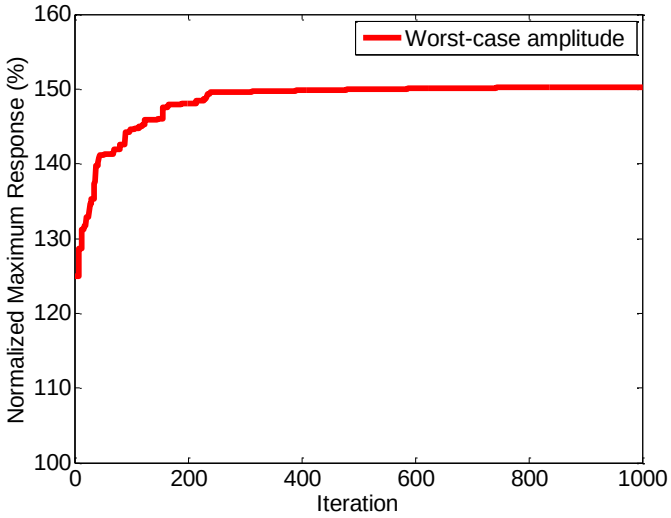

Figure 5.10 Worst-case amplitude search for bladed disk with 12 blades with random and interval uncertainties.

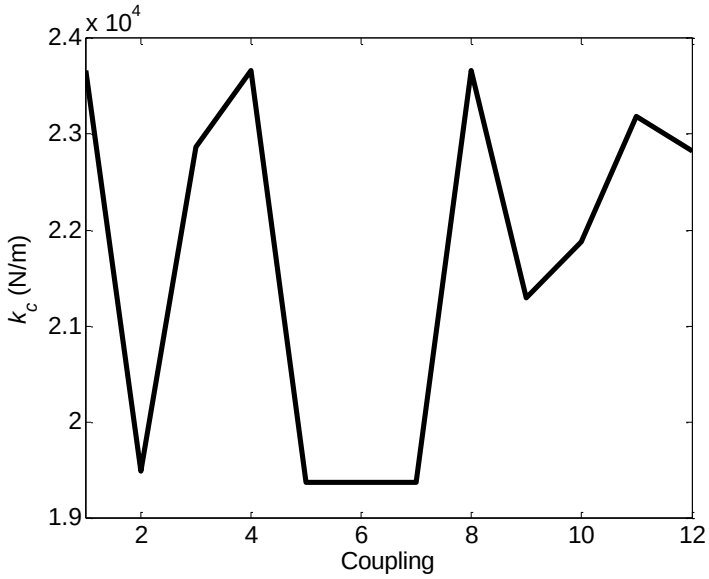

Figure 5.11 Worst-case combination of interval coupling stiffness for bladed disk with 12 blades with random and interval uncertainties.

5.5.2 Optimal Design of Intentional Mistuning to Satisfy Target Reliability

Obviously, reliabilities of the original bladed disks with uncertainties (37.7% and 14.6%) are not satisfactory. The reliability can be enhanced by applying the intentional mistuning technique. The two sets of bladed disks with uncertainties analyzed in Section 5.1 are considered again, and the target reliability is set to be 97.725%, i.e., to achieve a 2-sigma design. The goal is to identify the optimal design of intentional mistuning for the target reliability with the minimized amount of design modification.

As indicated in Section 5.4.2, for the first set of bladed disk with random blade mistuning only, the following problem is solved,

$$\text{Find} \quad \tau \quad \text{and} \quad \phi \quad \text{to minimize} \quad f(\tau,\phi) = \sqrt{\Delta k_{b,1}^2 + \Delta k_{b,2}^2 + ... + \Delta k_{b,N_b}^2} \tag{5.29}$$

$$\text{which is subject to} \quad P_F = P\left[\left|X\right|_{\max} - 0.001250\right] \le 2.275\%, \quad 0 \le \tau \le 0.10\,, \quad 0 \le \phi \le 360^\circ$$

Here the probability of failure only involves the random uncertainty. The maximum percentage change of the nominal blade stiffness is selected as 10%. Similarly, the design optimization problem for the second bladed disk can be formulated as

$$\text{Find } \tau \text{ and } \phi \text{ to minimize } f(\tau,\phi)=\sqrt{\Delta k_{b,1}^2+\Delta k_{b,2}^2+...+\Delta k_{b,N_b}^2} \tag{5.30}$$

$$\text{which is subject to } P_F^{\text{worst}}=P\left[|X|_{\max}^{\text{worst}}-0.001250\right]\le 2.275\%,\quad 0\le\tau\le 0.10\,,\quad 0\le\phi\le 360^\circ$$

The constraint on probability of failure shown in Equation (5.30) is different from that in Equation (5.29) as it requires calculating the worst-case probability of failure.

Equations (5.29) and (5.30) can be efficiently solved by employing the gradient-based design optimization outlined in Section 5.4.3. The design search history for the first and the second bladed disks are listed in Tables 5.2 and 5.3, respectively. It should be noted that worst-case amplitude search is required at every search iteration step. As shown in Tables 5.2 and 5.3, the optimal designs of intentional mistuning can be efficiently obtained for the first and second bladed disks within 7 and 5 iterations, respectively. Despite dramatic improvements on the reliabilities of bladed disks, the total amounts of required design modification (11 to 13%) are affordable. It is worth noting that interval uncertainty in coupling stiffness indeed affects considerably the reliability of a bladed disk, which is well indicated by the difference in reliabilities of the bladed disks at their initial designs and the difference in required amounts of design modification for their optimal designs (Tables 5.2 and 5.3). The spatial distributions of nominal blade stiffness values before and after the introduction of intentional mistunings are compared in Figure 5.12.

Table 5.2 Design search history for bladed disk with random uncertainty only

	τ	ϕ	Design Modification (%)	Reliability (%)
0	0.0000	0.0000	0.00	37.7
1	0.0500	3.1416	12.25	72.8
2	0.0762	3.1630	18.60	94.4
3	0.0835	3.3309	19.86	97.9
4	0.0746	3.5715	17.17	97.9
5	0.0569	4.4404	12.98	99.0
6	0.0435	4.8614	10.37	95.9
7	**0.0464**	**4.9011**	**11.11**	**97.7**

Table 5.3 Design search history for bladed disk with both random and interval uncertainties

	τ	ϕ	Design Modification (%)	Reliability (%)
0	0.0000	0.0000	0.00	14.6
1	0.0500	3.1416	12.25	43.4
2	0.0899	3.1928	21.85	92.3
3	0.0932	3.4582	21.76	97.5
4	0.0494	4.9824	11.92	96.5
5	**0.0511**	**5.0205**	**12.38**	**97.7**

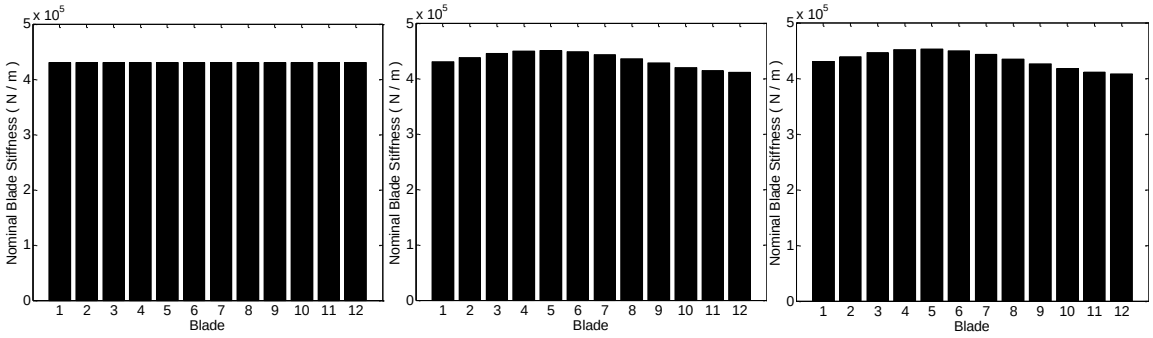

Figure 5.12 Nominal blade stiffness. (a) Before intentional mistuning is introduced; (b) With intentional mistuning design under random uncertainty only; (c) With intentional mistuning design under both random and interval uncertainties.

One advantage of the proposed method is that further modification of intentional mistuning parameters can be facilitated in case when the amount of design modification exceeds the tolerable amount. For instance, consider the tolerable total amount of design modification for the second bladed disk with both random and interval uncertainties is set as 10.50%. In that case, the initial optimal design of intentional mistuning which yields the amount of design modification as 12.38% is considered unacceptable because it exceeds the tolerable total amount. It can be either changed to a different pattern of intentional mistuning and the optimization is re-performed, or, the formulation of the optimization problem can be changed into the following

$$\text{Find} \quad \tau \quad \text{and} \quad \phi \quad \text{to minimize} \quad P_F^{\text{worst}} = P\left[\left|X\right|_{\max}^{\text{worst}} - 0.001250\right] \tag{5.31}$$

which is subject to $f(\tau,\phi)=\sqrt{\Delta k_{b,1}^2+\Delta k_{b,2}^2+...+\Delta k_{b,N_b}^2}\le 10.50\%$, $0\le\tau\le 0.10$, $0\le\phi\le 360°$

This formulation yields an alternative design objective. That is, recognizing the fact that under the pre-specified intentionally mistuning pattern and the desired reliability, an optimal design will exceed the tolerable total amount of design modification, the optimization problem is revised into one that finds the best reliability that can be achieved under the constraint of tolerable total amount of design modification. In such analysis, the gradient-based design optimization can be carried-out again to solve Equation (5.31) by directly using sensitivities derived in Section 5.4.2. The search history and the result of this alternative design optimization are listed in Table 5.4, where it is shown that intentional mistuning parameters satisfying the design modification constraint can be efficiently obtained and the best reliability that can be achieved is 91.5%.

Table 5.4 Design search history for alternative design optimization with adjusted tolerable amount of design modification

	τ	ϕ	Design Modification (%)	Reliability (%)
0	0.0511	5.0205	12.38	97.7
1	**0.0433**	**5.0307**	10.50	91.5

5.6. Conclusions

A new computational framework is developed to achieve reliability-oriented robust design for bladed disks with the mixture of random and interval uncertainties. The interval and random uncertainties are analyzed sequentially through identifying the worst-case response and its distribution, respectively. A Metropolis-Hastings based algorithm is adopted that can find the worst-case response with high efficiency and accuracy. Reliability can then be accurately calculated under the worst-case condition using Monte Carlo simulation. In order to enhance the reliability, spatially harmonic intentional mistuning is introduced to the nominal design of bladed disks, and gradient-based method is formulated to efficiently identify the optimal design. Case studies demonstrate that interval uncertainty indeed affects considerably the

reliability of bladed disk. Meanwhile, a moderate level of design modification can enhance remarkably the reliabilities of bladed disks. In case the required design modification exceeds the tolerable total amount, further adjustment can be facilitated to maximize the reliability for the given tolerable design modification.

Appendix

Assuming the maximum response amplitude is normally distributed, P_F^{worst} can be written as

$$P_F^{\text{worst}} = P\left[\left(\left|X\right|_{\max}^{\text{n,worst}} - \left|\text{X}\right|_{\text{allow}}\right) > 0\right] = 1 - P\left[\left(\left|X\right|_{\max}^{\text{n,worst}} - \left|\text{X}\right|_{\text{allow}}\right) < 0\right] = 1 - F_{\left|X\right|_{\max}^{\text{n,worst}}}\left(\left|\text{X}\right|_{\text{allow}}\right) \tag{5.A1}$$

where $\left|X\right|_{\max}^{\text{n,worst}}$ denotes normally distributed $\left|X\right|_{\max}^{\text{worst}}$, and $F_{\left|X\right|_{\max}^{\text{n,worst}}}\left(\left|\text{X}\right|_{\text{allow}}\right)$ is cumulative distribution function (CDF) of $\left|X\right|_{\max}^{\text{n,worst}}$ evaluated at $\left|\text{X}\right|_{\text{allow}}$. $F_{\left|X\right|_{\max}^{\text{n,worst}}}\left(\left|\text{X}\right|_{\text{allow}}\right)$ in Equation (AII.1) can be transformed to standard normal space based on *Rosenblatt transformation* (Halder and Mahadevan, 2000) as

$$\Phi\left(\left|\text{U}\right|_{\text{allow}}\right) = F_{\left|X\right|_{\max}^{\text{n,worst}}}\left(\left|\text{X}\right|_{\text{allow}}\right) \tag{5.A2}$$

where $\left|\text{U}\right|_{\text{allow}}$ is

$$\left|\text{U}\right|_{\text{allow}} = \Phi^{-1}\left(F_{\left|X\right|_{\max}^{\text{n,worst}}}\left(\left|\text{X}\right|_{\text{allow}}\right)\right) \tag{5.A3}$$

Based on that $\left|X\right|_{\max}^{\text{n,worst}}$ is normally distributed, $\left|\text{U}\right|_{\text{allow}}$ can be derived as

$$\left|\text{U}\right|_{\text{allow}} = \Phi^{-1}\left(F_{\left|X\right|_{\max}^{\text{n,worst}}}\left(\left|\text{X}\right|_{\text{allow}}\right)\right) = \Phi^{-1}\left(\Phi\left(\frac{\left|\text{X}\right|_{\text{allow}} - \mu_{\left|X\right|_{\max}^{\text{worst}}}}{\sigma_{\left|X\right|_{\max}^{\text{worst}}}}\right)\right) = \frac{\left|\text{X}\right|_{\text{allow}} - \mu_{\left|X\right|_{\max}^{\text{n,worst}}}}{\sigma_{\left|X\right|_{\max}^{\text{n,worst}}}} \tag{5.A4}$$

where $\mu_{|X|_{\max}^{\mathrm{n,worst}}}$ and $\sigma_{|X|_{\max}^{\mathrm{n,worst}}}$ are mean and standard deviation of $|X|_{\max}^{\mathrm{n,worst}}$. $\dfrac{\partial P_F^{\mathrm{worst}}}{\partial \boldsymbol{\Lambda}}$ and $\dfrac{\partial P_F^{\mathrm{worst}}}{\partial \boldsymbol{\Phi}}$ can be further derived as

$$\begin{aligned}\frac{\partial P_F^{\mathrm{worst}}}{\partial \boldsymbol{\Lambda}} &= -\frac{\partial \Phi\left(|\mathrm{U}|_{\mathrm{allow}}\right)}{\partial \boldsymbol{\Lambda}} = -\frac{\Phi\left(|\mathrm{U}|_{\mathrm{allow}}\right)}{\partial |\mathrm{U}|_{\mathrm{allow}}}\frac{\partial |\mathrm{U}|_{\mathrm{allow}}}{\partial \mu_{|X|_{\max}^{\mathrm{n,worst}}}}\frac{\partial \mu_{|X|_{\max}^{\mathrm{n,worst}}}}{\partial \boldsymbol{\Lambda}} - \frac{\Phi\left(|\mathrm{U}|_{\mathrm{allow}}\right)}{\partial |\mathrm{U}|_{\mathrm{allow}}}\frac{\partial |\mathrm{U}|_{\mathrm{allow}}}{\partial \sigma_{|X|_{\max}^{\mathrm{n,worst}}}}\frac{\partial \sigma_{|X|_{\max}^{\mathrm{n,worst}}}}{\partial \boldsymbol{\Lambda}} \\ &= \frac{\phi\left(|\mathrm{U}|_{\mathrm{allow}}\right)}{\sigma_{|X|_{\max}^{\mathrm{n,worst}}}}\left(\frac{\partial \mu_{|X|_{\max}^{\mathrm{n,worst}}}}{\partial \boldsymbol{\Lambda}} + \frac{1}{\sigma_{|X|_{\max}^{\mathrm{n,worst}}}}\frac{\partial \sigma_{|X|_{\max}^{\mathrm{n,worst}}}}{\partial \boldsymbol{\Lambda}}\right)\end{aligned} \tag{5.A5}$$

and similarly

$$\frac{\partial P_F^{\mathrm{worst}}}{\partial \boldsymbol{\Phi}} = \frac{\phi\left(|\mathrm{U}|_{\mathrm{allow}}\right)}{\sigma_{|X|_{\max}^{\mathrm{n,worst}}}}\left(\frac{\partial \mu_{|X|_{\max}^{\mathrm{n,worst}}}}{\partial \boldsymbol{\Phi}} + \frac{1}{\sigma_{|X|_{\max}^{\mathrm{n,worst}}}}\frac{\partial \sigma_{|X|_{\max}^{\mathrm{n,worst}}}}{\partial \boldsymbol{\Phi}}\right) \tag{5.A6}$$

$\dfrac{\partial \mu_{|X|_{\max}^{\mathrm{n,worst}}}}{\partial \boldsymbol{\Lambda}}$, $\dfrac{\partial \sigma_{|X|_{\max}^{\mathrm{n,worst}}}}{\partial \boldsymbol{\Lambda}}$, $\dfrac{\partial \mu_{|X|_{\max}^{\mathrm{n,worst}}}}{\partial \boldsymbol{\Phi}}$, and $\dfrac{\partial \sigma_{|X|_{\max}^{\mathrm{n,worst}}}}{\partial \boldsymbol{\Phi}}$ can be calculated using finite difference method.

Chapter 6. Multi-Objective Optimization of Piezoelectric Circuitry Network for Vibration Suppression of Mistuned Bladed Disks

6.1 Introduction

As explained in Chapter 5, one approach thus is to apply pre-specified, deterministic blade-to-blade difference, referred to as intentional mistuning, to a bladed disk to reduce such near-singularity (Martel *et al.* 2008; Han *et al.* 2011; Yu *et al.* 2011; Beirow *et al.* 2015). This intentional mistuning should be large enough to overcome the aforementioned near-singularity in the eigensolution sensitivity, but insignificant to cause change in the dynamic characteristics of the bladed disk involved. Yoo *et al.* (2016) formulated a reliability-based algorithm to identify the optimal design of intentional mistuning. While the reliability of a bladed disk can be improved with intentional mistuning, it was found unsurprisingly that, under a given level of uncertainties (i.e., random mistuning), higher reliability generally required more significant level of intentional mistuning. Obviously, a bladed disk with significant aperiodicity may not function well. A different approach to reducing vibration localization is through integrating spatially periodic piezoelectric circuitry network without altering the bladed disk itself, which preserves the nominal periodicity. Shunted piezoelectric transducers, e.g., piezoelectric transducers connected with inductances, are embedded onto individual blades to realization mode delocalization. The inductance and the inherent piezoelectric capacitance forms an LC shunt, which converts part of the vibratory energy into electrical energy (Tang and Wang, 2003). Properly selected electrical coupling between individual LC shunts can help propagate the energy throughout the entire system circumferentially, thereby reducing the vibration mode localization as well as the forced vibration localization (Yu *et al*. 2006; Wang and Tang 2009).

Ultimately the reliability and durability of a bladed disk is determined by its forced vibration level to which damping plays a very important role. Qualitatively, large damping reduces both the (nominal) vibration amplitudes in a bladed disk as well as the response variance (i.e., the level of vibration localization) in the presence of mistuning. Bladed disks are generally made of materials with low damping and there

have been on-going efforts on damping augmentation via various mechanisms, one of which is through piezoelectric shunting. It has long been recognized that an embedded piezoelectric transducer shunted with inductance and resistance elements, which forms an RLC circuit and is analogous to a tuned mass absorber. Although piezoelectric transducers are subjected to temperature restriction which limits its usage to cold sections of turbomachinery, a number of studies have demonstrated attractive potential of piezoelectric RLC shunts in augmenting damping for fan blades (Duffy *et al*. 2013; Min *et al.* 2013; Zhou *et al.* 2014).

Both the mode delocalization schemes and the vibration damping schemes utilizing piezoelectric transducers are based upon the two-way energy conversion capability of the transducers. In both types of schemes, the inductances are employed to create local resonances to enhance the energy conversion around the targeted frequency range (e.g., around the bladed disk natural frequencies). Several recent studies have attempted to integrating these two mechanisms into one configuration (Zhang and Wang 2002; Yu and Wang 2007; Yu and Wang 2009), i.e., establishing a circuitry network with both coupling capacitances for delocalization and resistances for damping augmentation, and developed encouraging results. Fundamentally, however, certain circuitry elements play very different roles in these two mechanisms. The mode delocalization scheme does not employ resistance elements, mainly because its design objective is to facilitate energy propagation throughout the entire system for all modes. One may even argue that the resistances would even hinder indirectly such energy propagation. Some damping augmenting schemes focus only on individual blades and do not employ coupling capacitances, while others use coupling capacitances to deal with multi-modal vibration suppression in bladed disks so the coupling capacitance selection criterion is entirely different from that in delocalization schemes.

The goal of this research is to provide both design method and insights to facilitate the simultaneous mode delocalization and vibration damping in bladed disks with random mistuning by using piezoelectric network. We adopt the network topology that consists of identical local LC shunts, identical local

resistances, and identical coupling capacitances. We identify quantitatively the influence of a fundamental parameter, the system-level electro-mechanical coupling of a piezoelectric transducer. In practice, the value of the coupling parameter is determined by the transducer size and by the location of embedment (Gupta *et al*. 2010; Durcane *et al.* 2012). This electro-mechanical coupling parameter reflects the transducer's capability of energy conversion between the mechanical and electrical domains (Triplett and Quinn 2009; Wickenheiser *et al.* 2010), and therefore decides how much energy would be dissipated through resistance elements in terms of vibration damping and how much energy would be propagated throughout the system to reduce vibration localization. The interaction and trade-off between vibration damping and mode delocalization, which are two design objectives, are investigated systematically through a multi-objective optimization analysis. This research yields a tool that can lead to the robust design of piezoelectric network for mistuned bladed disks.

6.2 System Model and Mode Localization Characterization

Configuration of the piezoelectric circuitry network to achieve both mode delocalization and vibration suppression of a bladed disk is shown in Figure 6.1 (Zhang and Wang 2002; Yu and Wang 2009), where each piezoelectric shunt circuit, which consists of piezoelectric transducer (PZT), inductor, and resistor, is integrated onto individual blades. Once vibration energy is converted to electrical energy through PZT, the energy is stored in inductor. Resistor in piezoelectric shunt circuit then dissipates the energy, acting as damper to the system while performing vibration suppressions of blades. By coupling the circuits through capacitive elements to form network, vibration delocalization is achieved by evenly distributing the stored energy to the blades.

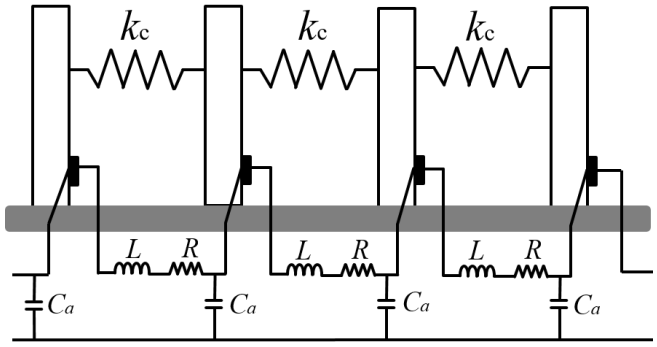

Figure 6.1 Coupled system of bladed disk with piezoelectric circuitry network

The first step to optimize circuit parameters is to derive the equation of motion for the coupled system. The transversal displacement of the *j*-th blade is approximated as (Wang and Tang 2008)

$$w_j(x,t) = \phi(x) q_j(t) \tag{6.1}$$

where ϕ is the first local blade mode without the piezoelectric circuit. The discretized equations of motion for the coupled system can be derived using Hamilton's principle and the assumed mode method, which are

$$m\ddot{q}_j + c\dot{q}_j + kq_j + k_c\left(q_j - q_{j-1}\right) + k_c\left(q_j - q_{j+1}\right) + k_2 Q_j = f_j \tag{6.2a}$$

$$k_2 Q_j + k_1 q_j = V_{aj} \tag{6.2b}$$

where m, c, k, k_c, f_j, k_1, and k_2 are mass, damper, stiffness of blade, coupling stiffness, external force, inverse of the capacitance of piezoelectric patch, and electro-mechanical coupling coefficient, which are given by

$$m = \int_0^{l_b} \rho_b A_b \phi^2 dx + \int_0^{l_b} \rho_p A_p \phi^2 \Delta H dx, \quad g = \int_0^{l_b} c_b \phi^2 dx$$

$$k = \int_0^{l_b} E_b I_b \phi''^2 dx + \int_0^{l_b} E_p I_p \phi''^2 \Delta H dx \quad , \quad k_c = k_s \phi^2\left(x_s\right)$$

$$k_1 = \frac{A_p \beta_{33}}{w_p^2 l_p} \quad , \quad k_2 = \frac{1}{w_p l_p} \int_0^{l_b} F_p h_{31} \phi'' \Delta H dx$$

where q_j is the generalized mechanical displacement of the j-th blade, and V_{aj} and Q_j are the voltage across and charge flowing to the piezoelectric patch attached to the j-th blade. Here $\Delta H = H(x - x_l) - H(x - x_r)$ where H is the Heaviside step function, and x_l and x_r are location of left and right ends of piezoelectric patch. Based on the circuit configuration in Figure 6.1 and *Kirchhoff's current law*, we have

$$Q_a = Q_j - Q_{j+1}$$

$$Q_b = Q_{j-1} - Q_j$$

which, in virtue of the voltage law, lead to

$$V_{aj} = -L\ddot{Q}_j - R\dot{Q}_j - k_a\left(Q_j - Q_{j-1}\right) + k_a\left(Q_{j-1} - Q_j\right) \tag{6.3}$$

where k_a is the inverse of the coupling capacitance. Substituting Equation (6.3) into Equation (6.2b) yields the discretized equations of motion of the electro-mechanically coupled system in Figure 6.1 as

$$m\ddot{q}_j + c\dot{q}_j + kq_j + k_c\left(q_j - q_{j-1}\right) + k_c\left(q_j - q_{j+1}\right) + k_2 Q_j = f_j \tag{6.4a}$$

$$L\ddot{Q}_j + R\dot{Q}_j + k_a\left(Q_j - Q_{j-1}\right) + k_a\left(Q_j - Q_{j+1}\right) + k_1 Q_j + k_2 q_j = 0 \tag{6.4b}$$

For the original bladed disk without piezoelectric circuitry, the equation of motion is given as

$$m\ddot{q}_j + c\dot{q}_j + kq_j + k_c\left(q_j - q_{j-1}\right) + k_c\left(q_j - q_{j+1}\right) = f_j \tag{6.5}$$

In the above derivations, it is assumed that the bladed disk is ideally periodic. On the other hand, uncertainty inevitably exist in blades of the system in its realistic application. As it is the common practice in the localization study, it is assumed in this study that uncertainties of the bladed disk are characterized by the

stiffness variations, and the mass remains unaffected. The stiffness of the *j*-th blade with uncertainty can be then written as

$$k_j = k + \Delta k \tag{6.6}$$

The external load is a time harmonic excitation that consists of a summation of all spatial harmonics with equal weightings. For each spatial harmonic excitation, there is a fixed phase shift between adjacent substructures, but the amplitude of force on all substructures is the same (Duan *et al.* 2016).

$$\begin{bmatrix} f_1 & f_2 & \cdots & f_N \end{bmatrix}^T = \frac{1}{(N/2+1)} \sum_{C=1}^{\frac{N}{2}+1} e^{j\omega t} \left\{ e^{j\varphi_1} \quad e^{j\varphi_2} \quad \cdots \quad e^{j\varphi_1} \quad \cdots \quad e^{j\varphi_N} \right\} \tag{6.7}$$

$$\varphi_i = \frac{2\pi D(i=1)}{N} \quad , \quad C = 0,1,...,N/2+1$$

where φ_i is the phase shift for a given *D*, which is engine order. Localization level of the bladed disk is defined as following (Tang and Wang 2008).

$$S_L = \frac{\sigma_k}{k_c / k} \tag{6.8}$$

where σ_k is the random variation of blade stiffness. Generalized electro-mechanical coupling coefficient of the coupled system is defined as the following (Tang and Wang 2008).

$$\xi = \frac{k_2}{\sqrt{k k_1}} \tag{6.9}$$

Depending on level of localization, bladed disks are subject to various degrees of vibration localization. One of its detrimental effects is localization of vibration modes. Let there be the bladed disk, whose condition is listed in Table 6.1, in the presence of 2.5% of random uncertainty in bladed stiffness, and the corresponding localization level is $0.025/0.025 = 1$. The 1st, 3rd, and 20th vibration modes of the localized system are shown in Figure 6.1, where they are compared with vibration modes of the ideal system. For the perfectly periodic system, all the modes are extended ones that essentially exhibit spatial harmonic patterns,

while vibration occurs only in small number of blades in the localized system. We can quantify localization of each vibration mode based on the definition of modal assurance criterion localization factor (*MACLF*) (Chandrashaker *et al.* 2016), i.e.

$$\mathrm{MACLF}_j = \max_{1\le k\le 2N_b}\left[\frac{\left(\mathbf{v}_j^{\mathrm{T}}\mathbf{b}_k\right)^2}{\left(\mathbf{v}_j^{\mathrm{T}}\mathbf{v}_j\right)\left(\mathbf{b}_k^{\mathrm{T}}\mathbf{b}_k\right)}\right] \tag{6.10}$$

where, in this study, $\mathbf{v}_j$ is the *j*-th vibration mode of the localized system, and $\mathbf{b}_k$ is the *k*-th vibration mode of the perfectly periodic system. Localized modes of rotationally periodic structure often undergo mode swapping that numbering of the modes does not always correspond to the mode numbers of the system with non-localized modes. Thus the maximum *MACLF* value is chosen in Equation (6.10) to pair the correct modes. Owing to its definition, *MACLF* is near 1 for the non-localized system, and it is more close to 0 for the more localized system. *MACLF* for the 1st, 3rd, and 20th modes for the localized system in Figure 6.2 are 0.1603, 0.1700, and 0.2702, respectively. Another detrimental effect of vibration localization is the serious amplification of the forced vibration response under engine-order excitation. The maximum blade tip displacements for the perfectly periodic and the mistuned system are shown in Figure 6.3.

Mode localization and the maximum vibration response can be both alleviated and reduced, respectively, by integrating piezoelectric circuitry network into host structure of the bladed disk. To maximize their effects, vibration suppression and mode delocalization each requires unique tuning of piezoelectric circuit parameters. In this study, methods are individually developed to optimize piezoelectric circuit parameters for each vibration suppression and mode delocalization. The multi-objective optimization is then developed by integrating both methods together.

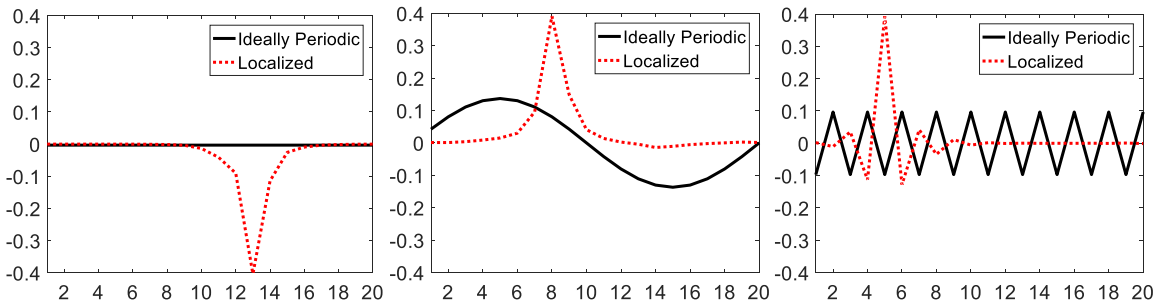

(a) (b) (c)

Figure 6.2 Vibration modes of ideally periodic and localized systems. (a) 1st mode; (b) 3rd mode; and (c) 20th mode

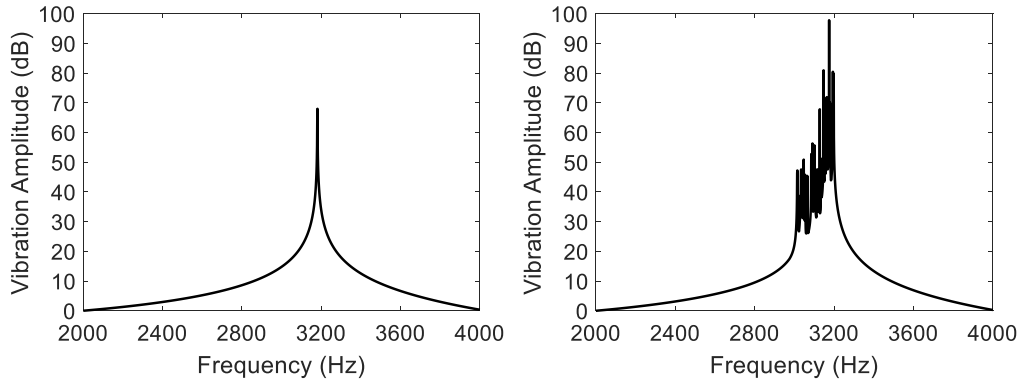

(a) (b)

Figure 6.3 Maximum blade tip displacement under 10th engine order excitation. (a) Perfectly periodic system; (b) Localized system

Table 6.1 Parameters used in computer simulation

$N_b = 20$	$l_b = 0.2253$ m
$l_p = 0.08$ m	$w_b = 0.1001$ m
$w_p = 0.075$ m	$x_l = 0.005$ m
$x_r = 0.085$ m	$h_b = 0.0302$ m
$h_p = 0.008$ m	$\rho_b = 7.8335\times10^3\,\mathrm{kg/m^3}$
$\rho_p = 1.250\times10^3\,\mathrm{kg/m^3}$	$E_b = 1.9818\times10^{11}\,\mathrm{N/m^2}$
$E_p = 7.1246\times10^{10}\,\mathrm{N/m^2}$	$h_{31} = 6.3076\times10^9\,\mathrm{N/C}$
$\beta_{33} = 9.4240\times10^6\,\mathrm{V}$	$R_c = 0.025$

6.3. Optimizations of Piezoelectric Network for Mode Delocalization and Vibration Suppression

6.3.1 Optimization of Piezoelectric Circuit Parameters for Vibration Suppression

Using spatial Fourier transformation, frequency response function of the coupled system under the *j*-th spatial harmonic excitation, which denoted by $\overline{p}_j$, can be derived as (Wang and Tang 2008)

$$\overline{p}_j = \frac{\left(k_1 + 2k_a\left[1-\cos\left(\left(j-1\right)\sigma\right)\right] - \omega^2 L\right) + j\omega R}{\left\{k + 2k_c\left[1-\cos\left(\left(j-1\right)\sigma\right)\right] - \omega^2 m\right\}\left(k_1 + 2k_a\left[1-\cos\left(\left(j-1\right)\sigma\right)\right] + i\omega R - \omega^2 L\right) - k_2^2} \tag{6.11}$$

Based on the reference (Zhang and Wang 2002; Yu and Wang 2007; Wang and Tang 2008), vibration suppression of the coupled system with the optimal piezoelectric network will remain as proportionally effective as the one of the deterministic system even in the presence of uncertainty, hence uncertainty of the system is not considered while analyzing vibration suppression. The optimization problem of piezoelectric circuit parameters for vibration suppression can be formulated as

$$\text{Find } C_a,\ L, \text{ and } R \text{ to minimize } \left|p_j\right|\Big|_{\omega_j=\omega_j^*} \tag{6.12}$$

$$\text{which is subject to } C_a^{\mathrm{L}} \le C_a \le C_a^{\mathrm{U}},\ L^{\mathrm{L}} \le L \le L^{\mathrm{U}},\ R^{\mathrm{L}} \le R \le R^{\mathrm{U}}$$

where

$$\left|p_j\right| = 20\log\left|\overline{p}_j\right| \text{ and } \omega_j^* = \arg\max_{\omega^{\mathrm{L}}\le\omega\le\omega^{\mathrm{U}}}\left(\left|p_j\right|\right)$$

In Equation (6.12), $\left|p_j\right|$ represents $\left|\overline{p}_j\right|$ in decibel unit; $\left|\overline{p}_j\right|$ is the amplitude for vibration response under the *j*-th spatial excitation, as defined in Equation (6.11); ω_j^* is the frequency that maximizes $\left|p_j\right|$; ω^{L} and ω^{U} are lower and upper bounds of the frequency range around the resonant frequency, within which ω_j^* is searched for. The sensitivity-based method is developed to solve Equation (6.12) in this study, and it is integrated into multi-objective optimization for both vibration suppression and mode delocalization,

which is explained in Section 6.4. At every search iteration step, the maximum amplitude within given frequency range is firstly searched, and then it is reduced using the sensitivity information.

Sensitivity of $\left|p_j\right\|_{\omega_j=\omega_j^*}$ with respect to C_a, L, and R can be expanded as

$$\left.\frac{\partial\left|p_j\right|}{\partial C_a}\right|_{\omega=\omega^*}=\frac{20}{\left|\overline{p}_j\right| ln20}\left(\left.\frac{\partial\left|\overline{p}_j\right|}{\partial C_a}\right|_{\omega=\omega^*}\right),\ \left.\frac{\partial\left|p_j\right|}{\partial L}\right|_{\omega=\omega^*}=\frac{20}{\left|\overline{p}_j\right| ln20}\left(\left.\frac{\partial\left|\overline{p}_j\right|}{\partial L}\right|_{\omega=\omega^*}\right),\ \left.\frac{\partial\left|p_j\right|}{\partial R}\right|_{\omega=\omega^*}=\frac{20}{\left|\overline{p}_j\right| ln20}\left(\left.\frac{\partial\left|\overline{p}_j\right|}{\partial R}\right|_{\omega=\omega^*}\right) \tag{6.13}$$

In Equation (6.13), $\partial\left|\overline{p}_j\right|/\partial C_a$, $\partial\left|\overline{p}_j\right|/\partial L$, and $\partial\left|\overline{p}_j\right|/\partial R$ need to be derived. For convenience, some terms for $\overline{p}_j$ in Equation (6.11) can be replaced into simplified terms as

$$S_1=\left[1-\cos\left((j-1)\sigma\right)\right],\ \ S_2=\left\{k_1+2k_aS_1-\omega^2L\right\}, \text{ and } \ S_3=\left(k+2k_cS_1-\omega^2m\right) \tag{6.14}$$

Using the replacing terms defined in Equation (6.14), $\overline{p}_j$ in Equation (6.11) can be rewritten as

$$\overline{p}_j=\frac{S_2+\omega Ri}{S_3\left(S_2+\omega Ri\right)-k_2^2}=\frac{S_2+\omega Ri}{\left(S_3S_2-k_2^2\right)+\omega RS_3i} \tag{6.15}$$

Again, with replacements, Equation (6.15) can be further simplified as

$$\overline{p}_j=\frac{a+bj}{c+dj}=\frac{\left(ac+bd\right)-\left(ad-bc\right)j}{c^2+d^2} \tag{6.16}$$

where

$$a=S_2,\ \ b=\omega R,\ \ c=S_3S_2-k_2^2,\ \ d=\omega RS_3 \tag{6.17}$$

Response amplitude $\left|\overline{p}_j\right|$ can be then obtained as

$$\left|\overline{p}_j\right|=\sqrt{\frac{\left(ac+bd\right)^2+\left(ad-bc\right)^2}{\left(c^2+d^2\right)^2}}=\frac{1}{\left(c^2+d^2\right)}\sqrt{\left(ac+bd\right)^2+\left(ad-bc\right)^2} \tag{6.18}$$

Sensitivity of response amplitude in Equation (6.18) with respect to C_a is derived as

$$\frac{\partial\left|\overline{p}_j\right|}{\partial C_a}=\frac{1}{\left(c^2+d^2\right)}\frac{1}{2\sqrt{\left(ac+bd\right)^2+\left(ad-bc\right)^2}}$$
$$\times\left[2\left(ac+bd\right)\left\{\left(\frac{da}{dC_a}\right)c+a\left(\frac{dc}{dC_a}\right)\right\}+2\left(ad-bc\right)\left\{\left(\frac{da}{dC_a}\right)d-b\left(\frac{dc}{dC_a}\right)\right\}\right] \quad (6.19)$$
$$-\frac{2c}{\left(c^2+d^2\right)^2}\left(\frac{dc}{dC_a}\right)\sqrt{\left(ac+bd\right)^2+\left(ad-bc\right)^2}$$

where

$$\frac{da}{dC_a}=-\frac{2S_1}{\left(C_a\right)^2} \text{ and } \frac{dc}{dC_a}=-\frac{2S_1S_3}{\left(C_a\right)^2}$$

Similarly, derivative of $\left|\overline{p}_j\right|$ with respect to L and R can be derived as

$$\frac{\partial\left|\overline{p}_j\right|}{\partial L}=\frac{1}{\left(c^2+d^2\right)}\frac{1}{2\sqrt{\left(ac+bd\right)^2+\left(ad-bc\right)^2}}$$
$$\times\left[2\left(ac+bd\right)\left\{\left(\frac{da}{dL}\right)c+a\left(\frac{dc}{dL}\right)\right\}+2\left(ad-bc\right)\left\{\left(\frac{da}{dL}\right)d-b\left(\frac{dc}{dL}\right)\right\}\right] \quad (6.20)$$
$$-\frac{2c}{\left(c^2+d^2\right)^2}\left(\frac{dc}{dL}\right)\sqrt{\left(ac+bd\right)^2+\left(ad-bc\right)^2}$$

where

$$\frac{da}{dL}=-\omega^2 \text{ and } \frac{dc}{dC_a}=-S_3\omega^2,$$

and

$$\frac{\partial\left|\overline{p}_j\right|}{\partial R}=\frac{1}{\left(c^2+d^2\right)}\frac{1}{2\sqrt{\left(ac+bd\right)^2+\left(ad-bc\right)^2}}$$
$$\times\left[2\left(ac+bd\right)\left\{\left(\frac{db}{dR}\right)d+b\left(\frac{dd}{dR}\right)\right\}+2\left(ad-bc\right)\left\{(a)\left(\frac{dd}{dR}\right)-\left(\frac{db}{dR}\right)(c)\right\}\right] \quad (6.21)$$
$$-\frac{2d}{\left(c^2+d^2\right)^2}\left(\frac{dd}{dR}\right)\sqrt{\left(ac+bd\right)^2+\left(ad-bc\right)^2}$$

where

$$\frac{db}{dR} = \omega \quad \text{and} \quad \frac{dd}{dR} = S_3\omega$$

Brief numerical example is carried-out in this section to demonstrate the proposed method. The condition of the coupled system is listed in Table 6.1. Consider the initial state of the coupled system for which circuit parameters are not ideally tuned. Vibration suppression of the initial system is shown in Figure 6.4 (a). The proposed sensitivity-based method can be applied to find the optimal circuit parameters. Note that sensitivity of the maximum vibration amplitude with respect to the coupling capacitance is relatively large due to its measurement unit. Hence search space for the coupling capacitance is transformed to the logarithmic space, which can be retrieved back to the original space once its optimal value is obtained. Design search history of optimal circuit parameters is shown in Figure 6.3, where the optimal circuit parameters are obtained within 13 iterations. Sensitivity information at each design search iteration is shown in Table 6.2, in which the one with respect to the resistance is consistently very small, while the one with respect to the inductance remains constantly high. While the proposed optimization method is for multi-objective optimization purpose, optimal circuit parameters have been analytically derived in the references (Zhang and Wang 2002; Yu and Wang 2007), and they are given as

$$C_a^* = \frac{k}{k_1 k_c}, \quad L^* = \frac{m\left\{k_1 + 2k_a\left[1-\cos\left((j-1)\sigma\right)\right]\right\}}{k + 2k_c\left[1-\cos\left((j-1)\sigma\right)\right]}, \quad R^* = \frac{\sqrt{2m\left(k_1 + 2k_a\left[1-\cos\left((j-1)\sigma\right)\right]\right)k_2}}{k + 2k_c\left[1-\cos\left((j-1)\sigma\right)\right]} \tag{6.22}$$

Vibration suppressions by the proposed optimization method and the traditional analytical method are shown in Figures 6.5 (b) and (c), respectively, and they are indeed equally in effect. In Figures 6.5 (b) and (c), both vibration responses are significantly reduced, and the resonant frequencies are also successfully removed.

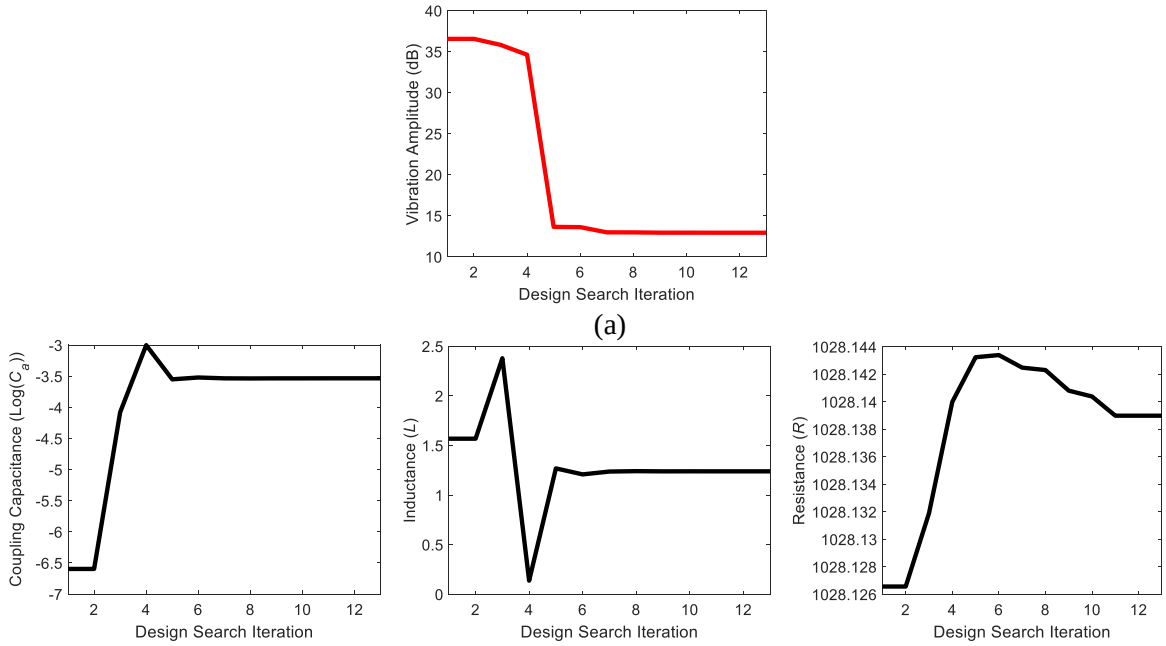

Figure 6.4 Design search history for (a) optimal vibration response; (b) optimal coupling capacitance; (c) optimal inductance; (d) optimal resistance

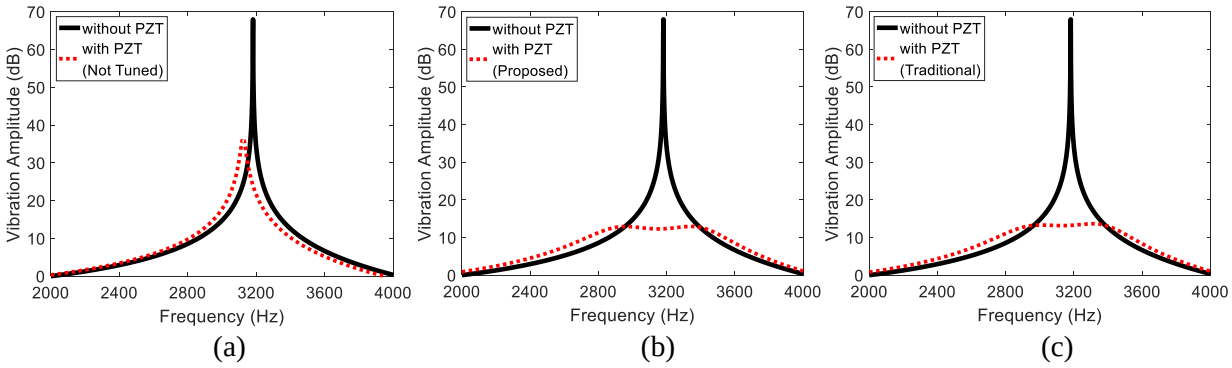

Figure 6.5 Frequency response of coupled system. (a) with initial not tuned circuit parameters; (b) with tuned circuit parameters using the proposed method; (c) with tuned circuit parameters using the traditional method

Table 6.2 Sensitivity information at each design search step

	Iteration						
	1	**2**	**3**	**4**	**5**	**6**	**7**
$\partial\lvert p_j\rvert / \partial \mathrm{Log}(C_a)$	–41.4098	–41.4098	0.1358	–0.0124	0.0705	–0.0755	–0.0766
$\partial\lvert p_j\rvert / \partial L$	–11.4	–11.4	13.2	–13.4	24.8	–22.4	–21.9
$\partial\lvert p_j\rvert / \partial R$	–0.00761	–0.00761	–0.00739	–0.00727	0.00192	–0.00014	0.00021
	Iteration						
	8	**9**	**10**	**11**	**12**	**13**	
$\partial\lvert p_j\rvert / \partial \mathrm{Log}(C_a)$	0.0644	–0.0765	0.0639	–0.0764	–0.0764	–0.0764	
$\partial\lvert p_j\rvert / \partial L$	23.3	–21.8	23.2	–21.8	–21.8	–21.8	
$\partial\lvert p_j\rvert / \partial R$	0.00306	0.00022	0.00310	0.00022	0.00022	0.00022	

6.3.2 Optimization of Piezoelectric Circuit Parameters for Vibration Mode Delocalization

Localization level of each vibration mode of the coupled system can be quantified based on the definition of *MACLF* in Equation (6.10), which is distributed in the presence of uncertainty. Using *Mahalanobis distance* (Webb 2003), we can scalarize distributed *MACLF* for each mode by defining root mean square localization factor (*RMSLF*) as

$$RMSLF_j = \frac{1}{NS}\sqrt{\sum_{k=1}^{NS}\left(1 - MACLF_j^{(k)}\right)^2} \tag{6.23}$$

The more the system is delocalized, the closer *RMSLF* is to 0. Objective function for vibration delocalization can be defined by scalarizing vector of *RMSLF* by using L_p *norm minimization* method (Boyd and Vandenberghe 2004). The optimization problem for vibration delocalization can be formulated as

$$\text{Find } C_a \text{ and } L \text{ to minimize } f^{\mathrm{d}}(C_a, L) = \left\{\sum_{h=1}^{2N_b} w_h^d \left(RMSLF_h\right)^p\right\}^{1/p} \tag{6.24}$$

which is subject to $C_a^{\mathrm{L}} \le C_a \le C_a^{\mathrm{U}}$, $L^{\mathrm{L}} \le L \le L^{\mathrm{U}}$

where w_h^d is the weight of importance assigned for *h*-th vibration mode of the bladed disk, and *P* is the amount of weight applied on distance from the perfect system. If $p=1$ is selected in Equation (6.24), the objective is identical to that of the standard *weighted sum optimization*. If $p=2$ is selected, the objective is formulated as *Euclidean norm* form. If $p=\infty$ is selected, the objective is formulated as *Chebyshev norm*, for which vibration mode with the worst *RMSLF* is only considered. The gradient-based method, which will be integrated into multi-objective optimization, is developed to solve the optimization problem in Equation (6.24).

The objective function in the design search space needs to be firstly identified. The proposed method evaluates objective functions in the given design search space by the sampling-based method. The objective function can be then approximated by the least-squares regression technique (Forrester and Keane 2009). To facilitate the gradient-based optimization method, bi-variate polynomial regression technique is used in this study. The general form of approximated bi-variate polynomial function can be written as

$$\begin{bmatrix} 1 & L_1 & (C_a)_1 & (C_a)_1 L_1 & (C_a)_1 L_1^2 & (C_a)_1^2 L_1 & (C_a)_1^2 L_1^2 & \cdots & (C_a)_1^n L_1^m \\ 1 & L_2 & (C_a)_2 & (C_a)_2 L_2 & (C_a)_2 L_2^2 & (C_a)_2^2 L_2 & (C_a)_2^2 L_2^2 & \cdots & (C_a)_2^n L_2^m \\ 1 & L_3 & (C_a)_3 & (C_a)_3 L_3 & (C_a)_3 L_3^2 & (C_a)_3^2 L_3 & (C_a)_3^2 L_3^2 & \cdots & (C_a)_3^n L_3^m \\ \vdots & \vdots & \vdots & \vdots & \vdots & \vdots & \vdots & & \vdots \\ 1 & L_{ns} & (C_a)_{ns} & (C_a)_{ns} L_{ns} & (C_a)_{ns} L_{ns}^2 & (C_a)_{ns}^2 L_{ns} & (C_a)_{ns}^2 L_{ns}^2 & \cdots & (C_a)_{ns}^n L_{ns}^m \end{bmatrix} \begin{bmatrix} a_0 \\ a_{01} \\ a_{10} \\ a_{11} \\ a_{12} \\ a_{21} \\ a_{22} \\ \vdots \\ a_{nm} \end{bmatrix} = \mathbf{X}\vec{\mathrm{A}} = \begin{bmatrix} \hat{f}_1^{\mathrm{d}} \\ \hat{f}_2^{\mathrm{d}} \\ \hat{f}_3^{\mathrm{d}} \\ \vdots \\ \hat{f}_{ns}^{\mathrm{d}} \end{bmatrix} = \vec{\hat{f}}^{\mathrm{d}} \tag{6.25}$$

where *ns* is number of samples and f^{d} is denoted for surrogate objective function. The coefficients in Equation (6.25) is identified by solving the least-squares optimization problem given as

$$\text{find} \quad \vec{\mathrm{A}} \tag{6.26}$$

$$\text{to minimize } \left\| \overrightarrow{f^{\mathrm{d}}} - \overline{f^{\mathrm{d}}} \right\|_2$$

Once the coefficients for surrogate objective function are determined, the optimization problem in Equation (6.24) can be rewritten as

$$\text{Find } C_a \text{ and } L \tag{6.27}$$

$$\text{to minimize } f^{\mathrm{d}}(C_a, L) = a_0 + a_{01}C_a + a_{10}L + a_{11}C_aL + a_{21}C_a^2 + a_{12}C_aL^2 + a_{22}C_a^2L^2 + \ldots + C_a^nL^m$$

$$\text{which is subject to } C_a^{\mathrm{L}} \le C_a \le C_a^{\mathrm{U}}, \quad L^{\mathrm{L}} \le L \le L^{\mathrm{U}}$$

where sensitivity of surrogate objective function with respect to piezoelectric circuit parameters are derived as

$$\frac{\partial f^{\mathrm{d}}}{\partial C_a} = a_{01} + a_{11}L + 2a_{21}C_a + a_{12}L^2 + 2a_{22}C_aL^2 + \ldots + nC_a^{n-1}L^m, \tag{6.28}$$

$$\frac{\partial f^{\mathrm{d}}}{\partial L} = a_{10} + a_{11}L + 2a_{12}C_aL + 2a_{22}C_a^2L + \ldots + mC_a^nL^{m-1}$$

The optimization problem in Equation (6.27) can be solved using the sensitivity in Equation (6.28).

To demonstrate the proposed method, brief numerical example is carried-out in this section. The simulation condition for a bladed disk is shown in Table 6.1, and design search space is identical to that in which piezoelectric circuit parameters are optimized to maximize vibration suppression. Distribution of *MACLF* for each mode can be firstly calculated for the nominal system. The corresponding *RMSLF* values are shown in Figure 6.4, where there is noticeable variance among *RMSLF*s of different modes, and higher modes tend to be more localized. The next step is to decide objective value for vibration delocalization based on definition in Equation (6.24). In this example, weights are equally distributed to all the existing modes, and *Euclidean norm* $(p = 2)$ is used. In the similar manner, objective values throughout the entire design search space are obtained, which is shown in Figure 6.7. By solving the optimization problem in Equation (6.26), high-fidelity surrogate model for the objective function with high correlation coefficient

of 0.9608 is obtained. Using the sensitivity obtained based on Equation (6.28), the optimization problem in Equation (6.27) can be solved. The design search history is shown in Figure 6.9, where the optimal design is obtained within 12 iterations.

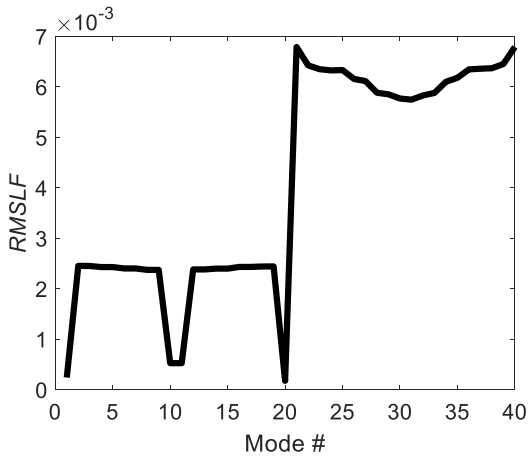

Figure 6.6 Root mean square localization factor (*RMSLF*) for vibration mode

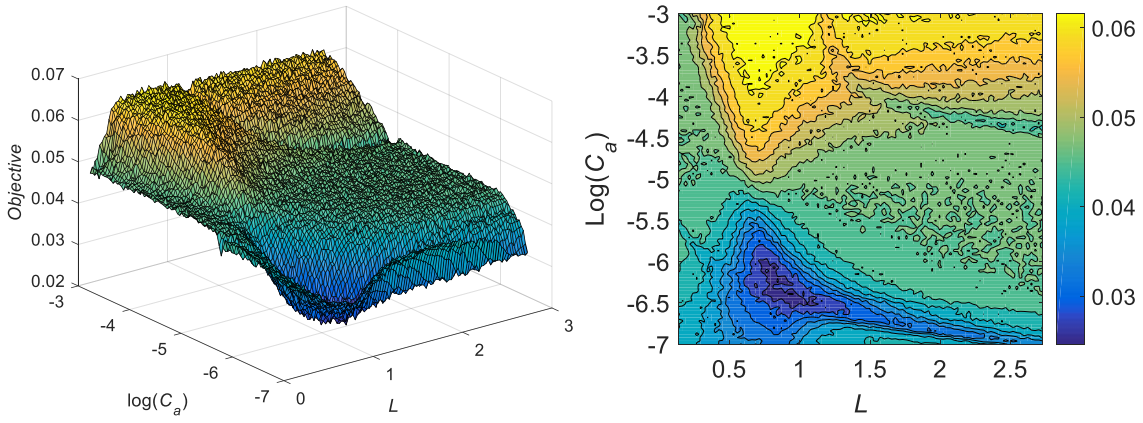

(a) (b)

Figure 6.7 Objective function for vibration delocalization. (a) three-dimensional view; (b) contour view

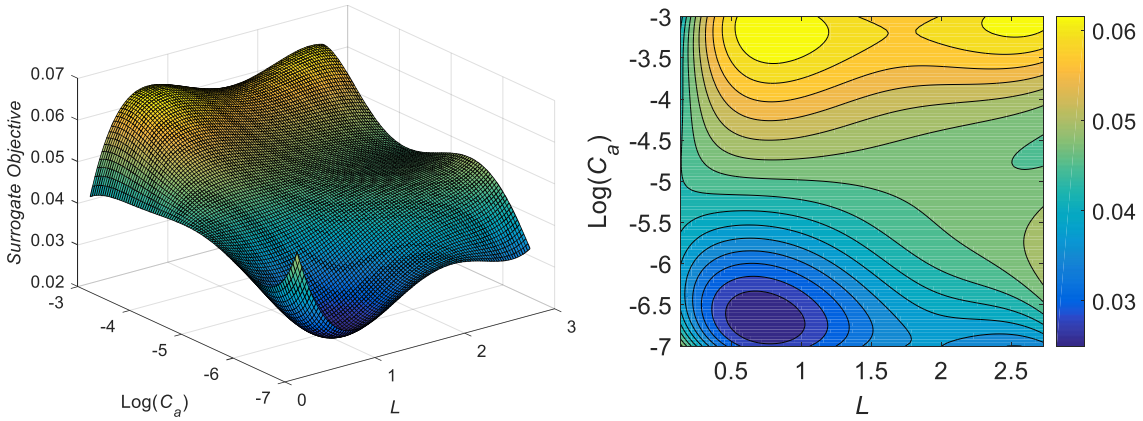

(a) (b)

Figure 6.8 Surrogate model for objective function for vibration delocalization. (a) three-dimensional view; (b) contour view

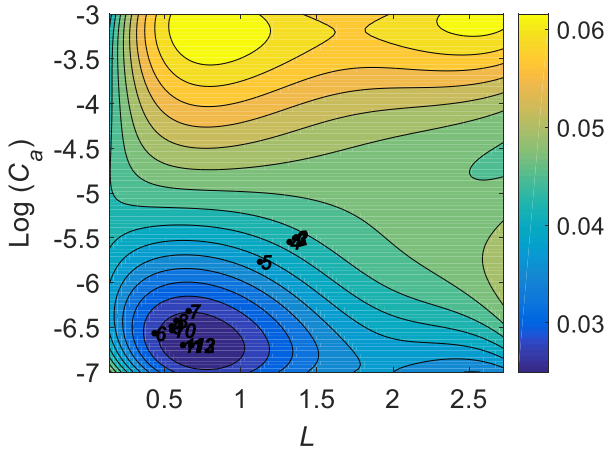

Figure 6.9 Design search history for vibration delocalization optimization

6.4 Multi-Objective Optimization for Vibration Suppression and Delocalization

Optimization methods for vibration suppression and delocalization are individually considered in Section 6.3. In this section, multi-objective optimization is developed to simultaneously consider both mode delocalization and vibration suppression. The most classic weighted sum method is developed in this study. In case when *Pareto optimal front*, which is set of non-dominated solutions, is non-convex, more thorough *Pareto optimal front* can be obtained by further applying such as ε-constraint method (Deb 2005). In the proposed framework, *composite objective* is defined, where vibration suppression and delocalization are defined as sub-objectives with assigned weights, which are decided based on their relative importance

(Collette and Siarry 2013). The multi-objective optimization of piezoelectric circuit parameters for vibration suppression and delocalization is formulated as

$$\text{Find } C_a,\ L \text{ , and } R \text{ to minimize } h = \alpha \mathrm{V}_s + (1-\alpha)\mathrm{V}_d \tag{6.29}$$

$$\text{which is subject to } C_a^{\mathrm{L}} \le C_a \le C_a^{\mathrm{U}},\ L^{\mathrm{L}} \le L \le L^{\mathrm{U}}, \text{ and } R^{\mathrm{L}} \le R \le R^{\mathrm{U}}$$

where

$$\mathrm{V}_s = \frac{|p_j|}{|p_j|^{\min}} \text{ and } \mathrm{V}_d = \frac{f^{\mathrm{d}}}{f^{\mathrm{d,min}}} \tag{6.30}$$

In Equation (6.29), α is weight coefficient; V_s and V_d are normalized sub-objectives for vibration suppression and delocalization, respectively; $|p_j|^{\min}$ and $f^{\mathrm{d,min}}$ are the minimums of vibration suppression and delocalization for a given design search space; Superscripts L and U represent lower and upper bounds of design search space, respectively. In this study, sensitivity-based method is developed to solve the multi-objective optimization problem in Equation (6.29). Sensitivity of the composite objective in Equation (6.29) with respect to C_a can be derived as

$$\frac{\partial h}{\partial C_a} = \alpha \frac{\partial \mathrm{V}_s}{\partial C_a} + (1-\alpha)\frac{\partial \mathrm{V}_d}{\partial C_a} = \alpha \left(\frac{1}{|p_j|^{\min}} \right) \left(\frac{\partial |p_j|}{\partial C_a} \right) + (1-\alpha) \left(\frac{1}{f^{\mathrm{d,min}}} \right) \left(\frac{\partial f^{\mathrm{d}}}{\partial C_a} \right) \tag{6.31}$$

In Equation (6.31), $\partial |p_j| / \partial C_a$ and $\partial f^{\mathrm{d}} / \partial C_a$ are derived in Sections 3. $\partial h / \partial L$ and $\partial h / \partial R$ can be derived in similar manner. Flowchart for the proposed multi-objective optimization method is shown in Figure 6.10, where optimizations for vibration suppression and mode delocalization are parallelly computed, and multi-objective optimization is carried-out after normalizing sub-objectives.

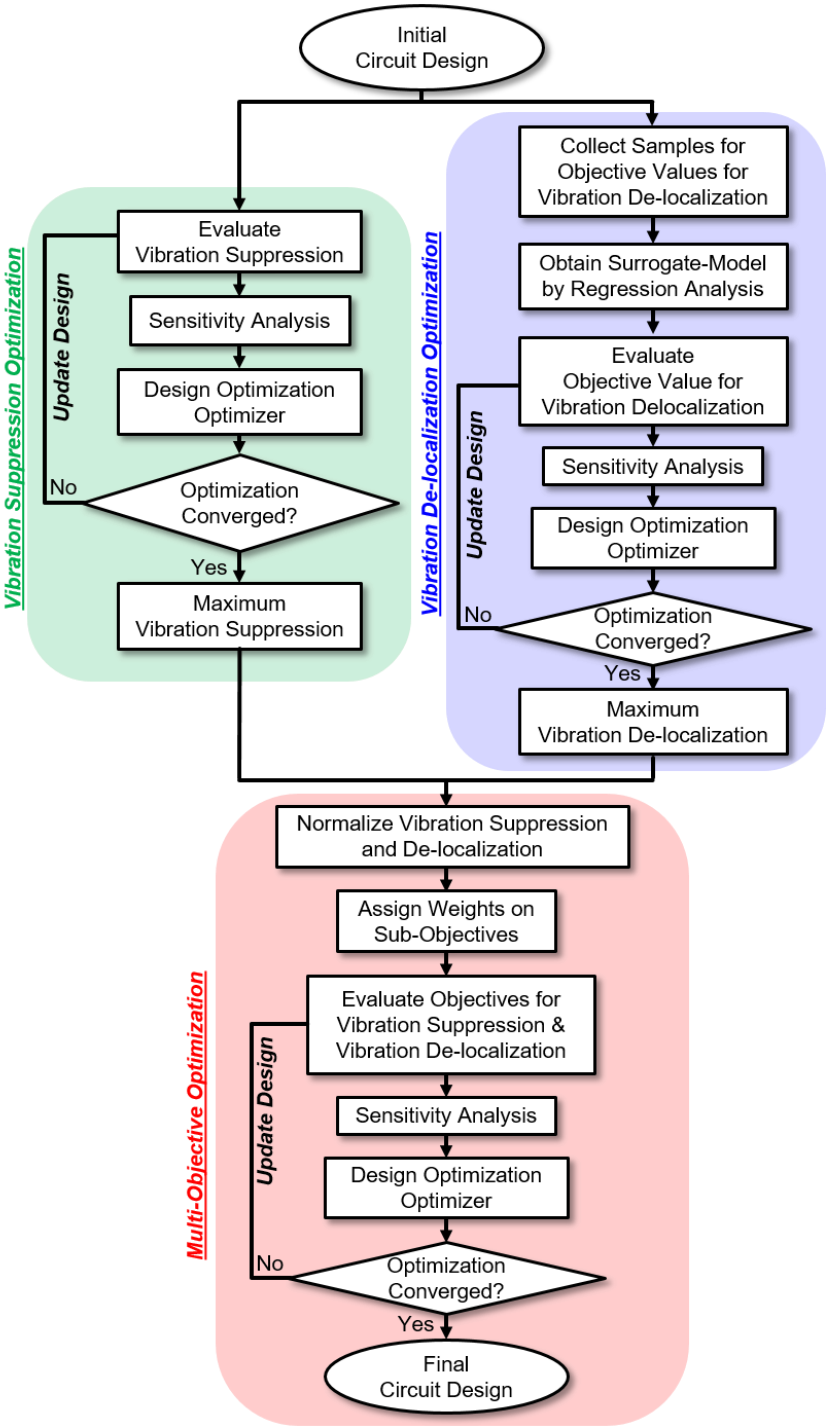

Figure 6.10 Flowchart for sensitivity-based multi-objective optimization of piezoelectric circuit parameters for vibration suppression and mode delocalization

Brief numerical example is carried-out in this section to demonstrate the proposed multi-objective optimization method. The simulation condition is shown in Table 6.1, which is identical to the ones in Section 6.3. The multi-objective optimizations are carried out for different weight coefficients $(\alpha = 0.0, 0.25, 0.5, 0.75, 1)$. The results are shown in Figure 6.11, where it is shown that the proposed method, in overall, can efficiently find optimal piezoelectric circuit parameters. As shown in Figure 6.11, there is the different trade-off between one sub-objective to another for different weight coefficient. When $\alpha = 0$ or $\alpha = 1$, either mode delocalization or vibration suppression is minimized. Meanwhile, the other sub-objective is completely sacrificed. When $\alpha = 0.25$ and $\alpha = 0.75$, the optimization concerns more of either vibration suppression or mode delocalization. When $\alpha = 0.5$, both vibration suppression and mode delocalization are equally concerned. It should be noted that trends of optimization result in terms of α is not linear. To elucidate the trend, *Pareto optimal front* is obtained by applying the proposed method for varying α, and it is shown in Figure 6.12 (Collette and Siarry 2013).

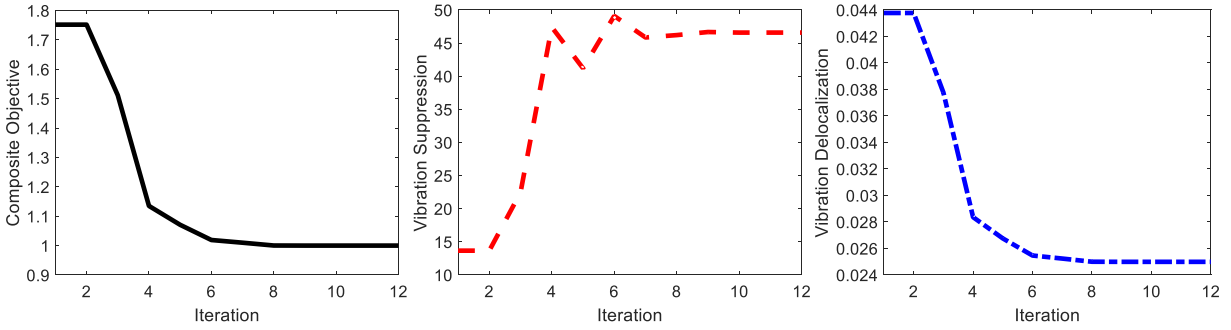

(a)

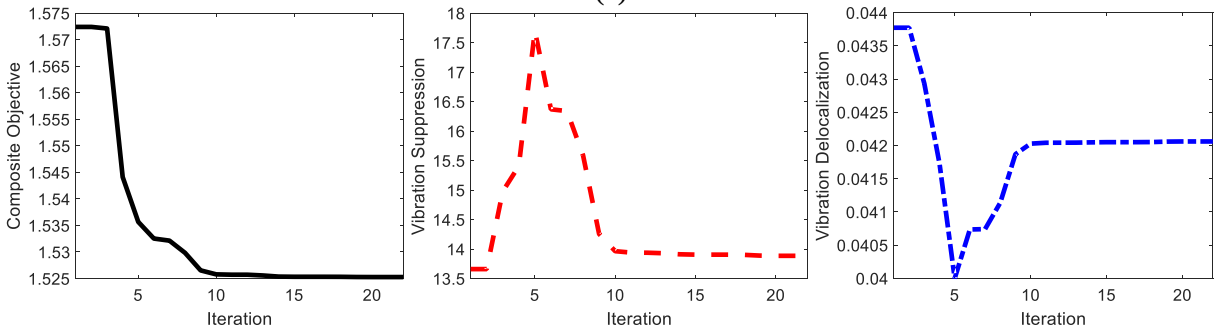

(b)

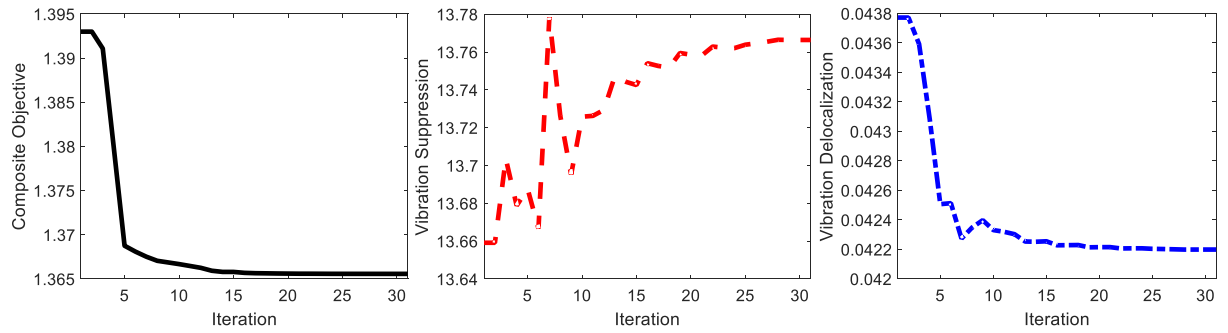

(c)

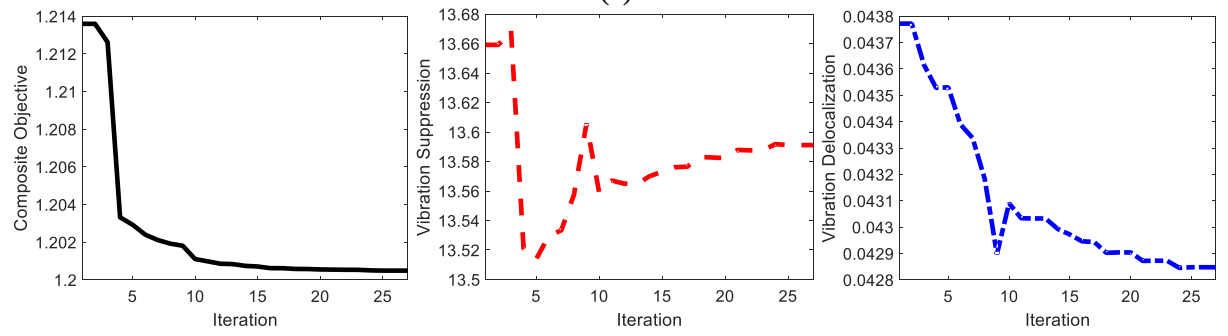

(d)

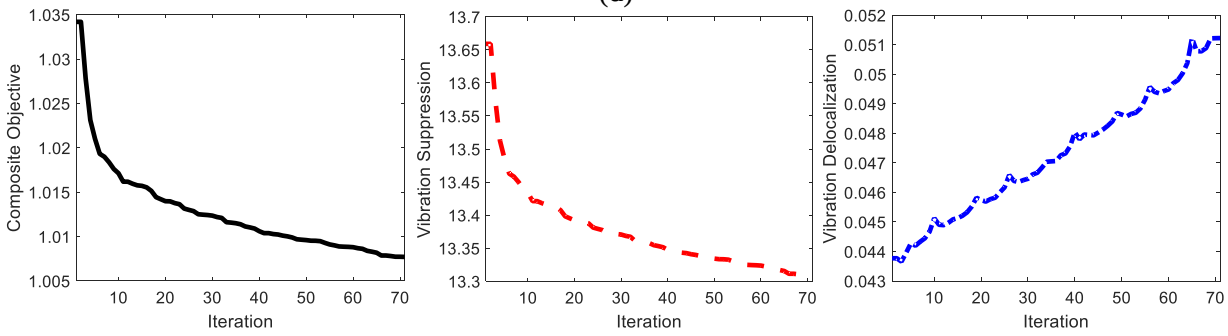

(e)

Figure 6.11 Multi-objective optimization for vibration suppression and delocalization with different weight coefficients. (a) $\alpha = 0$, (b) $\alpha = 0.25$, (c) $\alpha = 0.50$, (d) $\alpha = 0.75$, (e) $\alpha = 1.00$

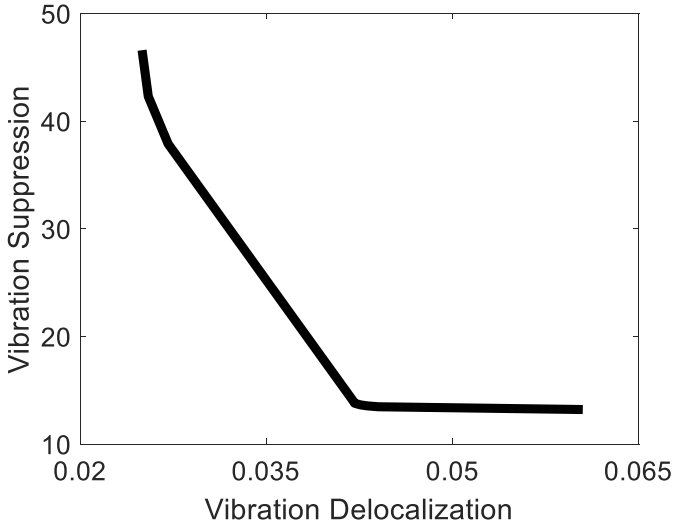

Figure 6.12 *Pareto optimal front* for vibration suppression and delocalization

6.5 Case Studies

6.5.1 Localization Level of Bladed Disk on Vibration Suppression and Delocalization

As introduced in Section 2, localization of overall vibration modes highly depends on localization level of bladed disk (Wang and Tang 2008; Chandrashaker *et al.* 2016). In this section, the proposed multi-objective optimization method is applied to bladed disks with different localization levels. The nominal bladed disk with localization level of 1 is shown in Table 6.1. Since uncertainty effect is not considered during the vibration suppression analysis, level of localization is expected to mostly affect vibration delocalization. The surrogate models for objectives of vibration delocalization for different localization levels of 0.2, 0.5, 1, 2, 3, and 6 are shown in Figure 6.13, where it is shown that localization level indeed much affects performance of vibration delocalization. As the localization level gets higher, average objective value for vibration delocalization considerably increases. Using the proposed method, *Pareto optimal fronts* for different localization levels are obtained as shown in Figure 6.14, where it is observed that *pareto optimal front* significantly declines with higher localization level. According to Figure 6.14, the effect of piezoelectric treatment is more dramatic when localization level is high, although it is more difficult to meet the desired state.

When localization level is low, corner point on *Pareto optimal front* should be the most reasonable choice, since beyond that point mode delocalization hardly improves while vibration suppression is much sacrificed. When localization level is high, corner point on *Pareto optimal front* is still the good choice, on the other hand, there is the option to improve mode delocalization as trade-off from vibration suppression.

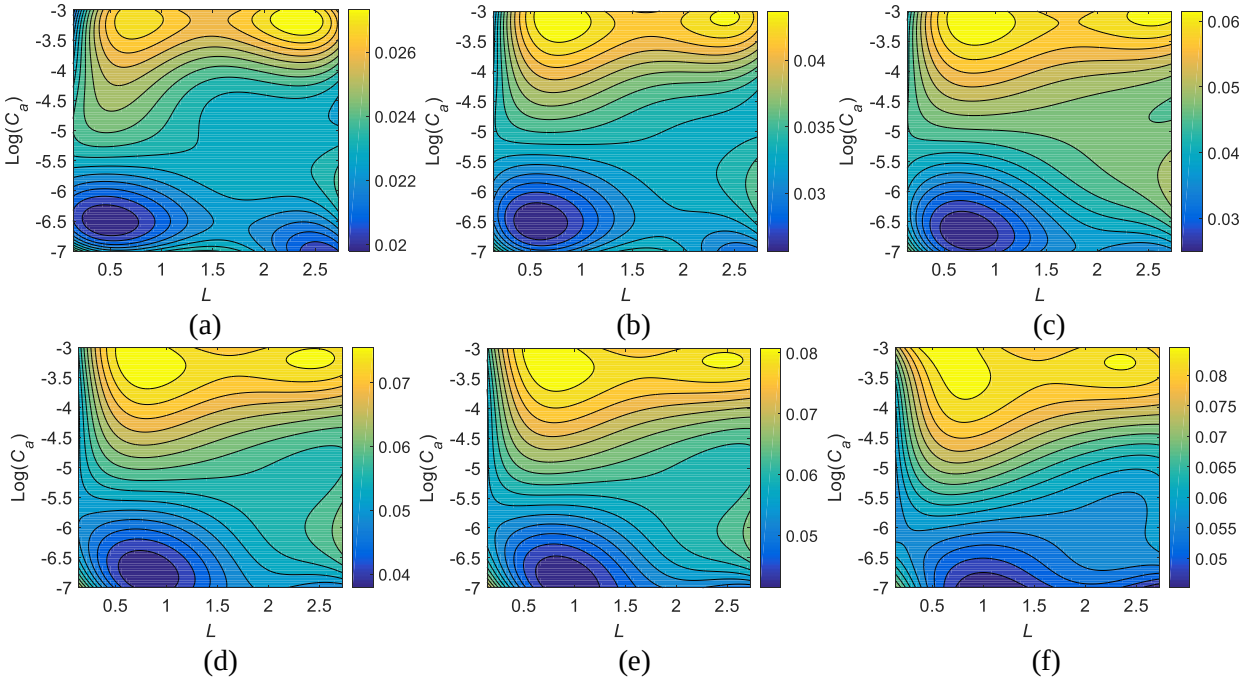

Figure 6.13 Surrogate models for objective function of vibration delocalization of bladed disk with different localization level. Localization level of (a) 0.2, (b) 0.5, (c) 1.0, (d) 2.0, (e) 4.0, and (f) 6.0

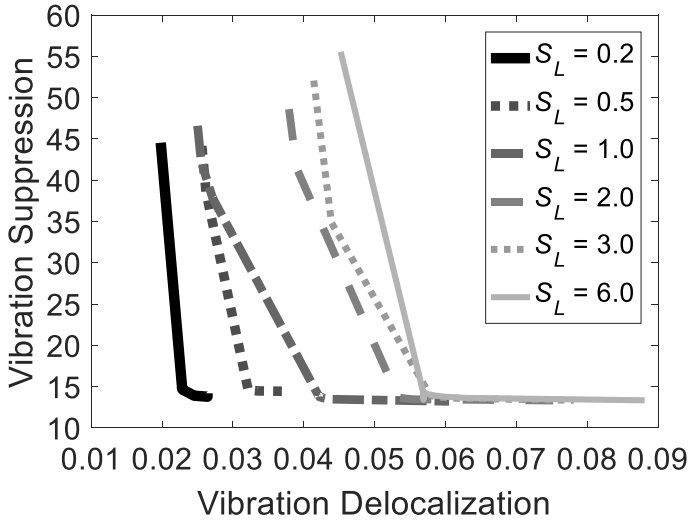

Figure 6.14 *Pareto optimal fronts* for different levels of localization (S_L)

6.5.2 Effect of Electro-Mechanical Coupling of PZT on Vibration Suppression and Delocalization of Bladed Disk

Depending on level of localization of the bladed disk, it is not always possible to meet desired state of bladed disk even with optimal tuning of piezoelectric circuit parameters. In such circumstance, the system needs more fundamental improvement, which is to increase electro-mechanical coupling, and it can be done by increasing the size of PZT, or by using PZT with better performance, or placing PZT at the optimal location. Electro-mechanical coupling of the nominal bladed disk is approximately 0.2, and condition of the nominal bladed disk is shown in Table 6.1. In this section, effect of electro-mechanical coupling on performances of vibration suppression and delocalization is further explored. For different electro-mechanical couplings of 0.025, 0.05, 0.075, 0.1, 0.2, and 0.4, and 0.5, surrogate models of objective functions for mode delocalization and performances of vibration suppression are shown in Figures 6.15 and 16, respectively. It is observed in Figures 6.15 and 6.16 that as electro-mechanical coupling increases, average objective values for mode delocalization decreases and vibration responses can be more suppressed. Using the proposed method, *Pareto optimal fronts* for different electro-mechanical couplings are obtained and are shown in Figure 6.17, where there is clear trend that performances of mode delocalization and vibration suppression significantly improve with higher electro-mechanical coupling.

When electro-mechanical coupling is low $(\xi = 0.025, 0.050, 0.075)$, corner point of *Pareto optimal front* should be the most sensible choice, since beyond that point vibration delocalization can be seldom improved while vibration suppression is much given-up. Also, when reliability and robustness of the system are both low, it is more crucial to recover system reliability first. When electro-mechanical coupling is high $(\xi = 0.4, 0.5)$, corner point of *Pareto optimal front* can be sill decent candidate, on the other hand, there are options to achieve complete vibration delocalization while sacrificing vibration suppression to some degrees, since the maximum vibration is well-suppressed over the entire *Pareto optimal front*.

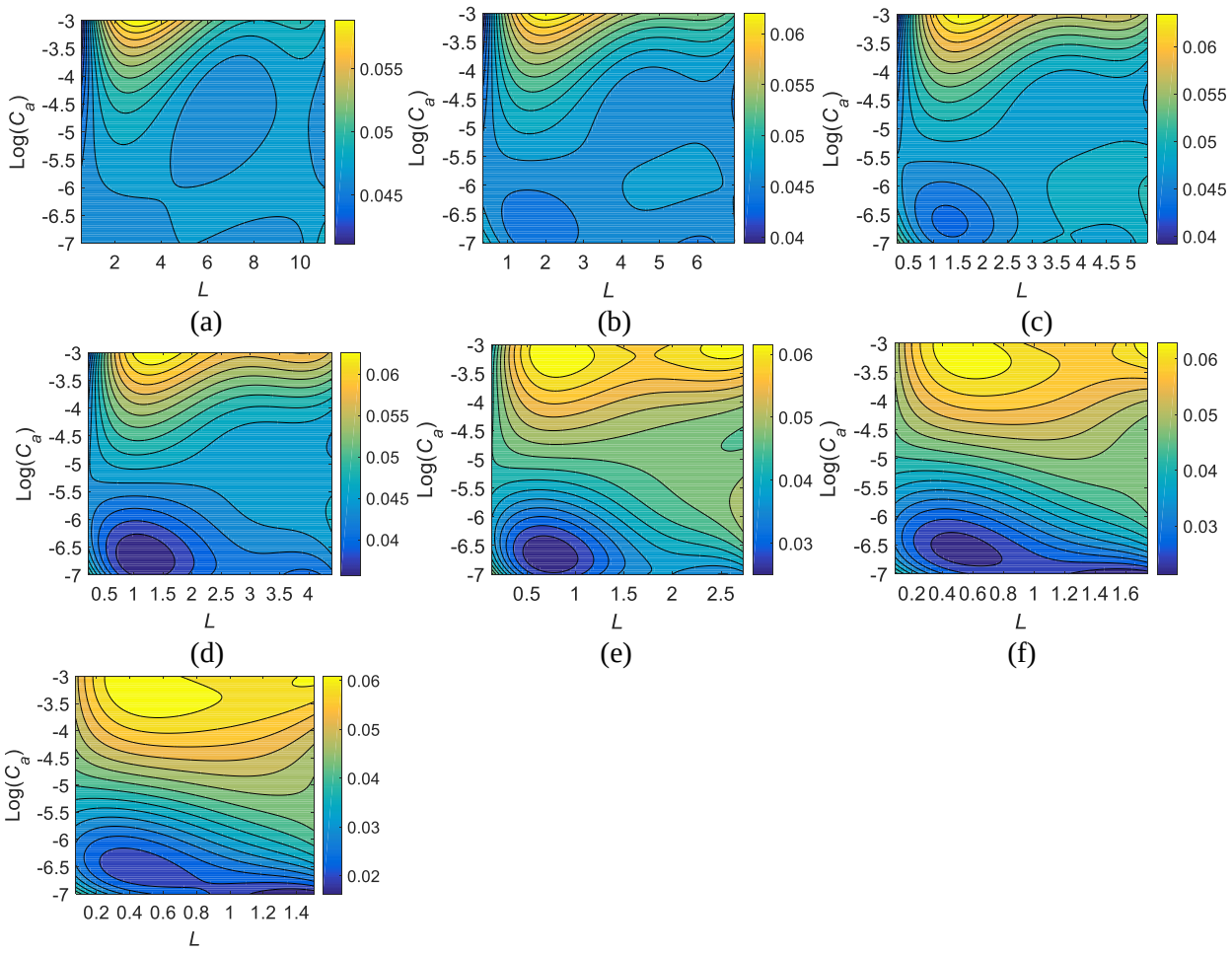

Figure 6.15 Surrogate models for objective function of vibration delocalization of bladed disk with different electro-mechanical coupling. Electro-mechanical coupling of (a) 0.025, (b) 0.050, (c) 0.075, (d) 0.100, (e) 0.200, (f) 0.400, and (g) 0.500

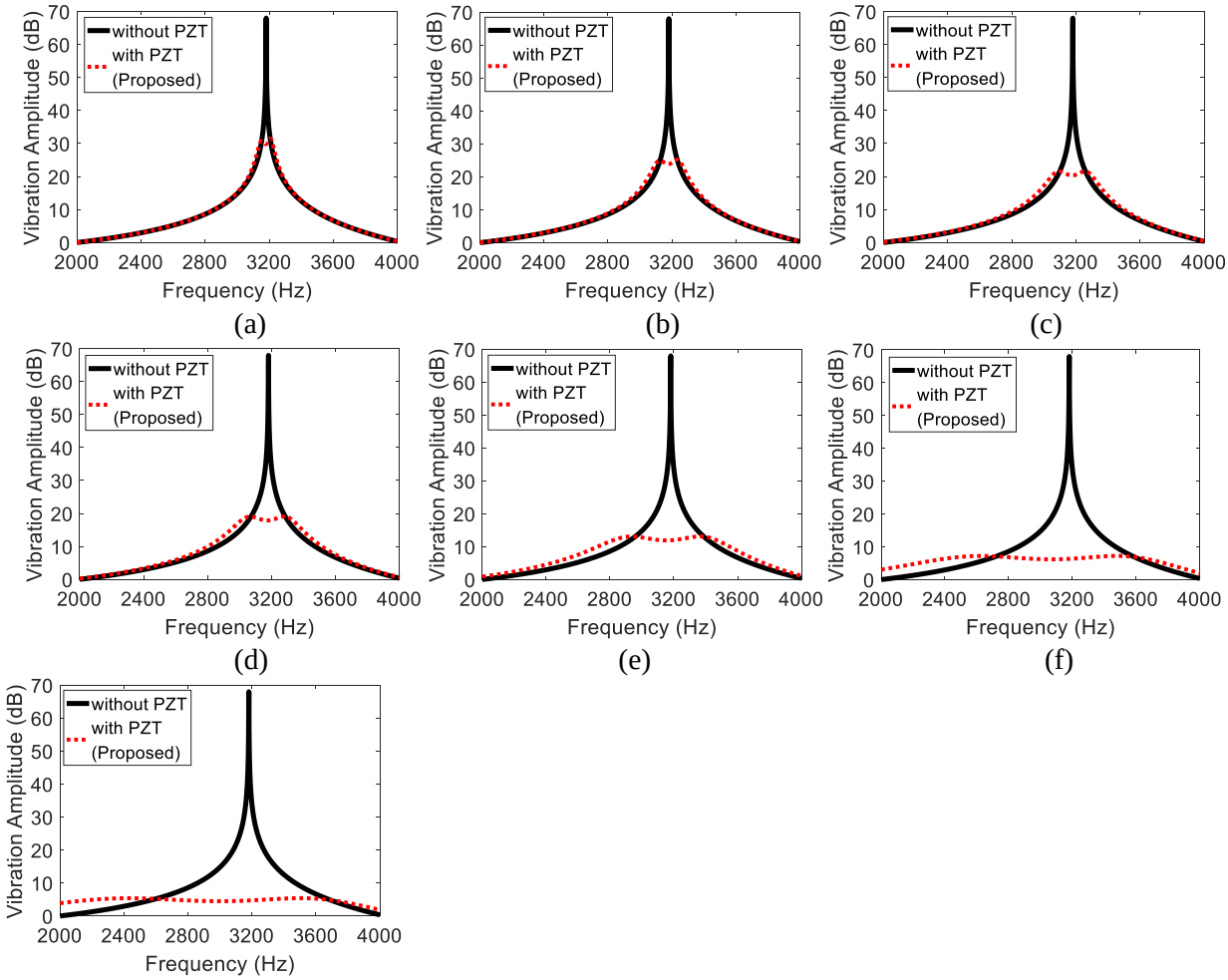

Figure 6.16 Vibration suppression of bladed disk with different electro-mechanical coupling. Electro-mechanical coupling of (a) 0.025, (b) 0.050, (c) 0.075, (d) 0.100, (e) 0.200, (f) 0.400, and (g) 0.500

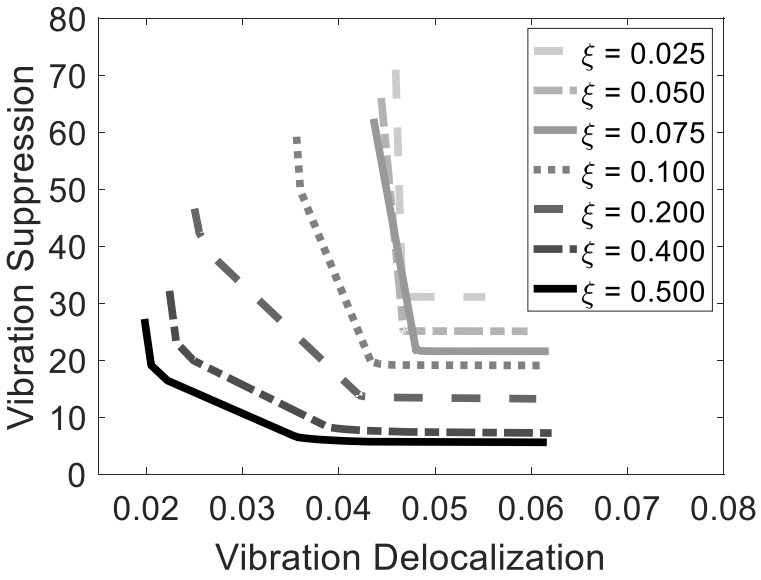

Figure 6.17 *Pareto optimal fronts* for different electro-mechanical couplings (ξ)

Nomenclature

ρ_b, ρ_p	Density of blade and piezoelectric patch
E_b, E_p	Young's modulus of blade and piezoelectric patch
w_b, w_p	Width of blade and piezoelectric patch
l_b, l_p	Length of blade and piezoelectric patch
A_b, A_p	Area of blade and piezoelectric patch
F_p	Moment of area of piezoelectric patch
I_b, I_p	Moment of inertia of blade and piezoelectric patch
k_s	Stiffness of coupling spring
x_s	Location of coupling spring
β_{33}	Dielectric constant of piezoelectric patch
h_{31}	Piezoelectric constant

6.6 Conclusions

Multi-objective optimization of piezoelectric circuit parameters for mode delocalization and vibration suppression using the identical topology of piezoelectric circuitry network is developed in this study. High-fidelity surrogate model for vibration delocalization can be obtained, and the optimal solution is quickly found by the developed gradient-based optimization. Sensitivity of vibration response under engine order excitation with respect to circuit parameters is analytically derived, and the optimal circuit parameters can be efficiently searched by the sensitivity-based optimization. Multi-objective optimization is developed by integrating developed optimization methods together, and the optimal circuit parameters for assigned weight coefficients on mode delocalization and vibration suppression can be obtained. By carrying-out the proposed method for varying weight coefficient, *Pareto optimal front* can be obtained. In case studies, it is observed that *Pareto optimal front* significantly degenerates as the localization level of bladed disk increases and electro-mechanical coupling of the coupled systems decreases. When localization level and electro-mechanical coupling of the system are low, tuning of circuit parameters should be primarily focused on vibration suppression. When localization level and electro-mechanical coupling of the system are high, mode delocalization can be further improved by giving-up vibration suppression to some extends.

Chapter 7. Summary & Conclusions

In this research, new reliability analysis methods are firstly proposed. The proposed novel second-order reliability method entails the error after quadratic approximation, which is inherent in SORM; it thus significantly improves accuracy of the conventional SORM. In order to carry-out more accurate RBDO using the developed SORM, mathematically rigorous sensitivity analysis is carried-out. The proposed sensitivity analysis is both efficient and accurate, and the error, which is generated due to the assumption, is within acceptable range even for higher-order performance function. Assuming accurate surrogate model is available, the sampling-based RBDO in the presence of additional interval uncertainties is developed in this research. The proposed method, while retaining accuracy, can search the worst-case probability of failure in a few iterations, utilizing which the reliable optimum can be obtained within a few design cycles. Therefore, the proposed method can be effectively applied to the problem where function evaluation of the given surrogate model is inexpensive. In this research, new computational framework is then developed to achieve reliability-oriented robust design for bladed disks with the mixture of random and interval uncertainties. Both intentional mistuning and piezoelectric circuitry network are introduced as methods to improve reliability and robustness of the bladed disk. A Metropolis-Hastings based algorithm is adopted, and it can find the worst-case response with high efficiency and accuracy. Reliability can be then accurately calculated under the worst-case condition using Monte Carlo simulation. Using the intentional mistuning technique, gradient-based method is formulated to efficiently find the optimal design. Case study demonstrates that highly reliable 2-sigma bladed disk design can be obtained by the proposed method within a few iterations. Multi-objective optimization approach for piezoelectric circuitry network is introduced as the alternative method to achieve both robustness and reliability of the bladed disk, in case when modification of the nominal design of the bladed disk is not allowed to be modified or the amount of the required modification is too large that aerodynamic performance of the bladed disk can be negatively affected. Sensitivity-based method is employed to optimize components for the piezoelectric circuit for

both objectives of vibration suppression and delocalization. Since objective function for vibration delocalization is not explicitly available, least-squares analysis is carried-out to obtain very accurate surrogate model. The sensitivity-based weighted-sum multi-objective optimization method is developed by utilizing the optimization methods for vibration suppression and delocalization. Pareto optimal front can be obtained with good efficiency using the proposed method. When electro-mechanical coupling is low, corner points of Pareto optimal fronts will be good choices for designs. When electro-mechanical coupling is high, vibration suppression can be sacrificed to achieve better vibration delocalization.

References

[1] Adhikari, S. 2004. "Reliability Analysis Using Parabolic Failure Surface Approximation." *ASCE Journal of Engineering Mechanics* 130 (12): 1407-1427.

[2] Arora, J. 2004. *Introduction to optimum design*. Cambridge: Academic Press.

[3] Beirow, B., A. Kühhorn, T. Giersch, J. Nipkau. 2014. "Forced Response Analysis of a Mistuned Compressor Blisk." *Journal of Engineering Gas Turbines and Power, Transactions of the ASME* 136 (6): 062507.

[4] Beirow, B., T. Giersch, A. Kühhorn, and J. Nipkau. 2015. "Optimization-Aided Forced Response Analysis of a Mistuned Compressor Blisk." *Journal of Engineering for Gas Turbines and Power, Transactions of the ASME* 137(1): 012504.

[5] Bladh, R., M. P. Castanier, and C. Pierre. 2002. "Effects of Multistage Coupling and Disk Flexibility on Mistuned Bladed Disk Dynamics." *Journal of Engineering for Gas Turbines and Power, Transactions of the ASME* 125 (1): 121–130.

[6] Boyd, S., and L. Vandenberghe. 2004. *Convex Optimization*. Cambridge: Cambridge University Press.

[7] Breitung, K. 1984. "Asymptotic Approximations for Multinormal Integrals." *ASCE Journal of Engineering Mechanics* 110 (3): 357-366.

[8] Brooks, S., A. Gelman, G. L. Jones, and X. L. Meng. 2011. *Handbook of Markov Chain Monte Carlo*. Florida: CRC press.

[9] Browder, A. 1996. *Mathematical Analysis: An Introduction*. New York: Springer Science & Business Media.

[10] Bucklew, J. A. 2010. *Introduction to Rare Event Simulation*. New York: Springer Science & Business Media.

[11] Buranathiti, T., J. Cao, W. Chen, L. Baghdasaryan, and Z. C. Xia. 2004. "Approaches for Model Validation: Methodology and Illustration on a Sheet Metal Flanging Process." *ASME Journal of Manufacturing Science and Engineering* 126 (2): 2009–2013.

[12] Cai, B., R. Meyer, and F. Perron. 2008. "Metropolis-Hastings Algorithms with Adaptive Proposals." *Statistics and Computing* 18 (4): 421–433.

[13] Castanier, C. P., and C. Pierre. 2006. "Modeling and Analysis of Mistuned Bladed Disk Vibration: Status and Emerging Directions." *Journal of Propulsion and Power* 22 (2): 384–396.

[14] Castanier, M. P., and C. Pierre. 2002. "Using Intentional Mistuning in the Design of Turbomachinery Rotors." *AIAA Journal* 40 (10): 2077–2086.

[15] Castanier, M. P., and C. Pierre. 2006. "Modeling and Analysis of Mistuned Bladed Disk Vibration: Current Status and Emerging Directions." *Journal of Propulsion and Power* 22 (2): 384-396.

[16] Chan, Y. J., and D. J. Ewins. 2011. "Prediction of Vibration Response Levels of Mistuned Integral Bladed Disks (Blisks): Robustness Studies." *Journal of Turbomachinery, Transactions of the ASME* 134 (4): 044501.

[17] Chandrashaker, A., S. Adhikari, M. I. Friswell. 2016. "Quantification of Vibration Localization in Periodic Structures." *Journal of Vibration and Acoustics, Transactions of the ASME* 138(2): 021002.

[18] Choi, B. k., J. Lentz, A. J. Rivas-Guerra, and M. P. Mignolet. 2003. "Optimization of Intentional Mistuning Patterns for the Reduction of the Forced Response Effects of Unintentional Mistuning:

Formulation and Assessment." *Journal of Engineering for Gas Turbines and Power, Transactions of the ASME* 125 (1): 131–140.

[19] Chowdhury, R., B. N. Rao, and A. M. Prasad. 2009. "High Dimensional Model Representation for Structural Reliability Analysis." *Communication in Numerical Methods in Engineering*. 25 (4): 301-337.

[20] Collette, Y., and P. Siarry. 2013. *Multi-objective Optimization: Principles and Case Studies*. New York: Springer Science & Business Media.

[21] Davies, R. B. 1980. "The Distribution of a Linear Combination of χ^2 Random Variables." *Journal of the Royal Statistical Society*. 29 (3): 323-333.

[22] Deb, K. 2005. *Multi-Objective Optimization Using Evolutionary Algorithms*. New York: John Wiley & Sons.

[23] Denny, M. 2001. "Introduction to Importance Sampling in Rare-Event Simulations." *European Journal of Physics* 22 (4): 403-411.

[24] Ditlevsen, O., and H. O. Madsen. 1996. *Structural Reliability Method*. New York: Wiley.

[25] Dixon, L. C. W., and R. C. Price. 1989. "The Truncated Newton Method for Sparse Unconstrained Optimization Using Automatic Differentiation." *Journal of Optimization Theory and Applications* 60 (2): 261-275.

[26] Du, L., K. K. Choi, and B. D. Youn. 2006. "An Inverse Possibility Analysis Method for Possibility-Based Design Optimization." *The American Institute of Aeronautics and Astronauts* 44 (11): 2682-2690.

[27] Du, X. 2007. "Interval Reliability Analysis." *Proceedings of ASME 2007 International Design Technical Conferences and Computers and Information in Engineering Conference*. Las Vegas, Nevada.

[28] Du, X., A. Sudjianto, and B. Huang. 2005. "Reliability-Based Design with the Mixture of Random and Interval Variables." *Journal of Mechanical Design, Transactions of the ASME* 127 (6): 1068–1076.

[29] Du, X., S. Agus, and B. Huang. 2005. "Reliability-based Design with Mixture of Random and Interval variables." *Journal of Mechanical Design, Transactions of the ASME* 127 (6): 1068-1076.

[30] Du, X., and B. Huang. 2006. "Uncertainty Analysis by Dimension Reduction Integration and Saddle Point Approximations." *Journal of Mechanical Design, Transactions of the ASME* 128 (1): 26-33.

[31] Duan, Y., C. Zang, and E. P. Petrov. 2016. "Forced Response Analysis of High-Mode Vibrations for Mistuned Bladed Disks with Effective Reduced-Order Models." *Journal of Engineering for Gas Turbines and Power, Transactions of the ASME* 138 (11): 112502.

[32] Ducarne, J., O. Thomas, and J. F. Deü. 2012. "Placement and Dimension Optimization of Shunted Piezoelectric Patches for Vibration Reduction." *Journal of Sound and Vibration* 331 (14): 3286-3303.

[33] Duffy, K. P., B. B. Choi, A. J. Provenza, J. B. Min, and N. Kray. 2013. "Active Piezoelectric Vibration Control of Subscale Composite Fan Blades." *Journal of Engineering for Gas Turbines and Power, Transactions of the ASME* 135 (1): 011601.

[34] Farebrother, R. W. 1984. "The Distribution of a Positive Linear Combination of χ^2 Random Variables." *Journal of the Royal Statistical Society*. 33 (3): 332-339.

[35] Forrester, A. I., and A. J. Keane. 2009. "Recent Advances in Surrogate-based Optimization." *Progress in Aerospace Sciences*. 45 (1): 50-79.

[36] Gu, L., R. J. Yang, C. H. Tho, M. Makowskit, O. Faruquet, and Y. Li. 2001. "Optimization and Robustness for Crashworthiness of Side Impact." *International Journal of Vehicle Design* 26 (4): 348-360.

[37] Guo, J., and X. Du. 2009. "Reliability Sensitivity Analysis with Random and Interval Variables." *International Journal for Numerical Methods in Engineering* 78 (13): 1585-1617.

[38] Gupta, V., M. Sharma, and N. Thakur. 2010. "Optimization Criteria for Optimal Placement of Piezoelectric Sensors and Actuators on a Smart Structure: A Technical Review." *Journal of Intelligent Material Systems and Structures* 21 (12): 1227-1243.

[39] Haldar, A., and S. Mahadevan. 2000. *Probability, Reliability, and Statistical Methods in Engineering Design*. New York: John Wiley & Sons.

[40] Han, Y., R. Murthy, M. P. Mignolet, and J. Lentz. 2011. "Optimization of Intentional Mistuning Patterns for the Mitigation of the Effects of Random Mistuning." *Journal of Engineering for Gas Turbines and Power, Transactions of the ASME* 136 (6): 062505.

[41] Hao, P., B. Wang, and G. Li. 2012. "Surrogate-Based Optimum Design for Stiffened Shells with Adaptive Sampling." *AIAA Journal* 50 (11): 2389–2407.

[42] Harville, D. A. 1971. "On the Distribution of Linear Combinations of Non-Central Chi-Squares." *The Annals of Mathematical Statistics* 42 (2): 809-811.

[43] Hasofer, A. M., and N. C. Lind. 1974. "An Exact and Invariant First Order Reliability Format." *ASCE Journal of the Engineering Mechanics Division* 100 (1): 111-121.

[44] Helton, J. C., and F. J. Davis. 2003. "Latin Hypercube Sampling and the Propagation of Uncertainty in Analyses of Complex Systems." *Reliability Engineering & System Safety* 81 (1): 23–69.

[45] Helton, J. C., J. D. Johnson, C. J. Sallaberry, and C. B. Storlie. 2006. "Survey of Sampling-based Methods for Uncertainty and Sensitivity Analysis." *Reliability Engineering and System Safety* 91 (10): 1175-1209.

[46] Hohenbichler, M., and R. Rackwitz. 1988. "Improvement of Second-Order Reliability Estimates by Importance Sampling." *ASCE Journal of Engineering Mechanics* 114 (12): 2195-2199.

[47] Hong, H. P. 1999. "Simple Approximations for Improving Second-order Reliability Estimates." *Journal of Engineering Mechanics* 125 (2): 592–595.

[48] Hoskins, R. F. 1979. *Generalized Functions*. New York: John Wiley & Sons.

[49] Hu, C., and B. D. Youn. 2011. "Adaptive-Sparse Polynomial Chaos Expansion for Reliability Analysis and Design of Complex Engineering Systems." *Structural and Multidisciplinary Optimization* 43 (3): 419-442.

[50] Hu, C., and B. D. Youn. 2011. "An Asymmetric Dimension-Adaptive Tensor-Product Method for Reliability Analysis." *Structural Safety* 33 (3): 218-231.

[51] Huntington, D. E., and C. S. Lyrintzis. 1998. "Improvements to and limitations of Latin Hypercube Sampling." *Probabilistic Engineering Mechanics* 13 (4): 245-253.

[52] Imhof, J. P. 1961. "Computing the Distribution of Quadratic Forms in Normal Variables." *Biometrika* 48 (3/4): 419-426.

[53] Johnson, N. L., S. Kotz, and N. Balakrishnan. 1994. *Continuous Univariate Distributions Volume 2*. New Jersey: John Wiley & Sons.

[54] Kanwal, R. P. 2000. "Generalized Functions: Theory and Technique." *APPLICATIONS OF MATHEMATICS-PRAHA* 45 (4): 320-320.

[55] Kauffman, J. L., and G. A. Lesieutre. 2012. "Piezoelectric-Based Vibration Reduction of Turbomachinery Bladed Disks via Resonance Frequency Detuning." *AIAA Journal* 50 (5): 1137−1144.

[56] Kenyon, J. A., J. H. Griffin, and N. E. Kim. 2005. "Sensitivity of Tuned Bladed Disk Response to Frequency Veering." *Journal of Engineering for Gas Turbines and Power, Transactions of the ASME* 127 (4): 835−842.

[57] Khuri, A. I. 2004. "Applications of Dirac's Delta Function in Statistics." *International Journal of Mathematical Education in Science and Technology* 35 (2): 185-195.

[58] Lee, I., K. K. Choi, and L. Zhao. 2010. "Sampling-Based Stochastic Sensitivity Analysis Using Score Functions for RBDO Problems with Correlated Random Variables." *Journal of Mechanical Design, Transactions of the ASME* 133 (2): 1055-1064.

[59] Lee, I., K. K. Choi, and D. Gorsich. 2009. "Sensitivity Analyses of FORM-based and DRM-based Performance Measure Approach (PMA) for Reliability-based Design Optimization (RBDO)." *International Journal for Numerical Methods in Engineering* 82 (1): 26-46.

[60] Lee, I., K. K. Choi, and L. Zhao. 2011. "Sampling-Based RBDO Using the Dynamic Kriging (D-Kriging) Method and Stochastic Sensitivity Analysis." *Journal of Structural and Multidisciplinary Optimization* 44 (3): 299-317.

[61] Lee, I., K. K. Choi, and L. Zhao. 2011. "Sampling-Based RBDO Using the Stochastic Sensitivity Analysis and Dynamic Kriging Method." *Structural and Multidisciplinary Optimization* 44 (3): 299-317.

[62] Lee, I., K. K. Choi, L. Du, and D. Gorsich. 2008. "Inverse Analysis Method Using MPP-Based Dimension Reduction for Reliability-Based Design Optimization of Nonlinear and Multi-Dimensional Systems." *Computer Methods in Applied Mechanics and Engineering* 198 (1): 14-27.

[63] Lee, I., K. K. Choi, Y. Noh, Z. Liang, D. Gorsich. 2011. "Sampling-Based Stochastic Sensitivity Analysis Using Score Functions for RBDO Problems with Correlated Random Variables." *Journal of Mechanical Design, Transactions of the ASME* 133 (2): 021003.

[64] Lee, I., Y. Noh, and D. Yoo. 2012. "A Novel Second-Order Reliability Method (SORM) Using Noncentral or Generalized Chi-Squared Distributions," *Journal of Mechanical Design, Transactions of the ASME* 134 (10): 10912.

[65] Madsen, H. O., S. Krenk, and N. C. Lind. 1986. *Methods of Structural Safety.* New Jersey: Prentice-Hall, Inc., Englewood Cliffs.

[66] Mahadevan, S., and A. Halder. 2000. *Probability, Reliability and Statistical Method in Engineering Design*. New York: John Wiley & Sons.

[67] Martel, C., R. Corral, and J. M. Llorens. 2008. "Stability Increase of Aerodynamically Unstable Rotors Using Intentional Mistuning." *Journal of Turbomachinery, Transactions of the ASME* 130 (1): 011006.

[68] McDonald, M., and S. Mahadevan. 2008. "Design Optimization with System Reliability Constraints." *Journal of Mechanical Design, Transactions of the ASME* 130 (2): 021403.

[69] McKay, M. D., R. J. Beckman, and W. J. Conover. 2000. "A Comparison of Three Methods for Selecting Values of Input Variables in the Analysis of Output from a Computer Code." *Technometrics* 42 (1): 55-61.

[70] Min, J. B., K. P. Duffy, B. B. Choi, A. J. Provenza, and N. Kray. 2013. "Numerical modeling methodology and experimental study for piezoelectric vibration damping control of rotating composite fan blades." *Computers & Structures* 128: 230-242.

[71] Mourelatos, Z. P., and J. Zhou. 2005. "Reliability Estimation and Design with Insufficient Data Based on Possibility Theory." *AIAA Journal* 43 (8): 1696–1705.

[72] Nikolic, M., E. P. Petrov, and D. J. Ewins. 2008. "Robust Strategies for Forced Response Reduction of Bladed Disks Based on Large Mistuning Concept." *Journal of Engineering for Gas Turbines and Power, Transactions of the ASME* 130 (2): 022501.

[73] Noh, Y., K. K. Choi, and I. Lee. 2011. "Reliability-Based Design Optimization with Confidence Level Under Input Model Uncertainty due to Limited Test Data." *Structural and Multidisciplinary Optimization* 43 (4): 443-458.

[74] Noh, Y., K. K. Choi, I. Lee, D. Gorsich, and D. Lamb. 2011. "Reliability-based Design Optimization with Confidence Level for Non-Gaussian Distributions Using Bootstrap Method." *Journal of Mechanical Design, Transactions of the ASME* 133 (9): 091001.

[75] Olsson, A., G. Sandberg, and O. Dahlblom. 2003. "On Latin Hypercube Sampling for Structural Reliability Analysis." *Structural Safety* 25 (1): 47-68.

[76] Penmetsa, R. C., and R. V. Grandhi. 2002. "Efficient Estimation of Structural Reliability for Problems with Uncertain Intervals." *Computers & Structures* 80 (12): 1103-1112.

[77] Petrov, E. P., and D. J. Ewins. 2003. "Analysis of the Worst Mistuning Patterns in Bladed Disk Assemblies." *Journal of Turbomachinery, Transactions of the ASME* 125 (4): 623–631.

[78] Petrov, E. P., and D. J. Ewins. 2006. "Effects of Damping and Varying Contact Area at Blade-Disk Joints in Forced Response Analysis of Bladed Disk Assemblies." *Journal of Turbomachinery, Transactions of the ASME* 128 (2): 403–410.

[79] Polidori, D. C., J. L. Beck, and C. Papadimitriou. 1999. "New Approximations for Reliability Integrals." *Journal of Engineering Mechanics* 125 (4): 466–475.

[80] Press, S. J. 1966. "Linear Combinations of Non-Central Chi-Square Variates." *The Annals of Mathematical Statistics* 37 (2): 480-487.

[81] Provost, S. B., and E. M. Rudiuk. 1996. "The Exact Distribution of Indefinite Quadratic Forms in Noncentral Normal Vectors." *Annals Institute of Statistical Mathematics* 48 (2): 381-394.

[82] Queipo, N. V., R. T. Haftka, W. Shyy, T. Goel, R. Vaidyanathan, and P. K. Tucker. 2005. "Surrogate-Based Analysis and Optimization." *Progress in Aerospace Sciences* 41 (1): 1-28.

[83] Rahman, S., and D. Wei. 2006. "A Univariate Approximation at Most Probable Point for Higher-Order Reliability Analysis." *International Journal of Solids and Structures* 43 (9): 2820-2839.

[84] Rahman, S., and D. Wei. 2008. "Design Sensitivity and Reliability-based Structural Optimization by Univariate Decomposition." *Structural and Multidisciplinary Optimization* 35 (3): 245-261.

[85] Rahman, S. 2009. "Stochastic Sensitivity Analysis by Dimensional Decomposition and Score Functions." *Probabilistic Engineering Mechanics* 24 (3): 278–287.

[86] Rice, J. A. 2006. *Mathematical Statistics and Data Analysis*. California: Thomson Higher Education.

[87] Roberts, G. O., and J. S. Rosenthal. 2001. "Optimal Scaling for Various Metropolis-Hastings Algorithms." *Statistical Science* 16 (4): 351–367.

[88] Rosenblatt, M. 1952. "Remarks on A Multivariate Transformation." *The Annals of Mathematical Statistics*. 23 (3): 470-472.

[89] Rosenblueth, E. 1975. “Point Estimates for Probability Moments.” *Proceedings of the National Academy of Sciences* 72 (10): 3812-3814.

[90] Ruben, H. 1962. “Probability Content of Regions under Spherical Normal Distributions, IV: The Distribution of Homogeneous And Non-Homogeneous Quadratic Functions of Normal Variables.” *The Annals of Mathematical Statistics* 33 (2): 542-570.

[91] Rubinstein, R. Y., and A. Shapiro. 1993. *Discrete Event Systems—Sensitivity Analysis and Stochastic Optimization by the Score Function Method*. New York: John Wiley & Sons.

[92] Rubinstein, R. Y., and D. P. Kroese. 2008. *Simulation and Monte Carlo Method*. New Jersey: John Wiley & Sons.

[93] Saichev, A. I., and W. A. Woyczynski. 1997. *Distributions in the Physical and Engineering Sciences*. Boston, MA.

[94] McKay, M. D., R. J. Beckman, and J. William. 1979. “Comparison of Three Methods for Selecting Values of Input Variables in the Analysis of Output from a Computer Code.” *Technometrics* 21 (2): 239-245.

[95] Shah, B. K. 1963. “Distribution of Definite and of Indefinite Quadratic Forms from a Non-Central Normal Distribution.” *The Annals of Mathematical Statistics* 34 (1): 186-190.

[96] Shapiro, B., and K. E., Willcox. 2003. “Analyzing Mistuning of Bladed Disks by Symmetry and Reduced-Order Aerodynamic Modeling.” *Journal of Propulsion and Power* 19 (2): 307–311.

[97] Siddiqui, M. M., and S. H. Alkarni. 2001. “An Upper Bound for The Distribution Function of A Positive Definite Quadratic Form.” *Journal of Statistical Computation and Simulation* 69 (1): 41-56.

[98] Simpson, T. W., T. M. Mauery, J. J. Korte, and F. Mistree. 2001. “Kriging Models for Global Approximation in Simulation-Based Multidisciplinary Design Optimization.” *AIAA Journal* 39 (12): 2233-2241.

[99] Sivanandam, S. N., and S. N. Deepa. 2007. *Introduction to Genetic Algorithms*. Massachusetts: Springer Science & Business Media.

[100] Tang, J., and K. W. Wang. 2003. “Vibration Delocalization of Nearly Bladed Disks Using Coupled Piezoelectric Networks.” *Journal of Vibration and Acoustics, Transactions of the ASME* 125 (1): 95–108.

[101] Trefethen, L. N. 1997. *Numerical Linear Algebra*. Philadelphia, PA: SIAM.

[102] Triplett, A., and D. D. Quinn. 2009. “The Effect of Non-Linear Piezoelectric Coupling on Vibration-Based Energy Harvesting.” *Journal of Intelligent Material Systems and Structures* 20 (16): 1959-1967.

[103] Tu, J., and K. K. Choi. 1999. “A New Study on Reliability-Based Design Optimization,” *Journal of Mechanical Design* 121 (4): 557–564.

[104] Tu, J., K. K. Choi, and Y. H. Park. 2001. “Design Potential Method for Reliability-Based System Parameter Design Using Adaptive Probabilistic Constraint Evaluation.” *AIAA Journal* 39 (4): 667-677.

[105] Wang, K. W., and J. Tang. 2009. *Adaptive Structural System with Piezoelectric Transducer Circuitry*. New York: Springer Science & Business Media.

[106] Webb, A. R. 2003. *Statistical Pattern Recognition*. New Jersey: John Wiley & Sons.

[107] Wei, D. L., Z. S. Cui, and J. Chen. 2008. “Uncertainty Quantification Using Polynomial Chaos Expansion with Points of Monomial Cubature Rules.” *Computers & Structures* 86 (23-34): 2102-2108.

[108] Whittaker, E. T. 1904. “An Expression of Certain Known Functions as Generalized Hypergeometric Functions.” *Bulletin of the American Mathematical Society* 10 (3): 125-134.

[109] Wickenheiser, A. M., T. Reissman, W. J. Wu, and G. Ephrahim. 2010. “Modeling the Effects of Electromechanical Coupling on Energy Storage through Piezoelectric Energy Harvesting.” *IEEE/ASME Transactions on Mechatronics* 15 (3): 400-411.

[110] Xiong, F., S. Greene, W. Chen, Y. Xiong, and S. Yang. 2010. “A New Sparse Grid Based Method for Uncertainty Propagation.” *Structural and Multidisciplinary Optimization* 41 (3): 335-349.

[111] Yoo, D., and I. Lee. 2014. “Sampling-Based Approach for Design Optimization in the Presence of Interval Variables.” *Structural Multidisciplinary Optimization* 49 (2): 253–266.

[112] Yoo, D., I. Lee, and H. Cho. 2014. “Probabilistic Sensitivity Analysis for Novel Second-Order Reliability Method (SORM) Using Generalized Chi-Squired Distribution.” *Structural Multidisciplinary Optimization* 50 (5): 787–797.

[113] Yoo, D., I. Lee, and J. Tang. 2017. “Reliability-Oriented Optimal Design of Intentional Mistuning for a Bladed Disk with Random and Interval Uncertainties.” *Engineering Optimization* 49 (5): 796-814.

[114] Yoo, H. H., J. Y. Kim, and D. J. Inman. 2003. “Vibration Localization of Simplified Mistuned Cyclic Structures Undertaking External Harmonic Force.” *Journal of Sound and Vibration* 261 (5): 859–870.

[115] Youn, B. D., K. K. Choi, L. Du, and D. Gorsich. 2007. “Integration of Possibility-Based Optimization and Robust Design for Epistemic Uncertainty.” *Journal of Mechanical Design, Transactions of the ASME* 129 (8): 876–882.

[116] Youn, B. D., Z. Xi, L. J. Wells, and D. A. Lamb. 2006. “Stochastic Response Surface Using The Enhanced Dimension Reduction (eDR) Method For Reliability-Based Robust Design Optimization.” *III European conference on Computational Mechanics*, Lisbon, Portugal.

[117] Youn, B. D., X. Zhimin, and P. Wang. 2008. “Eigenvector Dimension Reduction (EDR) Method for Sensitivity-Free Uncertainty Quantification.” *Structural and Multidisciplinary Optimization* 37 (1): 13-28.

[118] Yu, C. B., J. J. Wang, and Q. H. Li. 2011. “Investigation of the Combined Effects of Intentional Mistuning, Damping and Coupling on the Forced Response of Bladed Disks.” *Journal of Vibration and Control* 17 (8): 1149–1157.

[119] Yu, C. B., J. J. Wang, and Q. H. Li. 2011. "Investigation of the Combined Effects of Intentional Mistuning, Damping and Coupling on the Forced Response of Bladed Disks." *Journal of Vibration and Control* 17 (8): 1149-1157.

[120] Yu, H., and K. W. Wang. 2007. “Piezoelectric Networks for Vibration Suppression of Mistuned Bladed Disks.” *Journal of Vibration and Acoustics, Transactions of the ASME* 129 (5): 559-566.

[121] Yu, H., and K. W. Wang. 2009. “Vibration Suppression of Mistuned Coupled-Blade-Disk Systems Using Piezoelectric Circuitry Network.” *Journal of Vibration and Acoustics, Transactions of the ASME* 131 (2): 021008.

[122] Yu, H., K. W. Wang, and J. Wang. 2006. “Piezoelectric Networking with Enhanced Electromechanical Coupling for Vibration Delocalization of Mistuned Periodic Structures – Theory and Experiment.” *Journal of Sound and Vibration* 295 (1): 246–265.

[123] Yu, H., K. W. Wang, and J. Zhang. 2006. “Piezoelectric Networking with Enhanced Electromechanical Coupling for Vibration Delocalization of Mistuned Periodic Structures—Theory and Experiment.” *Journal of Sound and Vibration* 295 (1): 246-265.

[124] Zhang, J., and X. Du. 2010. “A Second-Order Reliability Method with First-Order Efficiency.” *Journal of Mechanical Design* 132 (10): 101006.

[125] Zhang, J., and K. W. Wang. 2002. “Electromechanical Tailoring of Piezoelectric Networks for Vibration Delocalization and Suppression of Nearly-Periodic Structures.” *Proceedings of 13th International Conference on Adaptive Structures and Technologies*: 199-212.

[126] Zhao, L., K. K. Choi, and I. Lee. 2011. “Metamodeling Method Using Dynamic Kriging for Design Optimization.” *AIAA Journal* 49 (9): 2034-2046.

[127] Zhou, B., F. Thouverez, and D. Lenoir. 2014. "Essentially nonlinear piezoelectric shunt circuits applied to mistuned bladed disks." *Journal of Sound and Vibration* 333 (9): 2520-2542.

[128] Zhou, K., A. Hedge, P. Cao, and J. Tang. 2017. “Design Optimization Toward Alleviating Forced Response Variation in Cyclically Periodic Structure Using Gaussian Process.” *Journal of Vibration and Acoustics* 139 (1): 011017.

[129] Zingg, D. W., M. Nemec, and T. H. Pulliam. 2008. “A Comparative Evaluation of Genetic and Gradient-based Algorithms Applied to Aerodynamic Optimization.” *European Journal of Computational Mechanics/Revue Européenne de Mécanique Numérique* 17 (1-2): 103-126.